Doctoral Thesis

Various dimensional design of high capacity anodes for advanced lithium storage system

Gyujin Song

Department of Energy Engineering

(Energy Engineering)

Graduate School of UNIST

2020

Various dimensional design of high capacity anodes for advanced lithium storage system

Gyujin Song

Department of Energy Engineering
(Energy Engineering)

Graduate School of UNIST

Various dimensional design of high capacity anodes for advanced lithium storage system

A thesis/dissertation
submitted to the Graduate School of UNIST
in partial fulfillment of the
requirements for the degree of
Doctor of Philosophy

Gyujin Song

12/13/2019
Approved by

Nam-Soon Choi

Advisor
Nam-Soon Choi

Various dimensional design of high capacity anodes for advanced lithium storage system

Gyujin Song

This certifies that the thesis/dissertation of Gyujin Song is approved.

12/13/2019

Signature

Advisor: Nam-Soon Choi

signature

Prof. Soojin Park

signature

Prof. Sang Kyu Kwak

signature

Prof. Il-Doo Kim

signature

Prof. Hyun-Wook Lee

Abstract

With the demand to overcome the issues concerning environmental pollution of fossil fuel in large-scale system and various fields, numerous efforts have been devoted toward a design of rational energy storage system (ESS) in order to substitute present energy source. While lots of systems are suggested, lithium-ion batteries (LIBs) have been attracted as one of the promising ESS among various storage devices. Existing one which consists of a graphite anode unfortunately have the trouble to fulfilling required condition such as high power and energy density. Thus, new type of anode materials has been developed to achieve mentioned specifications. As possible candidates, silicon (Si) and germanium (Ge) have been emerged owing to their high gravimetric/volumetric capacity and low operating voltage. Nevertheless, those materials remain under challenge level because inferior electronic properties have the limit to catch high power density and unexpected volume expansion on a lithiation process into materials, resulting in the electrode failure and capacity decay where factors influence safety and stability issues in LIBs system.

Here, we introduce approaches through dimensional manipulation to proceed. Overall synthetic processes are focused on versatile method, a possibility of mass production and evaluation methods obviously demonstrate intrinsic/extrinsic characteristic ways. With *in situ* microscopic/electrochemical techniques, specific properties and electrochemical reaction mechanism of synthesized materials are clearly unveiled to facilitate power density enhancement and volume change suppression.

In Chapter II, we present zero-dimensional (0D) carbon wrapped-hollow Si microparticles which possess porous shell structure from various silica source regardless of their shape. Sequent top-down and bottom-up processes fabricate uniform 0D Si and a key factor for unique formation mechanism is verified through *ex situ* characterization and simulation results. In electrochemical view, creating cavities in a core and pores in the shell alleviate volume expansion and enable short ion-diffusion length. Surface carbon layer additionally provide fast electron movement to guarantee stable and considerable power density. Besides, *in situ* transmission electron microscopic (TEM) demonstrate the stability of morphological structure on charge/discharging cycle.

In Chapter III, we design one-dimensional (1D) Ge/zinc (Zn)-based nanofibers. Homogeneous Ge/Zn nanofibers *via* electrospinning method and solid-gas reduction reaction own atomic-level distribution of each element. Well-dispersive metallic Zn in Ge nanofiber could effectively improve electronic conductivity/volumetric stability and nanosized structure also features facile ion transport and stress release by volume expansion on electrochemical cycles. *In situ*

TEM/electrochemical impedance spectroscopy (EIS) deeply investigate the critical role of ionic bond of Zn element in Ge nanofibers.

In Chapter IV, we introduce additional 1D Ge nanofibers, which feature numerous sizes of pores in whole morphological structure. Intrinsic metal oxide characters based on Ellingham diagram enable to carve heterogenous pore in and out of nanofibers. This structure shows stable electrochemical cyclability without a large volume expansion. Further, we confirm the unique behavior of Ge, called memory effect in LIBs. *In situ* TEM characterization supports that numerous pores work as volume buffer sites and keep spatial reversibility on charge/discharge cycles.

In Chapter V, we finally suggest synthetic method of three-dimensional (3D) porous Ge clusters from zeotype-borogermanate microcubes, artificial Ge-rich zeolite. This starting material is prepared in a large quantity through a simple hydrothermal process as followed by sequential thermal and etching treatment to produce 3D porous Ge. As-fabricated product interestingly behaves like a pseudocapacitance exhibiting fast electrochemical kinetics. Further, the as-formed pores build up stable solid electrolyte interphase (SEI) layer on the surface for prolonged cycles, improving cycle stability.

In Chapter VI, we briefly provide the insight for the correlation of the dimensions and electrochemical properties toward advanced lithium storage system. To handle unsettled issues in large-scale lithium batteries, it is essential to look around the overall circumstances to match the specific purpose.

Blank page

Contents

List of figures

Nomenclature

ESS	Energy storage system
LIBs	Lithium-ion batteries
Si	Silicon
Ge	Germanium
0D	Zero-dimensional
TEM	Transmission electron microscopy
1D	One-dimensional
Zn	Zinc
EIS	Electrochemical impedance spectroscopy
3D	Three-dimensional
SEI	Solid electrolyte interphase
$LiMO_x$	Li-stored transition metal oxide
LCO	Lithium cobalt oxide
LMO	Lithium manganese oxide
LFP	Lithium iron phosphate
LTO	Lithium titanium oxide
TRR	Thermochemical reduction reaction
Al	Aluminum
$AlCl_3$	Aluminum chloride
HPSS	Hollow porous silicon sphere
DFT	Density function theory
AlOCl	Aluminum oxychloride
HF	Hydrofluoric acid
HCl	Hydrochloric acid
PBE	Perdew-Burke-Ernzerhof
Ar	Argon
SS	Stainless steel
SiO_2	Silica
D.I. water	Deionized water
C_2H_2	Acetylene
FE-SEM	Field-emission scanning electron microscopy
STEM	Scanning transmission electron microscopy
EDX	Energy dispersive X-ray spectroscopy

XRD	X-ray diffraction
TGA	Thermogravimetric analysis
XPS	X-ray photoelectron spectroscopy
W	Tunsten
Li_2O	Lithium oxide
PAA	Poly(acrylic acid)
CMC	carboxymethylcellulose
PE	Polyethylene
EC	Ethylene carbonate
DMC	Dimethyl carbonate
FEC	Fluorinated ethylene carbonate
$LiPF_6$	Lithium hexafluorophosphate
PVdF	Poly(vinylidene) fluoride
ESP	Electrostatic potential
$Al(OH)_3$	Aluminum hydroxide
HR-TEM	High-resolution transmission electron microscopy
SAED	Selected area electron diffraction
EVs	Electric vehicles
GeO_x	Oxygen-containing germanium
NFs	Nanofibers
O-dGZNFs	Oxygen-deficient germanium-zinc composite nanofibers
GeO_2	Germanium oxide
PVP	Poly(vinyl pyrrolidone)
$Zn(NO)_3{\cdot}6H_2O$	Zinc nitrate hexahydrate
O-iGZNFs	Oxygen-including germanium-zinc composite nanofibers
H_2	Hydrogen gas
ETEM	Environmental transmission electron microscopy
ICP	Inductively coupled plasma
EA	Elemental analyzer
XANES	X-ray absorption near-edge structure
EXAFS	Extended X-ray absorption fine structure
STM	Scanning tunneling microscope
Pt	Platinum
PP	Polypropylene
O-iGNFs	Oxygen-including germanium nanofibers

O-dGNFs	Oxygen-deficient germanium nanofibers
HADDF-STEM	High-angle annular dark-field scanning transmission electron microscopy
Li_2CO_3	Lithium carbonate
LUMO	Lower unoccupied molecular orbital
CV	Cyclic voltammetry
GS-EIS	Galvanostatic electrochemical impedance spectroscopy
R_{CT}	Charge transfer resistance
NW	Nanowire
CVD	Chemical vapor deposition
NPGeNFs	Nanoporous germanium nanofibers
TEOS	Tetraethyl orthosilicate
DMF	Dimethylformamide
BJH	Barrett−Joyner−Halenda
ZRR	Zincothermic reduction reaction
TEOG	Germanium (IV) ethoxide
Mg	Magnesium
ICEs	Initial coulombic efficiencies
3D-pGe	Three-dimensional porous germanium
KBGO	$K_2B_2Ge_3O_{10}$
$K_2B_4O_7 \cdot 4H_2O$	potassium tetraborate tetrahydrate
KGO	$K_2Ge_4O_9$
TGA-DSC	Thermogravimetric analysis-differential scanning calorimeter
FFT	Fast Fourier transform

1. Introduction

1.1 Energy storage system

Numerous energy sources have employed where a fossil fuel has been considered one of the common sources to generate and supply the power to operate devices and systems. Meanwhile, with the demand of eco-friend and sustainable development in energy field, renewable energy usage such as solar[1], geothermal[2], biomass[3], wind[4], electric[5], hydroelectric[6] forms and energy storage system have been emerged as sustainable design to facilitate efficiently obtained energy from renewable sources. Besides, depending on types of energy storages, energy could be saved as electrochemical (batteries[7], flow batteries[8], hydrogen[9]), mechanical (Flywheels[10], compressed air[11]), electrical (capacitor[12], supercapacitor[13], superconductive magnetic[14]), and thermal (hot water[15], thermal fluid[16], ceramic thermal[17]) storages[18, 19].

Unfortunately, environmental resources like solar and wind could not sustain the required amounts, which mean that these are not reliable ones to operate the power due to the caprice of the climate. So, to achieve stable energy supply and deal lots of energy amounts, electrical energy storage using electricity should act as a key player in worldwide energy consumption to facilitate various energy devices such as grid-scale energy storage, electric, and hybrid vehicles while replacing fossil fuel to result in green house gas[20].

Electrical energy would be converted as another form(e.g. chemical or mechanical type) of energy along the need of usage. In particular, electrochemical conversion technologies, which generate the power through the switch between chemical and electric energy, have been attracted with benefits of high reversibility, facile conversion operating, and considerable energy density[21]. In accordance with the required power/energy, various types of operating systems, divided by occurred electrochemistry in storage and conversion principles[22].

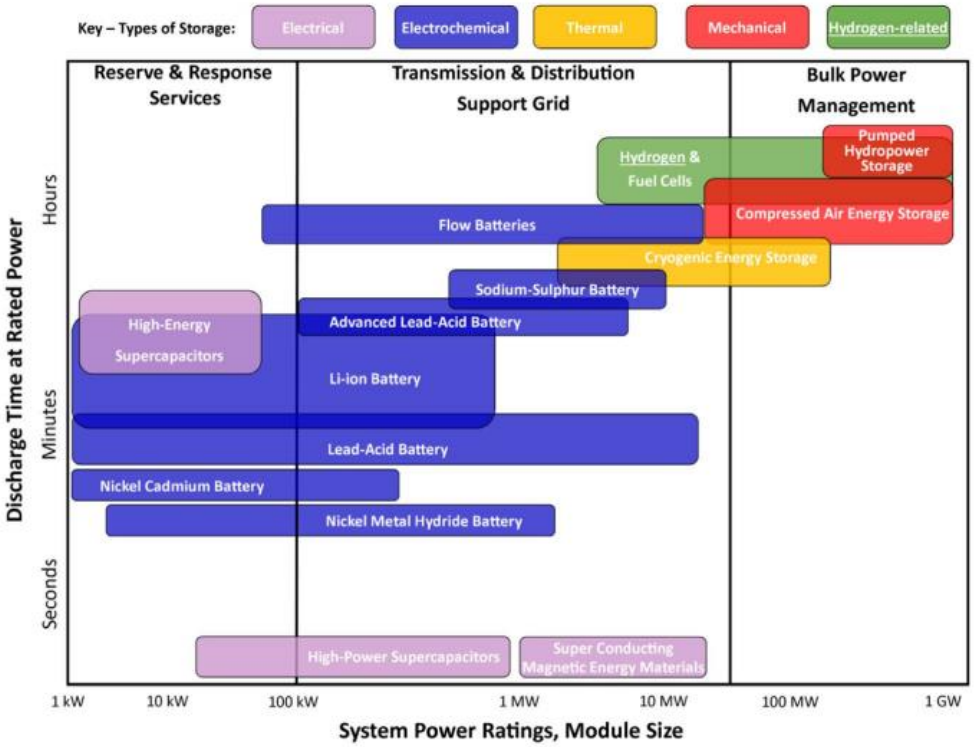

Figure 1-1. Comparison types of energy storage system[18].

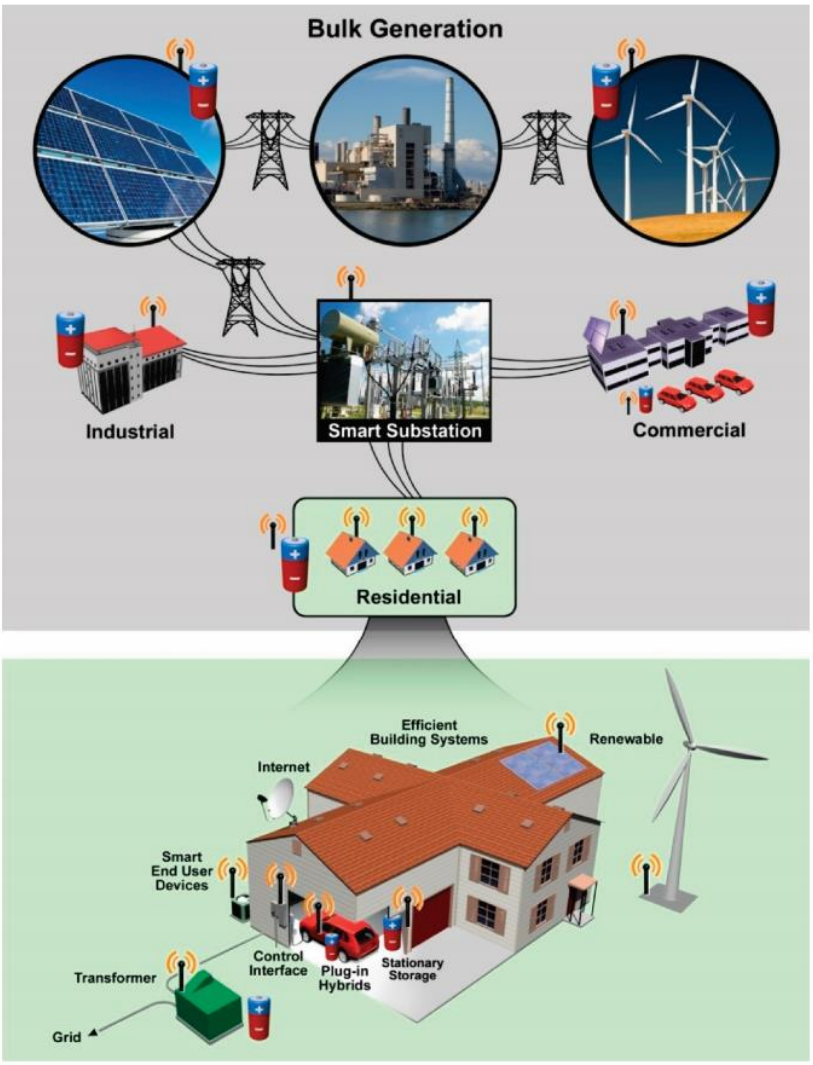

Figure 1-2. Application of electric storage from small size to large girds[20].

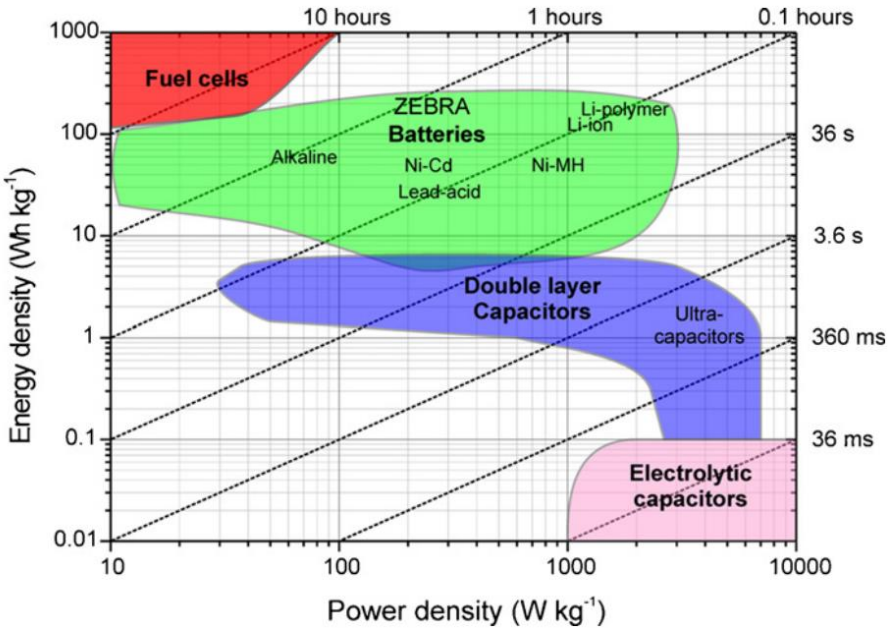

Figure 1-3. Ragone plot for electrical energy storage technologies[22].

1.2 Lithium-ion batteries

Lithium-ion batteries (LIBs) are one of well-known rechargeable energy conversion technologies between electric and chemical forms, quite reliable and meet the global demands for environment and versatility[23-25]. LIBs consist of four key components (anode[26], cathode[27], electrolyte[28], and separator[29]) to generate and store electric energy in devices. Both anode and cathode participate in realizing capacity while electrolyte provides the pathway of Li-ion transportation. Meanwhile, the separator electrically blocks the direct contact of the anode and cathode on electrochemical reaction. According to the charge process, anode accepts Li-ions and electrons from electrolytes and external circuit, respectively whereas cathode loses each charge carriers from the electrode. The discharge process follows reverse reaction direction while the anode gives the Li-ions and electrons to the cathode part. In this respect, each electrode should feature Li-active materials, which accumulate and export the Li-ions reversibly.

Cathode materials are composed of Li-stored transition metal oxides ($LiMO_x$, M:metal, O:oxygen). Firstly, two-dimensional layered structure of lithium cobalt oxide ($LiCoO_2$, LCO) had been suggested, reacting through Li intercalation/deintercalation into layers of LCO on charging/discharging process. Besides, three-dimensional spinel structure of lithium manganese oxide ($LiMn_2O_4$, LMO), and one-dimensional spinel structure of lithium iron phosphate ($LiFePO_4$, LFP) have been recently introduced as potential cathode materials[30-32]. Likewise, general cathode materials involve transition metals, which enable the change of oxidation states allowing Li-ions to store/export in cathode reversibly.

In case of anode materials, these are divided into three types along the reaction mechanism, intercalation, conversion, and alloying reaction[33-36]. The intercalation (insertion) mechanism, representatively graphite and lithium titanium oxide ($Li_4Ti_5O_{12}$, LTO), is similar with cathode materials showing that Li-ions are stored in vacant sites in lattices of anode materials, showing that these barely experience structural deformation on charging process. On the other hand, anode materials with alloying mechanism realizes high gravimetric capacity compared with materials with intercalation mechanism however alloying reaction causes dramatic volume change, resulting in electrode failure and low efficiency of batteries. In this regard, the commercialized batteries have been released, assembled with graphite anode due to safety issue, only applying small sized devices like smartphone and laptop. So, it is essential to develop high capacitive anode materials toward the application of electric vehicles and large-scale energy storage system[37].

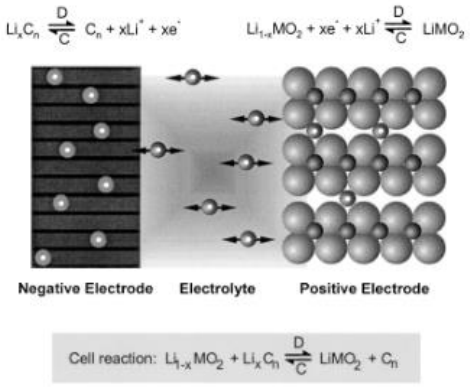

Figure 1-4. Electrochemical reaction of lithium-ion batteries in terms of charge/discharge process[23].

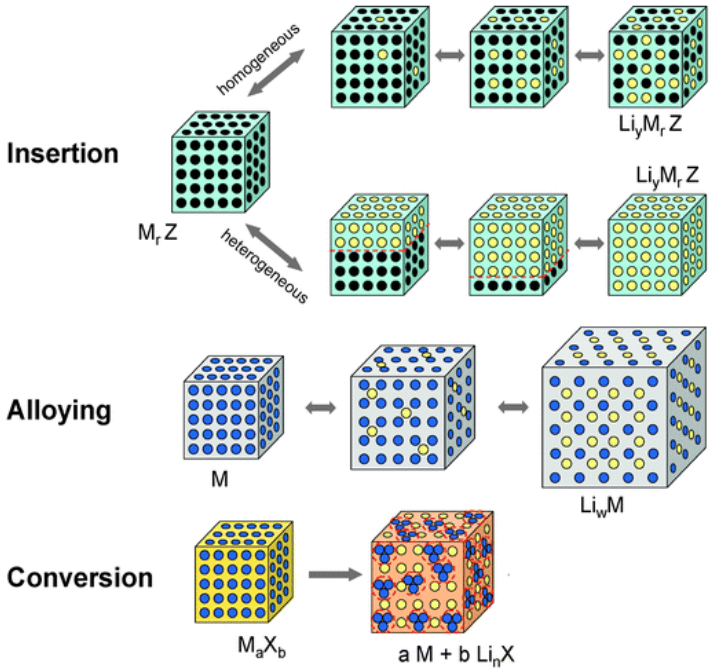

Figure 1-5. Three types of different electrochemical reaction in anodes for lithium-ion batteries[36].

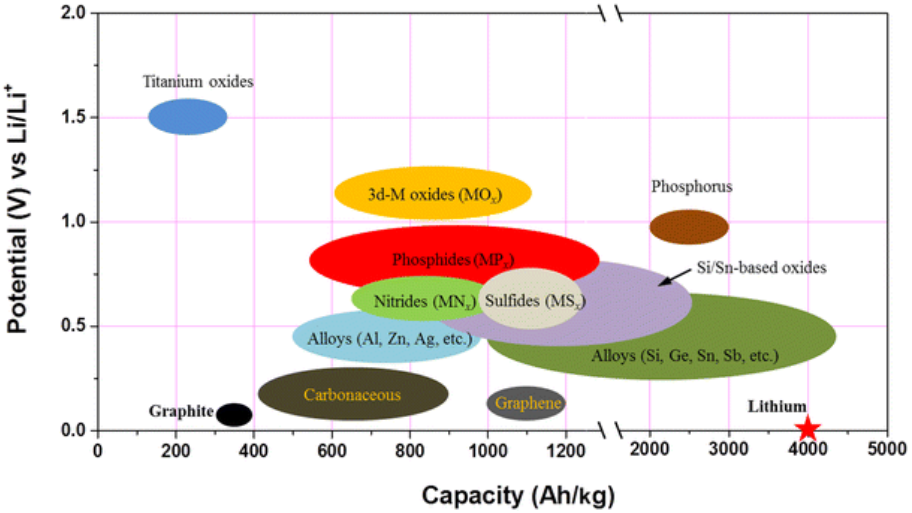

Figure 1-6. Comparison of potential and specific capacity of active materials[37].

1.3 High capacity anode materials

Graphite anodes, now commercialized materials, exhibits stable cyclability for long life span as mentioned. However, intercalation mechanism of graphite, which accepts Li-ion into each graphene layers for electrochemical reaction, cannot perform a high specific capacity toward desired battery system requiring high power/energy density in large-scale devices. Thus, it is essential to develop higher capacity to generate advanced electrochemical performance in same condition to meet the high specification. Therefore, alloying materials like silicon (Si), germanium (Ge) have been emerged as one of the promising candidates to satisfy high energy density batteries due to reaction mechanism where many Li atoms can accumulate in each Si or Ge atom ($M + xLi^+ + xe^- \rightarrow Li_xM$, M: Si or Ge, $0 < x < 4.4$)[38, 39].

Nevertheless, alloy-type materials accompany with uncontrollable volume expansion during charging/discharging process. So, the electrode suffers from pulverization, fracture, contact loss with a current collector, and followed by electrode failure. To alleviate volumetric change on electrochemical reaction, various strategies have been designed through nanostructuring[40, 41], reducing dimension[42, 43], morphology modification[444, 45], forming coating layer[46-48], introducing doped elements[49], and mixing another material as composites[50-54].

The nanostructure alloying materials prevent critical pulverization and fracture formation while inserting Li-ions into the electrode as well as enable that Li-ion experience short ion diffusion length[55]. Lower dimensional, 0D (spheres)[56], 1D (fibers)[57], and 2D (sheets)[58] structures, synthesized via various synthetic approaches, also provide stress-relief properties which persist stable cyclability. Further, high surface area-to-volume of low dimensional materials utilizes numerous contact points for Li-ion electrochemical reaction. Besides, hollow or porous morphological structures provide available cavities to accumulate volume change during alloy reaction[59]. Additionally, doping and composites integrities can improve electrical and mechanical properties extrinsically/intrinsically. Doping elements influence density of states of Si or Ge anodes, enhancing intrinsic electrochemical characteristics[60-62]. Composites/coating layers compensates inferior electronic conductivity of materials and buffer volume change, resulting in stable cycle retention at fast power density while maintaining such highly developed energy density[63].

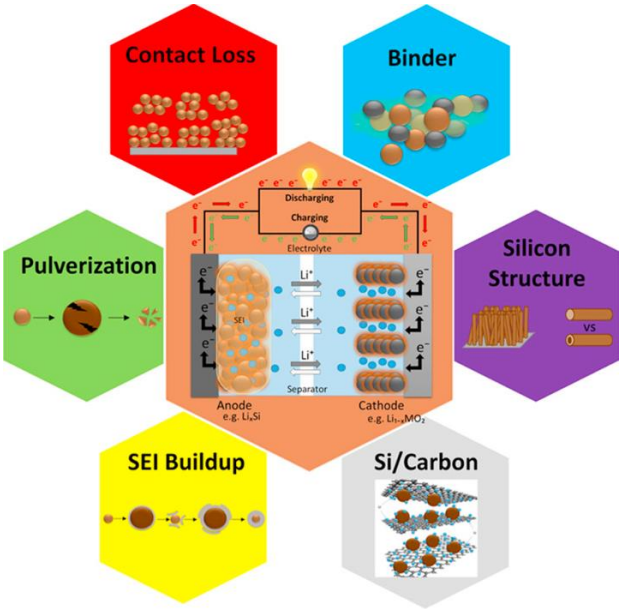

Figure 1-7. Schematic summary of issues of alloying materials and suggested strategies[54].

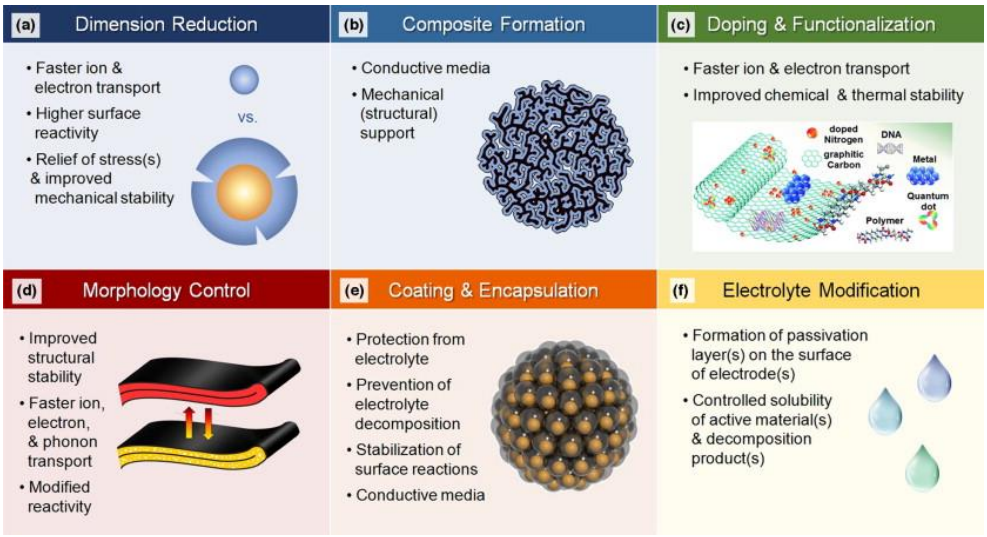

Figure 1-8. General strategies for enhanced electrochemical performance of alloying materials[63].

1.4 Reference

1. Lewis, N. S. Toward Cost-Effective Solar Energy Use. *Science* **2007**, *315*, 798.

2. Fridleifsson, I. B. Geothermal energy for the benefit of the people. *Renew. Sustain. Energy Rev.* **2001**, *5*, 299.

3. Filed, C. B.; Campbell, J. E.; Lobell, D. B. Biomass energy: the scale of the potential resource. *Trends Ecol. Evol.* **2007**, *23*, 65

4. Abbey, C. Supercapacitor Energy Storage for Wind Energy Applications. *IEEE Trans. Ind. Appl.* **2007**, *43*, 769

5. Chu, B.; Zhou. X.; Ren, K.; Neese, B.; Lin, M.; Wang, Q.; Bauer, F.; Zhang, Q. M. A. A Dielectric Polymer with High Electric Energy Density and Fast Discharge Speed. *Science* **2006**, *313*, 334.

6. Mimikou, M. A.; Baltas, E. A. Climate change impacts on the reliability of hydroelectric energy production. *Hydrolog. Sci. J.* **1997**, *42*, 661.

7. Armand, M.; Tarascon, J.-M. Building better batteries. *Nature*, **2008**, *451*, 652.

8. Weber, A. Z.; Mench, M. M.; Meyers, J. P.; Ross, P. N.; Gostick, J. T.; Liu, Q. Redox flow batteries: a review. *J. Appl. Electrochem.* **2011**, *41*, 1137.

9. Chalk, S. G.; Miller, J. F. Key challenges and recent progress in batteries, fuel cells, and hydrogen storage for clean energy systems. *J. Power Sources* **2006**, *159*, 73.

10. Ramli, M. A. M.; Hiendro, A.; Twaha, S. Economic analysis of PV/diesel hybrid system with flywheel energy storage. *Renew. Energy* **2015**, *78*, 398.

11. Lund, H.; Salgi, G. The role of compressed air energy storage (CAES) in future sustainable energy systems. *Energy Convers. Manag.* **2009**, *50*, 1172.

12. Kinjo, T.; Senjyu, T. Output Levelling of Renewable Energy by Electric Double-Layer Capacitor Applied for Energy Storage System. *IEEE Trans. ENERGY CONVER.* **2006**, *21*, 221.

13. Giri, S.; Ghosh, D.; Das, C. K. Growth of Vertically Aligned Tunable Polyaniline on Graphene/ZrO2 Nanocomposites for Supercapacitor Energy-Storage Application. *Adv. Funct. Mater.* **2014**, *24*, 1312.

14. Parizh, M.; Kalafala, A. K.; Wilcox, R. Superconducting Magnetic Energy Storage for Substation Applications. *IEEE Trans. Appl. Supercond.* **1997**, *7*, 849.

15. Lavan, Z.; Thompson, J. Experimental study of thermally stratified hot water storage tanks. *Sol. Energy* **1997**, *19*, 519.

16. Brosseau, D.; Kelton, J. W.; Ray, D.; Edgar, M.; Chisman, K.; Emms, B. Testing of Thermocline Filler Materials and Molten-Salt Heat Transfer Fluids for Thermal Energy Storage Systems in Parabolic Trough Power Plants. *J. Sol. Energy Eng.* **2005**, *127*, 109.

17. Luo, Z.; Wang, C.; Xiao, G.; Ni, M.; Cen, K. Simulation and experimental study on honeycomb-ceramic thermal energy storage for solar thermal systems. *Appl. Therm. Eng.* **2014**, *73*, 622.

18. Moller, K. T.; Jensen, T. R.; Akiba, E.; Li, H.-W. Hydrogen – A sustainable energy carrier. *Pro. Nat. Sci.-Mater.* **2017**, *27*, 34.

19. Zygadlo, M.; Kotowski, J.; Oko, J. Green computing and energy storage systems. *E3S Web Conf.* **2018**, *44*, 00202.

20. Yang, Z.; Zhang, J.; Kintner-meyer, M. C. W.; Lu, X.; Choi, D.; Lemmon, J. P.; Liu, J. Electrochemical Energy Storage for Green Grid. *Chem. Rev.* **2011**, *111*, 3577.

21. Conway, B. E. Transition from "Supercapacitor" to "Battery" Behavior in Electrochemical Energy Storage. *J. Electrochem. Soc.* **1991**, *138*, 1539.

22. Cai. Q.; Brett, D. J. L.; Browning, D.; Brandon, N. P. A sizing-design methodology for hybrid fuel cell power systems and its application to an unmanned underwater vehicle. *J. Power Sources* **2010**, *195*, 6559.

23. Besenhard, J. O.; Winter, M. Advances in Battery Technology: Rechargeable Magnesium Batteries and Novel Negative-Electrode Materials for Lithium Ion Batteries. *ChemPhysChem* **2002**, *3*, 155.

24. Divya, K. C.; Ostergaard, J. Battery energy storage technology for power systems—An overview. *Electr. Pow. Syst. Res.* **2009**, *79*, 511.

25. Guo, Y.-G.; Hu, J.-S.; Wan, L.-J. Nanostructured Materials for Electrochemical Energy Conversion and Storage Devices. *Adv. Mater.* **2008**, *20*, 2878.

26. Bar-Tow, D.; Peled, E.; Burstein, L. A Study of Highly Oriented Pyrolytic Graphite as a Model for the Graphite Anode in Li-Ion Batteries. *J. Electrochem. Soc.* **1999**, *146*, 824.

27. Fergus, J. W. Recent developments in cathode materials for lithium ion batteries. *J. Power Sources* **2010**, *195*, 939.

28. McMilan, R.; Slegr, H.; Shu, Z. X.; Wang, W. Fluoroethylene carbonate electrolyte and its use in lithium ion batteries with graphite anodes. *J. Power Sources* **1999**, *81*, 20.

29. Huang, X. Separator technologies for lithium-ion batteries. *J. Solid State Electrochem.* **2010**, *15*, 649.

30. Chen, H.; Qiu, X.; Zhu, W.; Hangenmuller, P. Synthesis and high rate properties of nanoparticled lithium cobalt oxides as the cathode material for lithium-ion battery. *Electrochem. Commun.* **2002**, *4*, 488.

31. Ammundsen, B.; Paulsen, J. Novel Lithium-Ion Cathode Materials Based on Layered Manganese Oxides. *Adv. Mater.* **2001**, *13*, 943.

32. Hu, L.-B.; Wu, F.-Y.; Lin, C.-T.; Khlobystov, A. N.; Li, L.-J. Graphene-modified LiFePO4 cathode for lithium ion battery beyond theoretical capacity. *Nat. Commun.* **2013**, *4*, 1687.

33. Joho, F.; Rykart, B.; Imhof, R.; Novak, P.; Spahr, M. L.; Monnier, A. Key factors for the cycling stability of graphite intercalation electrodes for lithium-ion batteries. *J. Power Sources* **1999**, *81*, 243.

34. Zhong, K.; Xia, X.; Zhang, B.; Li, H.; Wang, Z.; Chen, L. MnO powder as anode active materials for lithium ion batteries *J. Power Sources* **2010**, *195*. 3300.

35. Martin, C.; Alias, M.; Christien, F.; Crosnier, O.; Delanger, D.; Brousse, T. Graphite-Grafted Silicon Nanocomposite as a Negative Electrode for Lithium-Ion Batteries. *Adv. Mater.* **2009**, *21*, 4735.

36. Palacin, M. R. Recent advances in rechargeable battery materials: a chemist's perspective. *Chem. Soc. Rev.* **2009**, *38*, 2565.

37. Lu, J.; Chen, Z.; Pan, F.; Cui, Y.; Amine, K. High-Performance Anode Materials for Rechargeable Lithium-Ion Batteries. *Electrochem. Energy Rev.* **2018**, *1*, 35.

38. Wu, X.-L.; Guo, Y.-G. Rational Design of Anode Materials Based on Group IVA Elements (Si, Ge, and Sn) for Lithium-Ion Batteries. *Chem. Asian J.* **2013**, *8*, 1948.

39. Tian, H.; Xin, F.; Wang, X.; He, W.; Han. W. High capacity group-IV elements (Si, Ge, Sn) based anodes for lithium-ion batteries. *J. Materionmics* **2015**, *1*, 153.

40. Kennedy, T.; Brandon, M.; Ryan, K. M. Advances in the Application of Silicon and Germanium Nanowires for High-Performance Lithium-Ion Batteries. *Adv. Mater.* **2016**, *28*, 5696.

41. Teki, R.; Datta, M. K.; Krishnan, R.; Parker, T. C.; Lu, T.-M.; Kumta, P. M.; Koratkar, N.

Nanostructured Silicon Anodes for Lithium Ion Rechargeable Batteries. *Small* **2009**, *5*, 2236.

42. Song, T.; Hu, L.; Paik, U. One-Dimensional Silicon Nanostructures for Li Ion Batteries. *J. Phys. Chem. Lett.* **2014**, *5*, 720.

43. Ryu, J.; Hong, D.; Choi, S.; Park, S. Synthesis of Ultrathin Si Nanosheets from Natural Clays for Lithium-Ion Battery Anodes. *ACS Nano* **2016**, *10*, 2843.

44. Li, W.; Sun, X.; Yu, Y. Si-, Ge-, Sn-Based Anode Materials for Lithium-Ion Batteries: From Structure Design to Electrochemical Performance. *Small methods* **2017**, *1*, 1600037.

45. Xiao, W.; Zhou, J.; Yu, L.; Wang, D.; Lou, X. W. Electrolytic Formation of Crystalline Silicon/Germanium Alloy Nanotubes and Hollow Particles with Enhanced Lithium-Storage Properties. *Angew. Chem. Int. Ed.* **2016**, *55*, 7427.

46. Hu, W.-S.; Demir-Cakan, R.; Titirici, M.-M.; Muller, J.-O.; Schlogl, R.; Antonietti, M.; Maier, J. Superior Storage Performance of a Si@SiOx/C Nanocomposite as Anode Material for Lithium-Ion Batteries. *Angew. Chem. Int. Ed* **2008**, *47*, 1645.

47. Sim, S.; Oh, P.; Park, S.; Cho, J. Critical Thickness of SiO2 Coating Layer on Core@Shell Bulk@Nanowire Si Anode Materials for Li-Ion Batteries. *Adv. Mater.* **2013**, *25*, 4498.

48. Kim, H.; Cho, J. Superior Lithium Electroactive Mesoporous Si@Carbon Core−Shell Nanowires for Lithium Battery Anode Material. *Nano Lett.* **2008**, *8*, 3688.

49. Ge, M.; Rong, J.; Fang, X.; Zhou, C. Porous Doped Silicon Nanowires for Lithium Ion Battery Anode with Long Cycle Life. *Nano Lett.* **2012**, *12*, 2318.

50. Zhou, S.; Liu, X.; Wang, D. Si/TiSi2 Heteronanostructures as High-Capacity Anode Material for Li Ion Batteries. *Nano Lett.* **2010**, *10*, 860.

51. Tan, L. P.; Lu, Z.; Tan, H. T.; Zhu, J.; Rui, X.; Yan, Q.; Hng, H. H. Germanium nanowires-based carbon composite as anodes for lithium-ion batteries. *J. Power Sources* **2012**, *206*, 253.

52. Gao, X.; Luo, W.; Zhong, C.; Wexler, D.; Chou, S.-L.; Liu, H.-K.; Shi, Z.; Chen, G.; Ozawa, K.; Wang, J.-Z. Novel Germanium/Polypyrrole Composite for High Power Lithium-ion Batteries. *Sci. Rep.* **2014**, *4*, 6095.

53. Yu, W.; Yan, C.; Gy, L.; Lang, X.; Tang, K.; Zhang, L.; Hou, Y.; Wang, Z.; Chen, M. W.; Schmidt, O. G.; Maier, J. Three-Dimensional (3D) Bicontinuous Au/Amorphous-Ge Thin Films as Fast and High-Capacity Anodes for Lithium-Ion Batteries. *Adv. Energy Mater.* **2012**, *3*, 281.

54. Casimir, A.; Zhang, H.; Ogoke, O.; Amine, J. C.; Lu, J.; Wu, G. Silicon-based anodes for

lithium-ion batteries: Effectiveness of materials synthesis and electrode preparation. *Nano Energy* **2016**, *27*, 359.

55. Zhou, X.; Yin, Y.-X.; Wang, L.-J.; Gyu, Y.-G. Facile synthesis of silicon nanoparticles inserted into graphene sheets as improved anode materials for lithium-ion batteries. *Chem. Commun.* **2012**, *48*, 2198.

56. Ge, M.; Rong, J.; Fang, X.; Zhang, A.; Lu, Y.; Zhou, C. Scalable preparation of porous silicon nanoparticles and their application for lithium-ion battery anodes. *Nano Research* **2013**, *6*, 174.

57. Favors, Z.; Bay, H. H.; Mutlu, Z.; Ahmed, K.; Lonescu, R.; Ye, R.; Ozkan, M.; Ozkan, C. S. Towards Scalable Binderless Electrodes: Carbon Coated Silicon Nanofiber Paper via Mg Reduction of Electrospun SiO2 Nanofibers. *Sci. Rep.* **2015**, *5*, 8246.

58. Wang, H.; Tang, W.; Ni, L.; Ma, W.; Chen, G.; Zhang, N.; Liu, X.; Ma, R. Synthesis of silicon nanosheets from kaolinite as a high-performance anode material for lithium-ion batteries. *J. Phys. Chem. Solids* **2020**, *137*,109227.

59. Liu, M.; Ma, X.; Gan, L.; Xu, Z.; Zhu, D.; Chen, L. A facile synthesis of a novel mesoporous Ge@C sphere anode with stable and high capacity for lithium ion batteries. *J. Mater. Chem. A* **2014**, *2*, 17107.

60. Salihoglu, O.; Kahlout, Y. E. Doped Silicon Nanowires for Lithium Ion Battery Anodes. *Mater. Res.* **2019**, *22*, e20180303.

61. Shi, W.; Wu, S.; Shi, J.; Jin, W.; Yin, G. Al-Doped Ge as Anode Material for Rechargeable Ion Batteries: a Density Functional Theory Study. *Int. J. Electrochem. Sci.* **2016**, *11*, 559.

62. Klavetter, K. V.; Souza, J. P. D.; Heller, A.; Mullins, C. B. High tap density microparticles of selenium-doped germanium as a high efficiency, stable cycling lithium-ion battery anode material. *J. Mater. Chem. A* **2015**, *3*, 5829.

63. Nitta, N.; Wu, F.; Lee, J. T.; Yushin, G. Li-ion battery materials: present and future. *Mater. Today* **2015**, *18*, 252.

Chapter II. Revealing salt-expedited reduction mechanism for hollow silicon microsphere formation in bi-functional halide melts

2.1 Introduction

Crystallogen compounds have been the backbone of various energy applications[1-4], leading to the developments of further purification methods for its naturally occurring oxide forms. Elimination of oxygen elements from well-defined structure requires a high energy, in principle, which can be viable through gaseous reduction by hydrogen or natural gas[5], solvothermal reduction[6], and thermochemical reduction reaction (TRR)[7-10]. Among them, thermochemical process has been extensively investigated owing to its cost-effectiveness, scalability, precise quantification of precursors based on the stoichiometry, and versatility toward multiple choices of metal oxides[11-13]. The conversion of Si from SiO_2 through thermochemical process provides a general understanding on their mechanism under the given principle of Ellingham diagram and as-reduced semi-conducting Si materials have been particularly utilized as anodes in lithium-ion batteries (LIBs)[13-16].

Typical thermochemical process follows one-to-one exchange of oxygen atoms between metal reductants and SiO_2 initiated by a sufficient thermal energy (carbon for >1400 °C and metals for > 420 °C)[17]. As activated carbon or metal reductants undergo the explosive reactions of M (metal or carbon) + SiO_2 (s) → MO_2 (or carbon monoxide) + Si (s), easily etchable by-products are generated along with a large amount of exothermic heat. This extensive and accumulated energy of entire system will greatly increase the risk of explosion and accordingly, appropriate mediation of system energy should be addressed. For this purpose, salt-assisted thermochemical reactions are proposed where the molten salts absorb the heat of reactions (ΔE) and slow down the overall kinetics[13, 18-20]. However, even at this configuration, it is obvious that reactants are supposed to follow the above reaction path and molten salts perform the role of heat scavenger, which do not have any influence on types, spontaneity, and thermal redox pair of reactions.

The role of molten salts recently extended far beyond a kinetic controller and rather it effectively participated in the reduction process by providing a reactive medium to the system; Lin *et al.* introduced a low temperature molten salt process[21]. It was demonstrated that SiO_2 can be reduced in the presence of metallic aluminum (Al) and aluminum chloride ($AlCl_3$) molten salt medium at relatively low temperature of around 250 °C. Unlike a conventional understanding of thermochemical process, metal reductants are not directly activated by thermal energy from

outside but assumed to be activated by excessive molten salt streams, indicating that $AlCl_3$ molten salts take part in the reaction. Besides, the proposed driving force of this reaction is an ionization process which could occur to produce ions and electrons at a solvated state with a strong reducing power. In addition, Zhou *et al.* adapted the same experimental set up for a formation of Si hollow microspheres[22], while crucial questions, such as exact reaction mechanism of newly proposed reduction systems, a dramatic reduction at low reaction temperature, and influence of $AlCl_3$ in the overall systems, are still not unveiled. Although several possibilities were proposed in the previous works, it cannot fully elucidate the whole reaction mechanism of thermochemical process in the molten salt system at such a low temperature.

In this study, we establish the whole reaction pathway for the reduction of SiO_2 with metal reductants and $AlCl_3$ molten salts medium as follows: (I) Complex formation between Al and $AlCl_3$, (II) SiO_2 reduction with adsorbed Al-complex, and (III) recrystallization of Si seed to produce hollow porous Si sphere (HPSS) demonstrated by density function theory (DFT) calculations and consistent experimental results. In the calculated reaction mechanism, $AlCl_3$ molten salt contributes to the formation of Al-$AlCl_3$ complex, which subsequently promotes the reduction of the silicate surface at low temperature. A ligand of Al-$AlCl_3$ complex is readily separated from the complex into $AlCl_3$ or $AlCl_2^*$ and passes Cl to complex center Al until $AlCl^*$ is formed. Then, the remaining $AlCl^*$ draws oxygen atom from the SiO_2 surface. Successive reduction reaction results in the formation of aluminum oxychloride (AlOCl), the reduction of by-product, and the clustering of Si atoms to HPSS. The HPSS electrodes have a stable battery operation for a long electrochemical cycling, enabled by plenty of pores and void spaces to accommodate large volume change of Si anodes through *in-situ* transmission electron microscopy (TEM) validations. In particular, a large dimension of HPSS particles over 3 μm significantly increases the electrode density without further calendaring process and thus high volumetric energy density is attained both in half/full-cell demonstration.

2.2 Experimental method

Materials. Halloysite, Montmorillonite, Kaolinite, Nano clay, and nano-sized silica (10-20nm), anhydrous aluminum chloride ($AlCl_3$), and Hydrofluoric acid (HF, 49%) were obtained from Sigma-Aldrich. Micro-sized silica (1μm), aluminum metal, Hydrochloric acid (HCl, 35-37%) was purchased from Alfa Aesar, Angang, SAMCHUN, respectively. All of the chemicals were used without any purification.

Computational Modeling & Simulation Details. We investigated the molten $AlCl_3$ salt-expedited Si-reduction mechanism over silicate surface using Dmol^3 program[30-33]. The reduction mechanism was predicted to be a two-step reaction; the formation of metal complex, which is clustered $AlCl_3$ around atomic Al detached from metallic Al surface, and the reduction of silicate surface by the adsorbed complex. The most stable (111) surface of Al was used when the metal complex was investigated for the calculation. The silicate surface was a monolayer kaolinite, which is the dehydrated form of halloysite, because the reduction reaction occurs with the decomposed crumbs from the halloysite as shown in the experimental procedure. Even though kaolinite has a layered silicate structure, consisting of the corner-sharing SiO_4 sheet linked to the edge-sharing AlO_6 sheet, only reactions on SiO_4 sheet, i.e. kaolinite $(00\bar{1})$ surface, were taken into consideration for mechanism calculation in order to readily observe the formation of a new Si-Si bond. For the DFT calculation, we employed the Perdew-Burke-Ernzerhof (PBE) exchange-correlation functional[32] and DNP 4.4 basis set with the all-electron relativistic core treatment. The convergence criteria for energy, force, and displacement were set to 1×10^{-5} Ha, 0.002 Ha/Å, and 0.005 Å, respectively. To include the dispersion correction of the van der Waals effect, the Tkatchenko-Scheffler scheme was used[33]. In terms of model systems, we constructed two slab models for trilayer Al (111) and monolayer kaolinite $(00\bar{1})$, respectively (**Supplementary Figure 1**). Al metal slab model was constructed with the 3×3 supercell of (111) surface and 3 atomic layers and for the kaolinite slab, the 2×3 supercell of kaolinite $(00\bar{1})$ was used.

HPSS and HPSS@C Synthesis. In the Argon (Ar)-filled glove-box, 1.0 g of Halloysite was mixed with 0.8g of Al and 8.0g $AlCl_3$ in custom-made stainless steel (SS) reactor with completely sealed. This reactor was transferred to the furnace and then heated at

250 °C for 10 h under Ar atmosphere continuously. After cooling down, the reactor was brought out and as-synthesized product ($Si/SiO_2/AlOCl/AlCl_3$, (i)) was rinsed with deionized water (D.I water) for several times, followed by filtrating it with ethanol and D.I water and drying at 80 °C overnight ($Si/SiO_2/AlOCl$, (ii)). Then, $Si/SiO_2/AlOCl$ sample was leached with 1.0M HCl for 1h at 35 °C to remove the AlOCl, followed by same filtration and dry step (Si/SiO_2, (iii)). Finally, 5% HF treatment completely eliminate residual SiO_2 with same filtration and dry steps (HPSS). All silicon products using other silica precursors was synthesized by same procedure. Finally, for HPSS@C, HPSS was heated at 900 °C for 1 min in acetylene gas (C_2H_2, 99.9%) at a flow rate of 500 cc/min.

Materials characterization. The morphological analysis and elemental mapping was carried out by the field-emission scanning electron microscopy (FE-SEM, Nova 230, FEI) and scanning transmission electron microscopy (STEM, Titan 80-300/FEI) with EDX detector operated at 300kV. X-ray diffraction (XRD) pattern was acquired by using Bruker D8-advance, which were conducted at 3 kW using Cu Kα radiation in the θ range from 20° to 80°. Raman spectra was obtained by a confocal Raman (alpha 300R, WITec) with 532 nm of wavelength laser. Auto Physisorption Analyzer (ASAP2020 Analysis) was used for BET and BJH analysis to investigate the surface area and pore size. For checking carbon weight portion after carbon coating process, thermogravimetric analysis (TGA, Q500) was used with 10 °C/min ramping rate under oxygen gas (O_2) flow. The XPS (ThermoFisher, K-alpha) analysis were carried out to obtain quantitative/qualitative information on surface oxidation state of samples.

***In situ* TEM observation.** The solid state nanobattery was constructed to observe the electrochemical reaction in the real time as illustrated in **Figure 2-4a**. The samples were loaded on Al wire as the working electrode, which occupied one side of nanofactory STM holder. Li metal was scratched out by the tungsten (W) tip mounted on the other side of the holder as the counter electrode. This process was carried out in Ar-filled glove-box, then, the holder was transferred to the TEM. Li metal was shortly exposed to the air (< 2s) while lithium oxide (Li_2O) was formed to be a solid electrolyte in this system. The electrochemical reaction, lithiation/dethiation was driven by external bias applied to the nanobattery.

Electrochemical characterization. A slurry consisting of active materials, Super-P: poly (acrylic acid) (PAA)/ carboxymethyl cellulose (CMC) (1:1 weight ratio) in a weight ratio

of 80:10:10 were blade-coated on Cu foil with active loading level of 1.0-1.5mg cm^{-2}. 2032-type coin cells (Welcos) were assembled in an Ar-filled glove box using Li metal as the counter/reference electrode, a Celgard 2400 membrane (polyethylene) as the separator, and 1.3M $LiPF_6$ in a mixture of ethylcarbonate (EC) / dimethylcarbonate (DMC) (3:7 v/v) including 10 wt% Fluoroethylene carbonate (FEC) as the electrolyte, and 1M $LiPF_6$ as the lithium salt under Ar atmosphere. The electrochemical performance was evaluated by galvanostatic measurement using a battery cycler (Wonatech, WBCS-3000) in the operating voltage of 0.005-1.5V (1^{st} cycle) and 0.01-1.2V for further cycles at room temperature. In full-cell test, the $LiCoO_2$ (LCO) was adopted as cathode materials with a N/P ratio of ~1.1. The cathode was fabricated with active materials, Super-P, and polyvinylidene fluoride binder (PVdF) in a weight ratio of 95:2.5:2.5. The mass loading level of the cathode was ~19 mg cm^{-2}. Th full-cells were performed in the operating voltage of 2.5-4.2V.

2.3 Results and discussion

Whole reaction pathway of low temperature aluminothermic reduction reaction (LTARR). The overall procedure to produce HPSS is illustrated in Figure 2-1a. When the mixture, composed of various silica sources, metallic Al, and dry $AlCl_3$, was heated at well above the melting point of $AlCl_3$ (~192 ℃), the LTARR favorably occurred inside a home-made closed reactor. As the reaction proceeded to form a molten salt, silica was disintegrated into crumbs and reduced gradually into the Si to still separate each other. Afterwards, as-produced Si seeds underwent the recrystallization process, assembling themselves to the hollow and porous structure of Si microsphere. Herein, the reduction mechanism on disintegrated silica crumbs was investigated by the DFT calculation (see computational modeling and simulation details in experimental method). In order for the reduction reaction to occur at such a lower temperature than the melting point of metallic Al (~660°C), Al was predicted to be solvated by the molten salts to form a complex. The reduction mechanism is found as a two-stage reaction undergoing two paths; the formation of Al-centered complex with $AlCl_3$ salts and the reduction of silica surface by adsorbed Al-$AlCl_3$ complex (Figure 2-1b). Unlike the previous expectation on the reduction reaction by the activated Al[21, 23], the mechanism proposed here is the reduction reaction by the activated $AlCl^*$ from the ligand of the Al-$AlCl_3$ complex. In forming the activated $AlCl^*$, two reaction paths with slightly different reaction order are suggested from thermodynamic calculations; path a, in which the ligand $AlCl_3$ is solely separated from the Al-$AlCl_3$ complex and successive two-times transfers of Cl's take place, whereas path b, in which $AlCl_2^*$ is detached from Cl-sharing ligand formed through ligand rearrangement and undergoes the transfer of Cl. Detaching oxygen atoms by $AlCl^*$ from the silica surface resulted in the formation of aluminum oxychloride (AlOCl), the by-product of reduction, and a new Si-Si bond is formed. Successive reduction reactions, which generated many AlOCl molecules, could provide a clustering environment of Si atoms to be a Si seed. As confirmed by experimental works, Si seeds, which are made from successive reduction on SiO_2 crumbs, become recrystallized into spherical shell via localized Ostwald ripening process, and inner crystal seeds dissolve away to reduce the surface energy resulting the formation of HPSS.

Al dissolution in molten salts. For the initiation of the considered reduction reaction, the probable configurations of adsorbed salts and salt-solvated structures on Al metal surface were theoretically investigated. Since dimers and monomers coexist in the molten $AlCl_3$[24] and three $AlCl_3$ units can completely cover a single Al atom on the Al metal surface, two possible conformations of salts in molten state (*i.e.*, $3AlCl_3$ or $Al_2Cl_6 + AlCl_3$) were placed on the bare Al

metal surface, respectively. Here, we denoted the group of three separate $AlCl_3$ molecules as $3AlCl_3$, and the group of $AlCl_3$ dimer and monomer as Al_2Cl_6 + $AlCl_3$. More probable structure among them was determined by comparing the adsorption energies and the change of electronic structure by adsorbed salt molecules (Supplementary Figure 2). As $3AlCl_3$ adsorbed onto the surface, a larger adsorption energy (E_{ad}) was released than when Al_2Cl_6 + $AlCl_3$ were adsorbed. The surface charge of the bare Al metal was about 0.085*e* on average, where overall charge was lied in between 0.078*e* and 0.095*e*. When Al_2Cl_6 molecule was adsorbed on the surface, the partial charges of Al atoms around the adsorbent were slightly changed to 0.029*e* ~ 0.173*e.* However, in case of the adsorption of $3AlCl_3$, the Al charges near the adsorbents showed significant changes to -0.617*e* ~ 0.269*e*. Note that electrostatic potential (ESP) mapped electron density surface presents the chemical interaction between Al and $AlCl_3$ (Supplementary Figure 2e) in contrast to no interaction of Al_2Cl_6 with Al (Supplementary Figure 2f). As shown in Supplementary Figure 3a, we estimated that the Al dissolution required the energy about 1.14 eV, whereas a stable dissolution structure by Al_2Cl_6 + $AlCl_3$ could not be acquired. While an Al atom was detached from the metal surface by $3AlCl_3$, it was coordinated with Al and Cl atoms of two adjacent $AlCl_3$ molecules at distances of 2.6 and 2.4 Å, respectively (Supplementary Figure 3b-d); the Al-$AlCl_3$ complex was formed.

Figure 2-2 shows an experimental observation of Al dissolution accelerated by the molten salts. Pristine Al metals have a typical spherical structure (1-10 μm) with a smooth surface, while its size should be maintained as smaller as possible to guarantee the reduction reaction as previously reported (Figure 2-2a)[21]. In order to realize the interaction between Al metal and $AlCl_3$ salts, the mixture of two components reacted in a same manner without silica sources. After the reaction, bulging parts in the products were assumed to be Al metals embedded in a solidified salt and this will be readily converted to an aluminum hydroxide matrix due to extremely sensitive nature of $AlCl_3$ to the air and the hydroxyl group, which understandably exists on Al metal surfaces as shown in Figure 2-2b, c and f (bottom). Upon its exposure to moisture in air, the composite products were oxygen-contaminated to form a dissolvable $Al(OH)_3$ and subsequent washing process with water removed any other impurities. Furthermore, AlOCl compounds were not formed in the absence of silica precursors, suggesting that AlOCl compounds should be produced with the interaction of both oxygen-included reactants materials and Al-$AlCl_3$ complex. Interestingly, the reacted surface of Al metals, which eliminate $AlCl_3$ and aluminum hydroxide matrix, was caved in or have a porous structure, otherwise it was completely collapsed out of shape (Figure 2-2d, e, and f (top)). However, it still had a crystalline property, which implies that excess amounts of salts fully enveloped the Al metals, and at the interface, $AlCl_3$ monomers from molten salts were adsorbed on the Al to promote the formation of Al-$AlCl_3$ complex. This result

is consistent with our theoretical calculation results and the fact that over-stoichiometric amounts of salts are required for the completion of reaction[21]. Dissolution of Al metals in the molten salts creates the reactive species in a form of metal-salt complex and it is expected to initiate the reduction reaction which counter the previous understanding and hypothesis.

Mechanistic study of AlOCl and Si seed formation. As mentioned earlier, three $AlCl_3$ molecules could entirely surround the fused Al atom dissolved in the molten salt in the form of Al-$AlCl_3$ complex, *i.e.* [$Al(AlCl_3)_3$] complex molecule. Central Al was coordinated within 3 Å by the surrounding salt ligands (Supplementary Figure 4a). To elucidate the mechanism of reduction reaction on silica surface, particularly kaolinite surface in this study, we traced the step-by-step pathway to form a new Si-Si bond and the by-product of reduction, AlOCl[20]. The first mechanism considered was the reduction by Al center serving as an activated reductant during the mechanism, as proposed in other works[21, 25]. However, the reduction mechanism by Al center (denoted as path 0 in Supplementary Figure 4b) was not preferred because of high activation energy (2.01 eV) caused by the strong interaction of central Al with adjacent $AlCl_3$ molecules. Central Al atom did not fall off the ligand salt molecule, thus a large amount of energy was required for the Al to approach the surface close enough to dissociate the Si-O bonds. Instead, it was more preferential that the ligand was separated from the [$Al(AlCl_3)_3$] complex and adsorbed on the surface. Herein, we suggest another reaction mechanism to yield activated species from ligand. The reduction mechanism diverges into two paths, where the order of the reaction is slightly different to form the activated species from the [$Al(AlCl_3)_3$] complex, *i.e.* the ligand dissociation (path a) and Al activation (path b) mechanism (Figure 2-3). At the first intermediate state of the ligand dissociation mechanism (IM1-a), which had the activation energy (E_a) of 0.64 eV and heat of reaction (ΔE) of -0.41 eV, the ligand $AlCl_3$ itself was detached from the [$Al(AlCl_3)_3$] complex and solely adsorbed on the SiO_2 surface. On the other hand, at the corresponding state of the Al activation mechanism (IM1-b), the formation of Cl-sharing complex structure by ligand rearrangement required the less E_a (0.55 eV) and released the more ΔE (-0.72 eV), since the coordination bond between a $AlCl_3$ molecule and central Al need to be broken once in TS0-a, whereas it remained in TS0-b (Supplementary Figure 4c, d).

Subsequently, in IM2-a, a Cl^* atom of detached $AlCl_3$ was transferred to the Al-$AlCl_3$ complex ([$Al(AlCl_3)_2$]) and the remaining $AlCl_2^*$ interacted with two oxygens on silica surface with the E_a of 0.75 eV and ΔE of 0.48 eV. In IM2-b, the half of the Cl-sharing ligand was detached and adsorbed on silica surface in the form of activated $AlCl_2^*$, which strongly reacted with 3 oxygen atoms on the surface, thus resulting in the E_a of 0.79 eV and ΔE of 0.45 eV, respectively. From IM2 to IM3, the reaction paths of both mechanisms were similar in that a Cl^* atom was detached once more from $AlCl_2^*$ and the remaining $AlCl^*$ adsorbed to the center of the 6-membered ring

on silica surface. At this step, the heat of reaction was observed lower in path a due to the ligand rearrangement of $[Al(AlCl_3)_2Cl]^*$ complex structure to accept the transferred Cl^* (*i.e.*, 0.34 eV for path a and 0.74 eV for path b). As $AlCl^*$ reacted with oxygen in the SiO_2 surface, AlOCl was formed through the dissociations of strong Si–O bonds following the path a and path b with the highest E_a of 1.44 eV and 1.41 eV along with the ΔE of 1.05 eV and 0.97 eV, respectively. Subsequently, two Si atoms were left to form a new Si-Si bond. Overall, we suggest that Al activation mechanism (path b) provides a kinetically and thermodynamically favorable route although both reaction paths are likely to occur together because of the temperature as high as 250°C.

From our observations, the ligand $AlCl_3$ could make AlOCl, and Al atom from metallic Al worked as the activated chlorine acceptor at the center of complex structure. Additionally, we investigated whether the by-product of AlOCl formation (*i.e.*, $[Al(AlCl_3)_2Cl_2]^*$ complex structure) could be recycled though a reconstruction procedure. With adjacent $[Al(AlCl_3)_2Cl_2]^*$ complex molecules, mutual exchange of Cl^* atoms resulted in the formation of several $AlCl_3$ molecules and Al-centered new complex, which will act as a new reactant for further reduction reaction (Supplementary Figure 5). Through the complex reconstruction, three $[Al(AlCl_3)_2Cl_2]^*$ complexes are transformed into Al_2Cl_6 and $AlCl_3$ molecules as well as a new $[Al(AlCl_3)_2]$ complex (*i.e.*, $3[Al(AlCl_3)_2Cl_2]^* \rightarrow [Al(AlCl_3)_2] + 6AlCl_3$). In summary, the reaction formula considered with three $[Al(AlCl_3)_3]$ complexes in this study can be expressed as,

$$3Al + 9AlCl_3 + 3/2SiO_2 \rightarrow 3AlOCl + Al + 8AlCl_3 + 3/2Si$$

which is consistent with previous experimental suggestion.[21]

$$4Al + 2AlCl_3 + 3SiO_2 \rightarrow 6AlOCl + 3Si$$

Evolution of HPSS. Through step-by-step validations on overall reaction mechanism of low temperature reduction process, we revealed that molten salts served as a promoter for the Al metal dissolution and thus-stabilized complex structure broke the very strong Si–O bond, leading to the formation of Si–Si bond. As-produced Si seed had a relatively free motion in the salts stream at a temperature above its melting point, while it was self-assembled in a way of reducing the surface energy of particles upon cooling off (*i.e.*, spherical structure). However, concurrently generated AlOCl and small Si crystal seeds will be necessarily embedded together with remaining $AlCl_3$ salts in a Si sphere. As a result, these residues dissolved away and led to a construction of hollow and porous structure regardless of various silica sources (Supplementary Figure 6, 7).

Figure 2-4a-d shows stepwise SEM images of the HPSS prepared from halloysite clay minerals, which was chosen for its available purity and cost, as mentioned previously[21,22]. After the complete reduction, densely packed spheres are embedded in a stream of excessive solidified

molten salts. The subsequent water and leaching steps remove any other impurities and consequently lead to a pore generation both inside shells and at the core as shown in the inset of Figure 2-4d. The typical polycrystalline nature of HPSS was observed in high-resolution transmission electron microscopy (HR-TEM) images with lattice fringes of 0.19 nm spacing, corresponding to (220) plane and selected area electron diffraction (SAED) pattern (Figure 2-4e). The XRD pattern confirmed sequential phase transitions into the final Si and the formation of crucial by-products of aluminum oxychloride (AlOCl), which could further validate our proposed mechanism (Supplementary Figure 8). Based on the X-ray photoelectron spectroscopy (XPS) results, Al existed primarily as the AlOCl and Al metals, while HCl completely removes these compounds without any traces to prove that this LTARR method provide high-purity Si products, also corroborated by Si and O spectra (Figure 2-4g-i and Supplementary Figure 9).

Nitrogen sorption measurements were conducted to quantify the surface area and porosity of HPSS. During the post treatments, its value gradually increased as etching out the residual components (Al, AlOCl, amorphous Al_2O_3, and SiO_2) and the surface area of HPSS is 39.4 $m^2 g^{-1}$ with pore size of ~56 nm (Figure 2-4f, see detailed results in Supplementary Figure 10). In addition, various factors were investigated for further demonstration of this mechanism, such as reaction time, temperature, and existence of Al metal (Supplementary Figure 11-13). Apart from this variation, there are additional factors governing this reduction process. Size of metals, stoichiometry of reactants, and reaction environments are cases in point, while these issues have already discussed in previous report[21, 22], and are out of scope for this study. It should be noted that our mechanism could be directly applied to different metal centers for the complex structure as well as chlorine acceptor as discussed earlier, thus successfully producing a hollow and porous structured Si.

Electrochemical study. HPSS has comparable features of a porous shell and a core void available in a microparticle, which offers a viable choice for Si anodes, according to the recent novel designs[3, 4, 15, 26, 27]. For validation on capability of HPSS to accommodate volume changes, *in-situ* TEM analysis was carried out to monitor a dynamic behavior upon lithiation and delthiation with a nanobattery setup (Supplementary Figure 14). Before measurement, carbon coating layers were introduced to improve the electric conductivity of HPSS particle (denoted as HPSS@C, Supplementary Figure 15). Under a negative bias (-3 V), Li-ion diffuses gradually to the HPSS@C particle in Figure 5a to proceed the lithiation and at the end of lithiation for 50 min, a change in the outer diameter of the HPSS@C was negligible due to an inward void filling, even at the crystalline $Li_{15}Si_4$ phase (Figure 2-5b, d, and Supplementary Movie 1). During delithiation under a positive bias of 3 V for 22 min, amorphous Si was present, corresponding to the SAED pattern, and recovered to the original structure (Figure 2-5c, e, and Supplementary Movie 2). The

magnified TEM images of pristine state in Figure 2-5f and fully lithiated state of HPSS clearly show shell thickening and pore fillings as shown in Figure 2-5g. The shell expanded 22% and porous shell became dense with a high contrast, filling out both mesopores and macropores. It is notable that the filled pores were recovered after delthiation process, while the shells remained a little swelled to 17% with a great structural integrity in Figure 2-5h. Inner and outer diameters were estimated to calculate volume variation during lithiation/delithiation (Figure 2-5i). Surprisingly, the expansion of whole particle featured less than 10% and it recovered to only 4% swelled state with respect to the pristine. Although the swelling results for non-coated HPSS from *in-situ* analysis had similar values, it required a higher bias to proceed the lithiation, which indicated that carbon layers will facilitate the diffusion of Li-ions into the particles and further electrochemical properties were measured by using the HPSS electrodes (Supplementary Figure 16 and Movies 3,4).

The beneficial effects of HPSS structure on volume accommodation were further demonstrated by galvanostatic charge/discharge tests in both half-cell and full-cell configuration. The differential capacity curves are consistent with behavior of typical crystalline Si anodes (Supplementary Figure 17)[28]. Figure 2-6a shows rate-dependent voltage profiles in a potential window of 0.005-1.5 V and 0.01-1.2 V for initial cycle and subsequent cycles, respectively. HPSS@C electrode has an initial Coulombic efficiency of 91% with discharge capacity of 3494 mAh g^{-1}. The irreversible capacity loss originated from the formation of the solid electrolyte interphase (SEI) and reaction with native oxides[29]. The sufficient channels for electrolyte infiltration and microsphere structure of HPSS enable the electrode to be activated quickly and have such a high initial Coulombic efficiency. Despite bulky structure of HPSS, its electrode affords a fast charging ability up to 5C rate (1C = 3.5 A g^{-1}) with a reversible capacity of 1100 mAh g^{-1}, which is still 3 times higher than that of graphite anode (Supplementary Figure 18). Cycling stability of HPSS@C electrode was monitored for prolonged cycles. HPSS@C electrode delivered reversible capacity of 832 mAh g^{-1} after 800 cycles at 1C rate with an average Coulombic efficiency of 99.5%. This extended cycle life of the HPSS@C electrode can be ascribed to effective inward breathing during lithiation and pore restoration during delithiation (Figure 2-6b and Supplementary Figure 19). Sluggish diffusion of Li-ions through the microparticles can be simply redeemed by conductive carbon layers, compared to non-coated HPSS (Supplementary Figure 20). By extension, the full-cell evaluation was conducted with commercial $LiCoO_2$ (LCO) cathode in the potential window of 2.5-4.2 V. The cycling tests showed a stable capacity retention over 100 cycles with an end capacity of 2.39 mAh cm^{-2} at 0.2 C rate (Figure 2-6c and Supplementary Figure 21, 22). Since stable cycling and Li-ion diffusion kinetics have a close relation to structural stability and electrode swelling, post characterizations

were also carried out. Figure 2-6d shows a summary chart for electrode thickness change along with inset TEM images of cycled HPSS@C. It should be noted that electrodes expanded 56.4 % after 100 cycles without any pulverization or delamination (Figure 2-6e and Supplementary Figure 23) and have retained original structures with enough void spaces, which accords with improved electrochemical performances. Along with the structural stability and cyclic performance of HPSS@C in Supplementary Figures 24 and 25, Nyquist plots display low-charge transfer resistance after 50^{th} cycle due to fast electrode activation and shortened Li-ion diffusion path, compared with the results of HPSS that has exposed fresh Si surface to electrolyte, triggering thick or irregular formation of SEI layer on the surface.

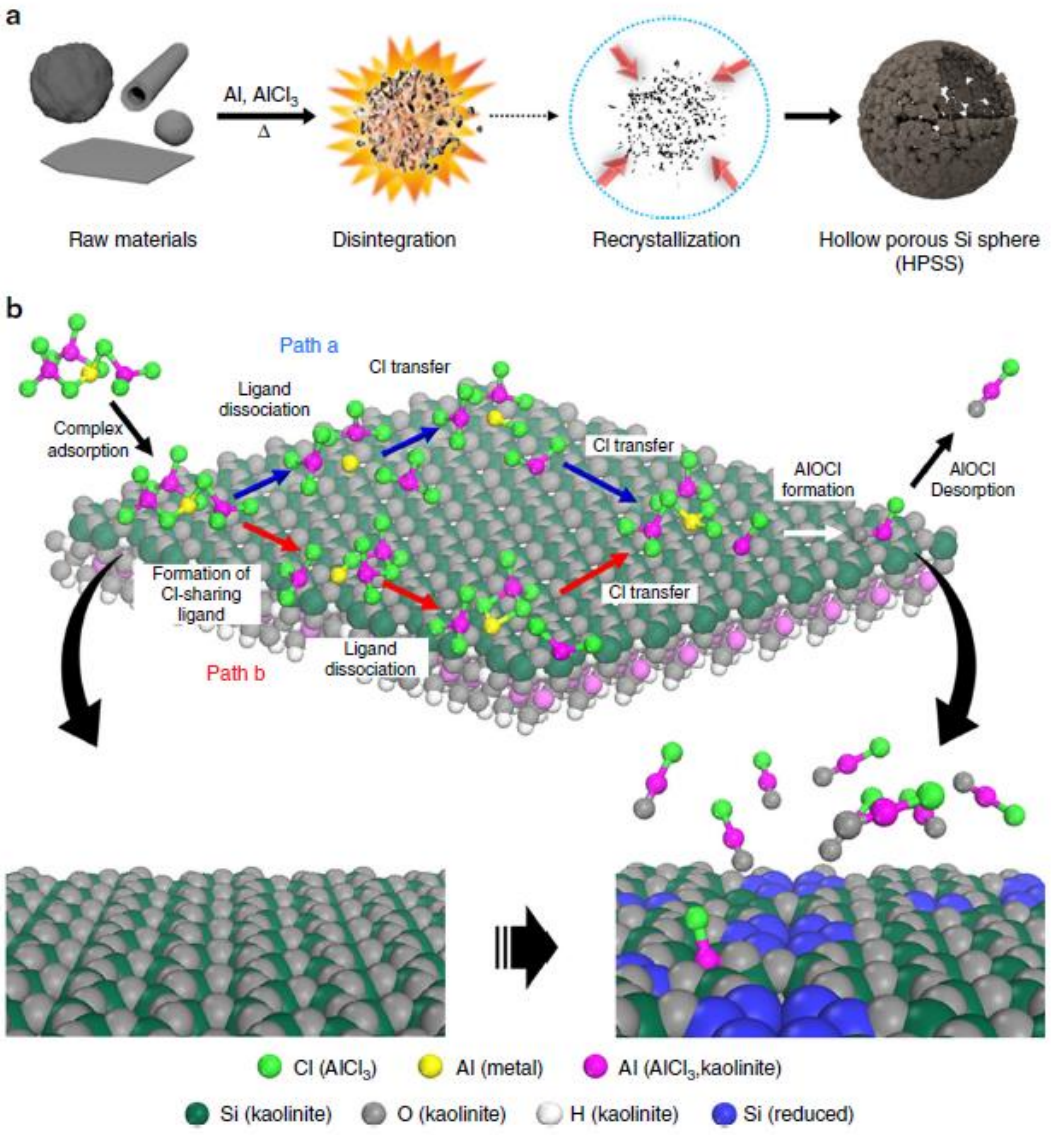

Figure 2-1. Schematic illustration of salt-expedited reaction. (a) Chemical reduction process to generate HPSS. Diversely structured SiO_2 raw materials are first disintegrated into smaller Si seeds and then it recrystallizes as time passes. Finally, after leaching out the by-products, HPSS can be obtained. (b) Theoretically tracked reaction mechanism on disintegrated silicate surface to form AlOCl. Path a and path b represent two different pathways to produce activated AlCl* from the adsorbed Al–$AlCl_3$ complex. Through path a or path b, the Al–$AlCl_3$ complex is dissociated, transferring Cl atoms to form AlCl*. Finally, AlOCl is formed by the as-made AlCl* reducing SiO_2 in both mechanisms. Atoms of surface and adsorbate are colored differently for the clear view. For kaolinite surface, Al and Si atoms are colored in pink and deep green, and O, H, and clustered Si atoms are colored in light gray, white, and blue, respectively. In the case of the adsorbate, Al and Cl in ligand, and Al center are colored in pink, green, and yellow, respectively.

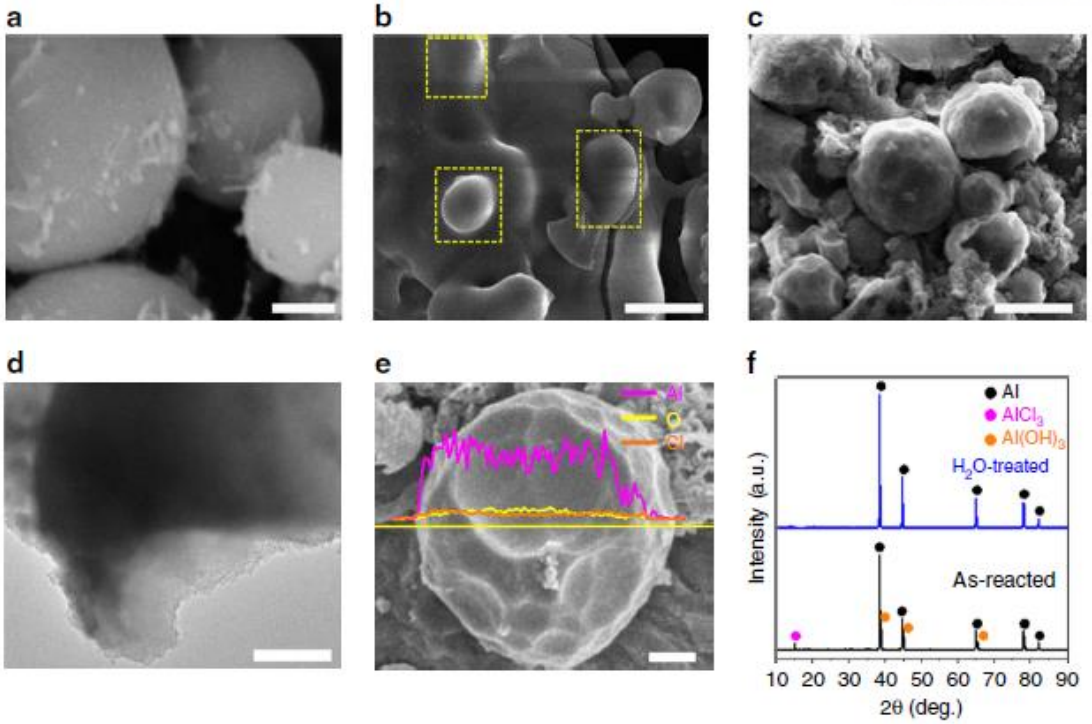

Figure 2-2. Al dissolution by molten salts. SEM images of (a) pristine Al and (b) as-reacted sample. Yellow boxes in b correspond to AlCl3/Al(OH)3 compounds formed on the Al metal surface. (c) SEM image, (d) TEM image, and (e) magnified SEM image with distribution profile of each atoms (magenta-Al, yellow-O, and orange-Cl) of samples after H2O treatment. (f) XRD patterns comparison of as-reacted sample and after H2O treatment. Scale bars, 4 μm (a–c); 500 nm (d); 1 μm (e).

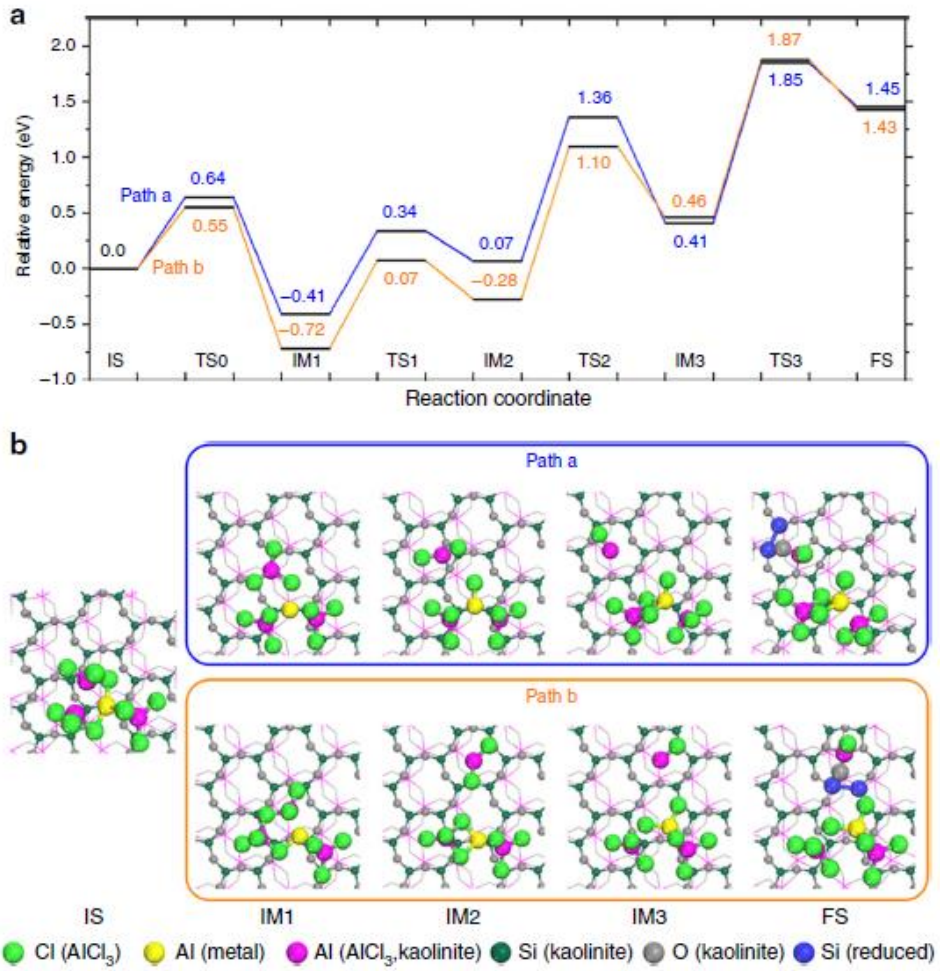

Figure 2-3. Reaction mechanism of salt-expedited Si reduction. (a) Reaction coordinate of two reaction mechanisms (i.e., path a and path b). (b) Optimized configurations of the reaction states of each mechanism: IS for initial state of adsorbed Al–AlCl3 complex on the SiO2 surface, IM1–IM3 for reaction intermediates, and FS for final state, where a Si–Si bond and AlOCl are formed. The numbers in a represent the relative energies of each state based on that of the IS. For the clear view, hydrogen atoms in kaolinite are omitted and bottom layers of kaolinite are presented by line model. The others are shown in ball-and-stick model. Color scheme is the same as Figure 2-1b.

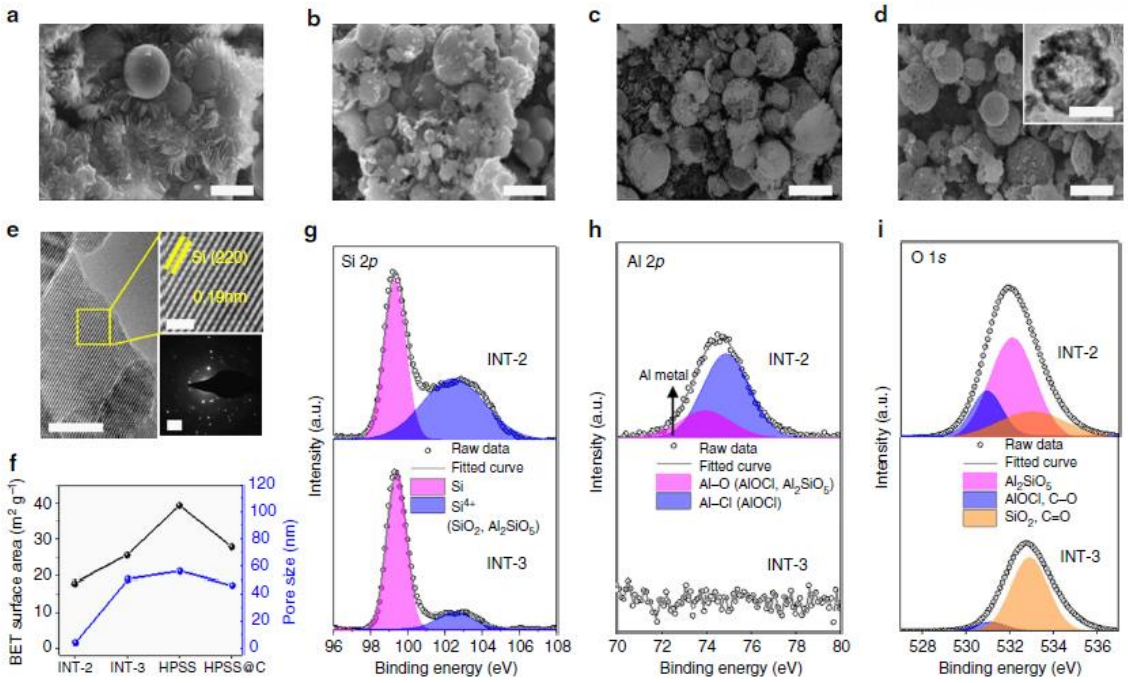

Figure 2-4. Structural evolution of HPSS. SEM images of samples at various stages; (a) INT-1, (b) INT-2, (c) INT-3, and (d) after HF treatment (denoted as HPSS, an inset corresponding to TEM image of HPSS). (e) Magnified TEM image of HPSS (an inset corresponding to High-resolution TEM image and selected area electron diffraction pattern). (f) BET surface area values and pore volumes of after-dissolving water (INT-2), after HCl treatment (INT-3), HPSS, and HPSS@C. (g–i) XPS spectra of Si 2p, Al 2p, and O1s of INT-2 and INT-3 samples. Scale bars, 4 μm (a–d); 5 nm, 2 nm, and 2 1/nm (e).

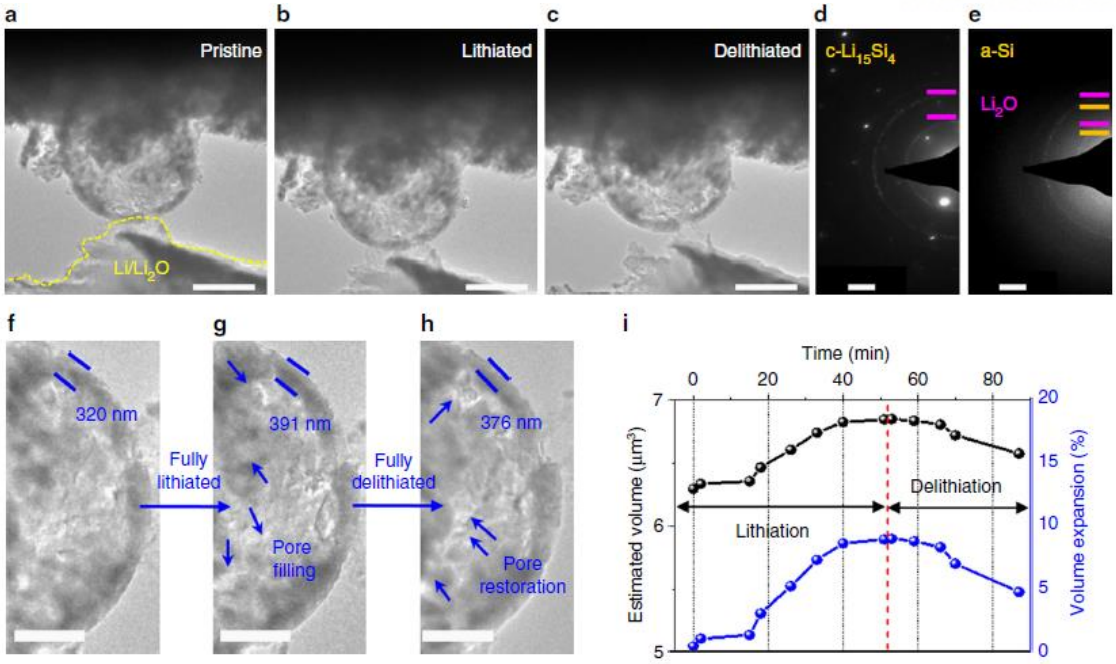

Figure 2-5. *In situ* electrochemical observation of a single HPSS-based particle. (a–c) Time-resolved TEM images of single HPSS@C particle during lithiation/delithiation with corresponding selected area electron diffraction (SAED) patterns of (d) fully lithiated and (e) delithiated samples under a potential of −3 V/3 V, respectively. Magnified TEM images of (f) pristine, (g) fully lithiated, and (h) delithiated HPSS@C particle, which illustrate thickened shell (22% expansion after lithiation) and pore filling/restoration showing no structural collapse. (i) Estimated volume and expansion ratio of HPSS@C particle during lithiation/delithiation. Scale bars, 1 μm (a–c); 2 1/nm (d, e); 500 nm (f–h).

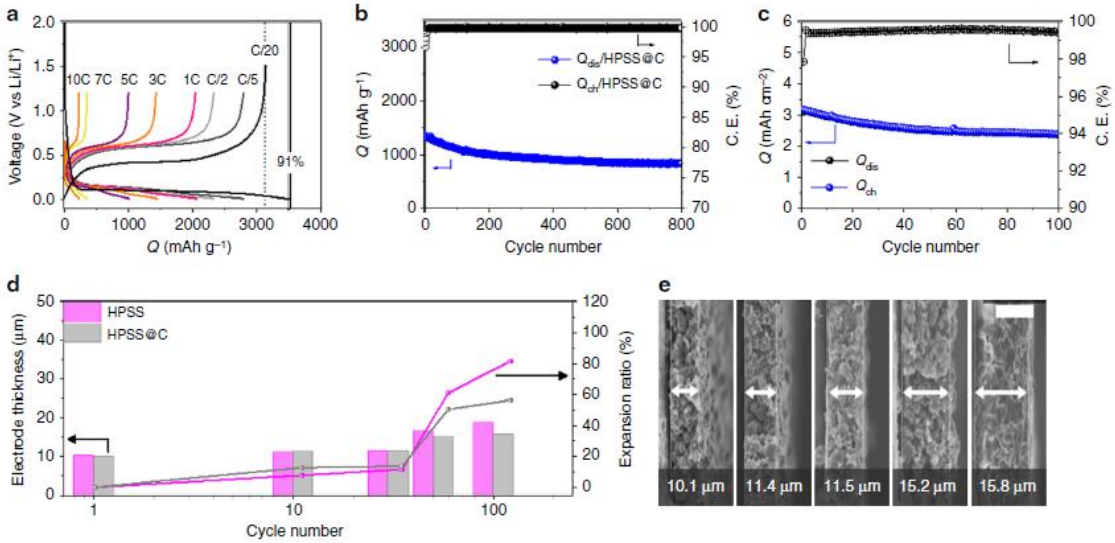

Figure 2-6. Electrochemical performance of HPSS-based electrode. (a) Galvanostatic charge–discharge profiles of HPSS@C electrode at different rates. (b) Cycling stability of HPSS@C electrode at 1C rate (3.5 A g^{-1}) for 800 cycles. (c) Cycling performance of full cell employing HPSS@C anode and LiCoO2 cathode for 100 cycles at 0.2C rate (0.62 mA cm^{-2}). (d) Ex situ electrode analysis for thickness change. (e) Cross-sectional SEM images of HPSS@C electrodes of pristine (10.1 μm), 10th (11.4 μm), 30th (11.5 μm), 50th (15.2 μm), and 100th cycle (15.8 μm). Scale bar, 10 μm (e).

2.4 Conclusion

In this study, we have demonstrated the step-by-step mechanism of LTARR on silicate surface in the presence of molten $AlCl_3$ salts, and electrochemical performance of as-prepared hollow porous Si sphere. By the DFT calculation as well as experimental validation, it showed that adsorption of molten $AlCl_3$ molecules on the Al surface emits quite large amount of heats promoting the detachment of Al atom in the form of Al-$AlCl_3$ complex. Remarkably, dissimilar to expectations of previous research on the reduction by activated Al^* atom forming Al_2O_3 in molten $AlCl_3$, the activated Al^* does not favorably adsorb on the silica surface compared to $AlCl_3$ since considerable amount of activation energy and heat of reaction are accompanied when detaching oxygen atoms.[23] In this regard, LTARR mechanism is considered as a ligand-promoted reduction, where the activated $AlCl^*$ produced from ligand reacted with oxygen atom of silica surface. Due to the dominant role of the salt molecule in this reduction, the mechanism we have suggested may show the universality of the mechanism of reduction to metals, which can form complex structures with metal halide molecules. In addition, through the reconstruction of $[Al(AlCl_3)_2Cl_2]^*$ molecules and the by-products of AlOCl formation, some fraction of active sites for succeeding reduction are preserved even after a series of reaction.

In terms of electrochemical performance, as-synthesized HPSS via LTARR through salt-expedited mechanism shows definitely prolonged cycles owing to pores on the surface and inside voids, which have the role of space-enhancing structure to moderately accept lithium ion during lithiation and the extraordinary morphology is still maintained without any breakdown. Further introduction of carbon coating layer can be utilized for improving lower intrinsic electronic conductivity of Si microparticles.

In this standard point to understand the part of molten salt in thermochemical reaction, we expect that the present proposed mechanism could be widely applied to other metals or metal salts system with SiO_2-containing compounds.

2.5 Reference

1. Pietsch, P.; Westhoff, D.; Feinauer, J.; Eller, J.; Marone, F.; Stampanoni, M.; Schmidt, V.; Wood, V. Quantifying microstructural dynamics and electrochemical activity of graphite and silicon-graphite lithium ion battery anodes. *Nat. Commun.* **2016**, *7*, 12909.

2. Billaud, J.; Bouville, F.; Margrini, T.; Villevieille, C.; Studart, A. R. Magnetically aligned graphite electrodes for high-rate performance Li-ion batteries. *Nat. Energy* **2016**, *1*, 16097.

3. Ko, M.; Chae, S.; Ma, J; Kim, N.; Lee, H.-W.; Cui, Y.; Cho, J. Scalable synthesis of silicon-nanolayer-embedded graphite for high-energy lithium-ion batteries. *Nat. Energy* **2016**, 1, 16113.

4. Liu, N.; Lu, Z.; Zhao, J.; McDowell, M. T.; Lee, H.-W.; Zhao, W.; Cui, Y. A pomegranate-inspired nanoscale design for large-volume-change lithium battery anodes. *Nat. Nanotechnol.* **2014**, 9, 187-192.

5. Choi, S.; Kim, J.; Hwang. D. Y.; Park, H.; Ryu, J.; Kwak, S. K.; Park, S. Generalized redox-responsive assembly of carbon-sheathed metallic and semiconducting nanowire heterostructures. *Nano. Lett.* **2016**, *16*, 1179-1185.

6. Liang, J.; Li, X.; Zhu, Y.; Guo, C.; Qian, Y. Hydrothermal synthesis of nano-silicon from a silica sol and its use in lithium ion batteries. *Nano Res.* **2015**, *8*, 1497-1504.

7. Bao, Z.; Weatherspoon, M. R.; Shian, S.; Cai, Y.; Graham, P. D.; Allan, S. M.; Ahmad, G.; Dickerson, M. B.; Curch, B. C.; Kang, Z.; Abernathy, H. W.; Summers, C. J.; Liu, M.; Sandhage, K. H. Chemical reduction of three-dimensional silica micro-assemblies into microporous silicon replicas. *Nature* **2007,** *446*, 172-175.

8. Choi, S.; Kim, J.; Choi, N.-S.; Kim, M. G.; Park, S. Cost-effective scalable synthesis of mesoporous germanium particles via a redox-transmetalation reaction for high-performance energy storage devices. *ACS Nano* **2015**, *9*, 2203-2212.

9. Lee, K. J.; Choi, S.; Park, S.; Moon, H. R. General recyclable redox-metallothermic reaction route to hierarchically porous carbon/metal composites. *Chem. Mater.* **2016**, *28*, 4403-4408 .

10. Choi, S.; Cho, Y.-G.; Kim, J.; Choi, N.-S.; Song, H.-K.; Wang, G.; Park, S. Mesoporous germanium anode materials for lithium-ion battery with exceptional cycling stability in wide temperature range. *Small* **2017**, *13*, 1603045.

11. Choi, S.; Bok, T.; Ryu, J.; Lee, J.-I.; Cho, J.; Park, S. Revisit of metallothermic reduction for macroporous Si: compromise between capacity and volume expansion for practical Li-ion battery. *Nano Energy* **2015**, *12*, 161-168.

12. Ryu, J.; Jang, Y. J.; Choi, S.; Kang, H. J.; Park, H.; Lee, J. S.; Park, S. All-in-one synthesis of mesoporous silicon nanosheets from natural clay and their applicability to hydrogen evolution. *NPG Asia Mater.* **2016**, *8*, e248.

13. Favors, Z.; Wang, W.; Bay, H. H.; Mutlu, Z.; Ahmed, K.; Liu, C.; Ozkan, M.; Ozkan, C. S. Scalable synthesis of nano-silicon from beach sand for long cycle life Li-ion batteries. *Sci. Rep.* **2014**, *4*, 5623.

14. Wang, W.; Favors, Z.; Lonescu, R.; Ye, R.; Bay, H. H.; Ozkan, M.; Ozkan, C. S. Monodisperse porous silicon spheres as anode materials for lithium ion Batteries. *Sci. Rep.* **2015**, *5*, 8781.

15. Xiao, Q.; Gu, M.; Yang, H.; Li, B.; Zhang, C.; Liu, Y.; Liu, F.; Dai, F.; Yang, L.; Liu, Z.; Xiao, X.; Liu, G.; Zhao. P.; Zhang, S.; Wang, C.; Lu, Y.; Cai, M. Inward lithium-ion breathing of hierarchically porous silicon anodes. *Nat. Commun.* **2015**, *6*, 8844.

16. Jung, D. S.; Ryou, M.-H.; Sung, Y. J.; Park, S. B.; Choi, J. W. Recycling rice husks for high-capacity lithium battery anodes. *Proc. Natl. Acad. Sci. USA* **2013**, *110*, 12229-12234.

17. Hutchison, S. G.; Richardson, L. S.; Wai, C. M. Carbothermic reduction of silicon dioxide – a thermodynamic investigation. *Metall. Trans. B* **1988**, *19*, 249-253.

18. Bok, T.; Choi, S.; Lee, J.; Park, S. Effective strategies for improving the electrochemical properties of highly porous Si foam anodes in lithium-ion batteries. *J. Mater. Chem. A* **2014**, *2*, 14195-14200.

19. Ryu, J; Hong, D.; Choi, S.; Park, S. Synthesis of ultrathin Si nanosheets from natural clays for lithium-ion battery anodes. *ACS Nano* **2016**, *10*, 2843-2851.

20. Liu, X.; Giordano, C.; Antonietti, M. A molten-salt route for synthesis of Si and Ge nanoparticles: chemical reduction of oxides by electrons solvated in salt melt. *J. Mater. Chem.* **2012**, *22*, 5454-5459.

21. Lin, N.; Han, Y.; Zhou, J.; Zhang, K.; Xu, T.; Zhu, Y.; Qian, Y. A low temperature molten salt process for aluminothermic reduction of silicon oxides to crystalline Si for Li-ion batteries. *Energy Environ. Sci.* **2015**, *8*, 3187-3191.

22. Zhou, Z.-W.; Liu, Y.-T.; Xie, X.-M.; Ye, X.-Y. Aluminothermic reduction enabled synthesis of silicon hollow microspheres from commercialized silica nanoparticles for superior lithium

storage. *Chem. Commun.* **2016**, *52*, 8401-8404.

23. Lin, N.; Han, Y.; Wang, L.; Zhou, J.; Zhou, J.; Zhu, Y.; Qian, Y. Preparation of nanocrystalline silicon from $SiCl_4$ at 200°C in molten salt for high-performance anodes for lithium ion batteries. *Angew. Chem. Int. Ed.* **2015**, *54*, 3822-3825.

24. Aarset, K.; Shen, Q.; Thomassen, H.; Richardson, A. D.; Hedberg, K. Molecular structure of the aluminum halides, Al_2Cl_6, $AlCl_3$, Al_2Br_6, $AlBr_3$, and AlI_3, obtained by gas-phase electron-diffraction and ab initio molecular orbital calculations. *J. Phys. Chem. A* **1999**, *103*, 1644-1652.

25. Yoshikawa, N.; Kikuchi, A.; Taniguchi, S. Anomalous temperature dependence of the growth rate of the reaction layer between silica and molten aluminum. *J. Am. Ceram. Soc.* **2002**, *85*, 1827-1834.

26. Li, X.; Gu, M.; Hu, S.; Kennard, R.; Yan, P.; Chen, X.; Wang, C.; Sailor, M. J.; Zhang, J.-G.; Liu, J. Mesoporous silicon sponge as an anti-pulverization structure for high-performance lithium-ion battery anodes. *Nat. Commun.* **2014**, *5*, 4105.

27. Li, Y.; Yan, K.; Lee, H.-W.; Lu, Z.; Liu, N.; Cui, Y. Growth of conformal graphene cages on micrometre-sized silicon particles as stable battery anodes. *Nat. Energy* **2016**, *1*, 15029.

28. Esmanski, A.; Ozin, G. A. Silicon inverse-opal-based macroporous materials as negative electrodes for lithium ion batteries. *Adv. Funct. Mater.* **2009**, *19*, 1999-2010.

29. Yen, Y.-C.; Chao, S.-C.; Wu, H.-C.; Wu, N.-L. Study on solid-electrolyte-interphase of Si and C-coated Si electrodes in lithium cells. *J. Electrochem. Soc.* **2009**, *156*, A95-A102.

30. Delley, B. An all-electron numerical-method for solving the local density functional for polyatomic-molecules. *J. Chem. Phys.* **1990**, *92*, 508-517.

31. Delley, B. From molecules to solids with the DMol3 approach. *J. Chem. Phys.* **2000**, *113*, 7756-7764.

32. Perdew, J. P.; Burke, K.; Ernzerhof, M. Generalized gradient approximation made simple. *Phys. Rev. Lett.* **1996**, *77*, 3865-3868.

33. Tkatchenko, A.; Scheffler, M. Accurate molecular van der waals interactions from ground-State electron density and free-atom reference data. *Phys. Rev. Lett.* **2009**, *102*, 073005.

35. Bell, S.; Crighton, J. S. Locating transition states. *J. Chem. Phys.* **1984**, *80*, 2464–2475.

36. Halgren, T. A.; Lipscomb, W. N. The synchronous-transit method for determining reaction pathways and locating molecular transition states. *Chem. Phys. Lett.* **1977**, *49*, 225–232.

Chapter III. Atomic-scale combination of germanium-zinc nanofibers for structural and electrochemical evolution

3.1 Introduction

With the increase in energy consumption and the development of large-scale devices such as electric vehicles (EVs), the demand for rechargeable energy storage systems, especially lithium-ion batteries (LIBs), has sharply increased[1-10]. However, existing LIBs face many limitations due to their low energy density. So far, various anode candidates that possess a higher specific capacity have been suggested to substitute graphite with theoretical capacity (372 mAh g^{-1}). Among the many candidates, germanium (Ge) is one of the most promising anode materials owing to its high gravimetric and volumetric capacity (1396 mAh g^{-1} and 7366 Ah L^{-1}, respectively, for $Li_{3.75}Ge$), which are comparable to those of Si; reasonable Li ion diffusivity and electronic conductivity[11-13]. Furthermore, Ge-based anodes operate at a low operating voltage (< 0.5 V), resulting in a high potential window when assembled as full cells[14]. Nevertheless, pure Ge compounds are expensive, and the synthesis of pure Ge nanostructures is rather complicated. As a result, oxygen-containing Ge (GeO_x) has recently drawn attention as an alternative to pure Ge due to the following merits: a higher theoretical capacity (2152 mAh g^{-1}), reduced cost, and superior chemical stability[15-18]. However, GeO_x also triggers a large volume change during lithiation process, resulting in fatal capacity decay upon cycling with the loss of electrical contacts, fracturing, and pulverization, along with the continuous formation of unwanted solid electrolyte interphase (SEI) layers. Additionally, the poor electronic conductivity of GeO_x limits electron transfer at high current density, which remains a challenge to realizing high-power/high-energy-density anode materials for advanced LIBs.

To overcome the problems mentioned above, two main strategies have been attempted: (i) one approach is to synthesize low-dimensional Ge/GeO_x nanomaterials (nanoparticles, nanotubes, nanowires, and nanofibers (NFs)), which can mitigate a large volume change of > 300%, shorten the Li ion diffusion length, and suppress contact loss and unstable SEI layer formation[13, 19-21]; (ii) the other approach is to combine Ge/GeO_x with foreign atoms (carbon, metal, or metal oxide) and/or a protective layer (carbon), which allows additional electron pathways through enhanced conductivity[22-27]. Nevertheless, a feasible strategy to enhance both the structural and electrochemical stability of GeO_x-based anodes has yet to be fully investigated; such a strategy is critical to realize high-performance anodes for sustainable LIBs.

In this work, we propose an intriguing defect engineering of one-dimensional Ge-based materials through the intermolecular incorporation of Zn element. The as-synthesized oxygen-defective and intermolecularly distributed Ge-Zn NFs (oxygen-deficient Ge-Zn composite NFs, denoted as O-dGZNFs), which is prepared by a facile electrospinning followed by subsequent thermal treatment, feature a well-mixed atomic distribution of Ge-Zn-O with disordered Ge. In addition, this unique structure limits the sublimation of Ge or GeO_x, a chronic problem in solid-gas reduction reactions[28]. *In situ* transmission electron microscopy/electrochemical impedance spectroscopy (TEM/EIS) characterizations further demonstrate the significantly improved structural stability and electronic conductivity. Unlike previous work on $Zn_xGe_{1-x}O$ composites showing inferior electrochemical performance (510 mAh g^{-1} at 0.5 A g^{-1})[29], O-dGZNFs electrode exhibits ultrahigh cycling stability (capacity retention of 73%), a reversible capacity of 546 mAh g^{-1} for 1000 cycles at 3.0 C-rate and exceptional rate capability (capacity of ~50% at 20 C-rate compared to that of 0.2 C-rate). In a full cell, a high energy density of 335 Wh kg^{-1} (565 Wh L^{-1}) was achieved after the 1st cycle, and a stable charge/discharge characteristic was observed with coulombic efficiency of 99.4% during 400 cycles; the designed material shows great potential for practical energy storage systems.

3.2 Experimental method

Materials. Germanium oxide (GeO_2, 99.995%) was purchased from Kojundo Chemical Lab. Co., LTd.. Poly(vinyl pyrrolidone) (PVP, M_w ~1,300,000 g mol^{-1}) and zinc nitrate hexahydrate ($Zn(NO_3)_2 \cdot 6H_2O$, reagent, 98%) were purchased from Sigma Aldrich. Germanium (Ge) was purchased from Alfa Aesar for FT-EXAFS measurement of reference Ge. All the chemicals were used without further purification.

Synthesis of O-iGNFs and O-iGZNFs. O-iGNFs and O-iGZNFs were prepared *via* electrospinning and a subsequent calcination step. For the preparation of O-iGNFs, 0.4 g of GeO_2 was dissolved in 50 mL of deionized (DI) water at 90 °C. Then, 7.5 g of PVP was added into the solution and stirred at 500 rpm for 6 h. Then, the electrospinning solution was loaded into a syringe, where the electrospinning process took place using an electrospinning tool (Machine 1 Type, NanoNC). The electrospinning was conducted with the following conditions: a flow rate of 0.5 mL h^{-1}, an applied voltage of 16.0 kV, and a distance of 15 cm between the tip of the syringe and the current collector using a 25-gauge needle. The as-spun NFs were calcined at 250 °C for 1 h and 500 °C for 2 h at a ramping rate of 5 °C min^{-1} in a box furnace (MF-22G, JEIO TECH). For the preparation of O-iGZNFs, a solution mixture with specific amounts of GeO_2 and Zn $(NO_3)_2 \cdot 6H_2O$ (98%) (Supplementary Figure 2b) was added to the electrospinning solution and subjected to identical electrospinning conditions and subsequent calcination. As a result, O-iGNFs and O-iGZNFs were successfully synthesized.

Synthesis of O-dGNFs and O-dGZNFs. As-synthesized O-iGNFs and O-iGZNFs underwent a reduction process in a quartz furnace (OTF-1200X-II, MTI corporation) filled with argon (Ar). In this process, the furnace was heated to 600 °C under Ar at a ramping rate of 5 °C min^{-1}, and once the temperature reached an expected value, the atmosphere was changed to an Ar and hydrogen gas mixture (Ar/H_2 (96/4, v/v)) and maintained for 1 h. Afterward, the furnace was filled again with Ar instead of Ar/H_2 and cooled spontaneously to room temperature.

Material characterization. Morphological images were acquired by field-emission scanning electron microscopy (FE-SEM, Nova 230, FEI) operating at 10 kV and environmental transmission electron microscopy (ETEM, FEI) with an accelerating voltage of 300 kV under vacuum conditions. In addition, energy-dispersive X-ray (EDX) detection combined with scanning transmission electron microscopy (STEM, FEI) was used to analyze the elemental distribution and the amounts of elements. Raman spectra were collected with a confocal Raman spectrometer (alpha 300R, WITec) with a laser wavelength of 532 nm. XRD patterns were

obtained by using a Bruker D8-advance with 3 kW Cu Kα radiation and wavelengths in the range of 20° to 80°. An inductively coupled plasma (ICP) instrument combined with a mass spectrometer (LC-ICP/MS, PerkinElmer, ELAN DRC-II) and elemental analyzer (EA, Flash 2000) were used to examine the elemental content. X-ray photoelectron spectroscopy (XPS) (K-alpha, ThermoFisher) was used for surface analysis. X-ray absorption near-edge structure (XANES) and extended X-ray absorption fine structure (EXAFS) analyses were conducted at the BL6D beamline of the Pohang light source (PLS-II) under a current of 300 mA with 3.0 GeV.

***In situ* electrochemical observations.** For *in situ* transmission electron microscopy (*in situ* TEM) measurements using ETEM, an open cell, which was composed of Li metal for the counter electrode and samples for the working electrode, was manufactured for the observation of electrochemical reactions in real time. This open cell could be operated with a scanning tunneling microscope (STM) holder. The working electrode was held on an Al nanowire, and the counter electrode was loaded on a W tip in an Ar-filled glove box on each side of the holder. Then, the holder was transferred to the ETEM while exposed to air for less than 2 s. During the movement, a very thin Li_2O layer was coated on the Li metal and used as the solid electrolyte. For Li^+ ion insertion/extraction, a negative/positive potential was applied to the STM holder by an external bias, -2 V/2 V for Li ion insertion/extraction. A negative bias drove Li^+ to the samples across the Li_2O layer on the Li metal via the potential difference between the two electrodes, and the samples reacted with Li^+, consistent with lithiation. In contrast, a positive bias induced the delithiation step by extracting Li^+ from the samples. The *in situ* conductivity test was almost the same as the *in situ* lithiation/delithiation observation, except there was no loading of Li metal. Individual single NFs loaded on platinum (Pt) nanowires could be directly contacted with only the tungsten (W) probe, and an external bias was applied in the range of -10 V to 10 V to measure the electrical conductivity. For *in situ* electrochemical impedance spectroscopy (*in situ* EIS), a set of multiple impedance spectra was measured every 30 min by galvanostatic EIS in constant current mode (1.0 C) during lithiation/delithiation since the potentiostat of the *in situ* EIS system consisted of two different channels: one channel was for measuring impedance spectra, and the other channel was for recording voltage profiles. Input signals were generated by the superposition of sinusoidal current waves of 10 mA amplitude at 200 kHz to 1 Hz (VSP-300, BioLogic).

Electrochemical measurements. To prepare the electrodes, a viscous slurry consisting of the active materials, super-P carbon black as a conductive material, and poly(acrylic acid) (PAA)/carboxymethyl cellulose (CMC) (1:1 weight ratio) as a binder with a weight ratio of 70:15:15 (w/w/w) was cast on Cu foil with a loading mass of 1.0-1.3 mg cm^{-2}. Then, the electrode was transferred into an Ar-filled glove box to act as the working electrode in 2016-type coin cells (Welcos) with Li metal as a counter electrode, a polypropylene membrane (Celgard) as a separator,

and ethylene carbonate/diethyl carbonate (EC/DEC = 3:7, v/v) including 10 wt% fluoroethylene carbonate (FEC) and 1.3 M $LiPF_6$ salt as a liquid electrolyte. Galvanostatic measurements of half cells were conducted using a battery cycler (Wanatech, WBCS-3000) in the range of 0.005-1.5 V (1^{st} cycle) and 0.01-1.5 V (further cycles) at 25 °C. For full cells, Li metal was substituted with $LiCoO_2$ (LCO), while all the other components were identical. The LCO electrode was manufactured with LCO:Super-P:polyvinylidene fluoride (PVdF) binder with a weight ratio of 90:5:5 (w/w/w) and cast on Al foil (loading mass: 13 mg cm^{-2}). The full cells were evaluated in the operating voltage range from 2.5 to 4.29 V at 25 °C.

3.3 Results and discussion

Structural evolution of O-dGZNFs. Unstable Ge states during the reduction process result in unexpected sublimation, causing a lower yield and structural deformation. Zn atoms that are directly interconnected to GeO_2 could stabilize the Ge state owing to the robust Ge-Zn bonding. Based on the binary phase diagrams of various metals, Zn was carefully selected. Some metals (such as Cu and Fe) form alloys with Ge as verified by X-ray diffraction (XRD) analysis before and after reduction (Supplementary Figure 1a). Moreover, other kinds of metals (such as Ag, Au, Sb, and Sn) can be combined with Ge, but other limitations are present. For example, Ag and Au are very expensive, and synthetic conditions are difficult due to their sensitive precursors; Sb is difficult to mix with Ge in electrospinning solution; and Sn can be easily mixed with Ge, however undesired phases, i.e., partial Ge oxides and Sn oxides, are independently formed, limiting the generation of complete GeSn alloy at operating temperature (Supplementary Figure 3-1b). As a result, we selected Zn as an optimal element to synthesize O-dGZNFs. The synthetic process of oxygen-including Ge-Zn composite NFs (O-iGZNFs) and O-dGZNFs and their TEM images are displayed in Figure 3-1a. Similarly, oxygen-including Ge NFs (O-iGNFs) and oxygen-deficient Ge NFs (O-dGNFs) (control samples prepared without Zn) were prepared using the same process, and the elemental compositions of both O-dGNFs and O-dGZNFs along with their calcined samples were determined (Supplementary Figure 2). Although both O-dGNFs and O-dGZNFs have a high proportion of Ge, the Ge weight loss from O-iGZNFs to O-dGZNFs is less than that from O-iGNFs to O-dGNFs. An as-prepared electrospinning solution including a metal salt precursor (zinc nitrate hexahydrate/germanium oxide) and a poly(vinyl pyrrolidone) (PVP) was injected and directly transformed into polymer/metal ion composite NFs on a current collector, as shown in the scanning electron microscopy (SEM) image in Figure 3-1b. Then, upon calcination, the PVP chains were decomposed at approximately 450 °C (Supplementary Figure 3), while the metal ions were eventually oxidized by oxygen under ambient air during the calcination step; Ge and Zn ions were thus spontaneously mixed through intermolecular bonds in an amorphous phase (as shown in the TEM image in Figure 3-1, selected area electron diffraction (SAED) patterns in Figure 3-1c and XRD patterns in Supplementary Figure 4). The amorphous phase was maintained at 500 °C. However, when the calcination temperature increased to 600 and 650 °C, crystalline structures of GeO_2 and Zn_2GeO_4 were gradually developed (Supplementary Figure 5).

Afterward, the as-calcined NFs underwent a reduction process under H_2 gas *via a* solid-gas reduction reaction at 600 °C to remove oxygen atoms from the NFs (denoted as O-dGZNFs) while

maintaining a similar crystal structure in nanoscale (Figure 3-1d). The O-dGZNFs had a uniform distribution of Ge-Zn atoms, according to high-angle annular dark-field scanning transmission electron microscopy (HAADF-STEM) mapping (Figure 3-1e) without significant morphological changes or agglomeration (Supplementary Figure 6). As a result of this step, germanium-oxygen (Ge-O) bonds were reduced to Ge-Ge bonds with distorted d-spacing, whereas oxygen atom-incorporated Zn (Zn-O) remained in the amorphous phase without reduction owing to insufficient activation energy at the given temperature (Supplementary Figure 4 and 7). Additionally, higher structural disorder was observed in the O-dGZNFs than in the O-dGNFs without Zn (Supplementary Figure 4b). The main Ge metal peak of microstructure, representing the (111) plane in a crystal region of the O-dGZNFs, was slightly shifted due to the d-spacing increase and separated by the development of new kinds of bonds. We believe that this change is attributed to the atomic-level influence of Zn and structural distortion because Zn atom is theoretically larger than Ge atom. These XRD patterns directly demonstrate the bonding of Ge with foreign atoms in the NFs. Moreover, the high-resolution TEM (HR-TEM) image in Figure 3-1d microscopically shows no clear lattice fringe and amorphous SAED patterns, which attributed to the intermolecular Ge-Zn structure having homogeneous Ge-Zn-O bonding and distorted Ge clusters. The TEM images and SAED patterns of O-iGNFs and O-dGNFs are displayed in Supplementary Figure 8, showing similar crystal structures and morphology to those of O-iGZNFs and O-dGZNFs due to the dominant presence of large amounts of carbon and amorphous GeO_x in the Ge clusters.

To accurately confirm the chemical bonding, Raman spectra were analyzed and are shown in Figure 3-2a. The O-dGZNFs showed broad Ge-Ge bonds in the range of 280-305 cm^{-1} and independently exhibited oxygen-defective and asymmetric Ge-Zn-O bonds at 750 and 777 cm^{-1}, respectively, as well as partial Zn-O bonds (437 cm^{-1}). In contrast, Ge-O bonds at 445 cm^{-1} and broad Ge-Ge peaks were detected in the O-dGNFs[30-33]. The Raman spectra of both NFs confirmed that the amorphous-phase carbon was formed by the thermal decomposition of PVP, as determined from the intensity of the I_D/I_G ratios: 1.46 (O-dGNFs) and 1.30 (O-dGZNFs). The result indicates that oxygen-shared Ge and Zn exist in a state of intermolecular connection in the amorphous carbon matrix. Furthermore, the triggering of Ge-Ge distortion by this featured bond was proven through core-level X-ray photoelectron spectroscopy (XPS) spectra. Figure 3-2b and c display characteristic peaks related to Ge-Zn-O at approximately 1021, 1044 (Zn 2p), and 32 eV (Ge 3d), different from the case of O-iGNFs and O-dGNFs, as shown in Supplementary Figure 9[34,35]. Moreover, Fourier transform-extended X-ray absorption fine structure (FT-EXAFS) analysis in Figure 3-2d and e reveals that the Ge-Ge bonding length was elongated in the presence of Zn (Zn-Zn: 2.29 Å)[36]. The O-dGNFs lost Ge-O bonding at 1.38 Å showed an increase in the

peak intensity corresponding to Ge-Ge bonds at 2.14 Å, which is consistent with the value for reference Ge (2.14 Å)[37, 38]. In accordance with the XPS results in Supplementary Figure 9, the O-dGNFs still showed a partial GeO_x content in the NFs, and the O-dGZNFs also showed a peak corresponding to Ge-O at 1.38 Å even after reduction. However, the peak positions in the O-dGZNFs were slightly shifted to the right (to 1.67 and 2.17 Å from 1.38 Å and 2.14 Å, respectively) and did not perfectly overlap with Ge-O bonds as well as with the peak related to Ge-Ge bonds. This unusual result is attributed to the disordered Ge-Ge d-spacing by Ge-Zn intermolecular connections and the longer bonding length of intrinsic Zn-Zn than that of Ge-Ge. In addition, this delicate interconnection can prevent the chronic problem of Ge sublimation during the reduction of GeO_2. GeO_x and/or Ge gas molecules immediately after reduction can be vaporized without a phase transition to solid-state Ge metal due to their unstable state[39]. Core-level XPS spectra of C, N, and O for the O-iGNFs/O-iGZNFs and O-dGNFs/O-dGZNFs were also analyzed (Supplementary Figure 10 and 11); C-C bonding became more intense after the reduction process, and Ge-Zn-O bonding was also visible. The calibrated graph in Figure 3-2f based on energy-dispersive X-ray (EDX) spectroscopy and SEM images confirmed that the Ge content dramatically decreased during the reduction process owing to the sublimation of unstable Ge states. For this reason, 26 wt% of Ge was lost and 11% of diameter shrinkage occurred, as determined through the comparison of O-iGNFs and O-dGNFs. In contrast, the O-dGZNFs showed distinct characteristics with only 8 wt% of Ge loss and a 4% of diameter change during reduction. The overall weight change (Supplementary Figure 12) also showed similar patterns between O-dGNFs and O-dGZNFs: the introduction of Zn resulted in a higher yield of Ge. The well-distributed Ge-Zn atoms with Ge-Zn-O bonds resulting from intermolecular interactions clearly bind near Ge-Ge bonds because Zn-O consumes minimal oxygen at this step due to insufficient activation energy for the reaction ($ZnO\,(s) + H_2\,(g) \rightarrow Zn\,(s) + H_2O\,(g)$). That is, sturdy Zn-O bonds directly connected to Ge-O can hold metallic Ge without vaporization. Such intermolecular interactions in O-dGZNFs enhance the electrical properties due to the uniform metallic zinc distribution, leading to high electronic conductivity and ultralong cycle stability as well as structural maintenance. In addition, the introduction of Zn into O-dGZNFs resulted in a higher surface area (61.3 $m^2\ g^{-1}$) than that (37.1 $m^2\ g^{-1}$) of O-dGNFs (Supplementary Figure 13), with higher concentrations of distinct mesopores (between 3 and 4 nm).

Revealing the electrochemical maturation of O-dGZNFs. Ge anodes feature intrinsically inferior electronic conductivity and undergo a large volume change during cycling in LIBs, triggering poor electrochemical performance despite exhibiting a high theoretical capacity. In contrast, Zn demonstrates a low volume expansion (Li_xZn, $0 < x < 1$) and outstanding electronic conductivity. Therefore, O-dGZNFs, a composite of Ge and Zn, displayed compatible advantages

with improved ion conductivity. Galvanostatic measurements of O-dGNF and O-dGZNF electrodes were conducted to determine the dependence of their electrochemical properties on the intermolecular bonding of Ge-Zn. The differential capacity results in Figure 3-3a and b show redox peaks during the discharge/charge of O-dGNFs and O-dGZNFs, respectively. In the 1st cycle, an SEI layer was formed, and the conversion reaction of Ge-O occurred at 0.87 V in the cathodic part. Thus, the peaks at approximately 0.18, 0.36, and 0.51 V are related to the Li-Ge alloy reaction. Furthermore, Li ions were extracted from the Li-Ge alloy at the anodic peaks (0.36 and 0.49 V), followed by the reformation of Ge-O bonds due to lithium oxide (Li_2O) decomposition at 1.08 V. The O-dGZNF electrode displayed a similar tendency, but some peaks were slightly shifted during the 1st cycle, which can be ascribed to the introduction of foreign Zn atom. After the 1st cycle, the cathodic and anodic peaks of both electrodes remained consistent. Figure 3-3c exhibits the first galvanostatic discharge/charge capacities of O-dGNFs (1965/1360 mAh g^{-1}) and O-dGZNFs (1444/1043 mAh g^{-1}), which show a low initial Coulombic efficiency (ICE) of 69.2 and 72.2%, respectively, because one-dimensional materials feature a large surface area, which means that more Li ions participate in the formation of SEI layers. The introduction of Zn resulted in a slightly enhanced ICE, although the difference was not significant. Surprisingly, the galvanostatic discharge/charge profile of the 50th cycle did not show a plateau related to conversion and Li_2O decomposition compared with that of the 1st cycle. Moreover, the Li_2O decomposition at 1.08 V (O-dGNFs) and 1.04 V (O-dGZNFs) decreased and vanished after cycles (Figure 3-3a, b). This trend suggests that the oxygen components in the NFs were transformed into different forms during the initial cycles. Core-level XPS spectra of 50-cycled electrodes (O-dGNFs-50th and O-dGZNFs-50th) were characterized after the removal of partial SEI layers by slight etching. As shown in Supplementary Figure 14a-c, most of the oxygen components in the NFs were reformed into Li_2O and lithium carbonate (Li_2CO_3) composites, as well as components of SEI layers[40-42]. Additionally, the presence of LiF in nanofibers is attributed to the decomposition of $LiPF_6$ and reduction of fluoroethylene carbonate (FEC) due to the lower unoccupied molecular orbital (LUMO) level of LiF, which is in accordance with previous works (Supplementary Figure 14c, d)[43-46]. Furthermore, Ge-Zn-O and Ge metallic bonds remained after the 50th cycle. The capacity retention (Q) with cycling in Figure 3-3d reflects oxygen deformation and irreversible Li_2O decomposition during the initial 50 cycles as the capacity gradually decreased.

The above phenomenon influences the electrochemical properties of NFs. After the 50th cycle, the O-dGZNFs displayed outstanding reversible capacity and cycle retention until the 350th cycles, even at 2.0 C-rate, with almost 100% capacity retention (0.05% capacity decay per cycle). In addition, to examine the effect of oxygen content on the electrochemical performance of the O-

dGZNF electrode as well as to determine the optimized oxygen contents of the NFs, charge capacity retention tests (Supplementary Figure 15) were carried out for O-dGZNFs with different Ge/Zn ratios; a higher proportion of Zn led to a higher oxygen content, resulting in stable cycle retention owing to the high ionic/electronic conductivity but poor reversible capacity; a lower oxygen content resulted in a higher initial capacity, but capacity fading was more prominent. In contrast, the O-dGNFs required an activation step to attain optimal capacity, showing a capacity gain during tens of cycles. However, the O-dGNF electrode subsequently suffered from fatal capacity decay with only 49.5% retention (corresponding to 0.3% capacity decay per cycle) due to the low electronic conductivity and low response to current changes. To verify this behavior and confirm the main reasons, cyclic voltammetry (CV) measurements were conducted at various scan rates after the 1st cycle and 50th cycle. The results are shown in Supplementary Figure 16; the contributions of faradaic and capacitive (nonfaradaic) current were calculated using Equation (1) and are shown in Figure 3-3e:

$$i_p = k_1 v + k_2 v^{1/2} \quad \text{Equation (1)}$$

where i_p is the peak current and ν is the scan rate in the CV graph, and k_1 and k_2 are the constants for the capacitive and faradaic current, respectively. The capacitive current is related to surface reactions at the interface between the electrolyte and electrode, while the faradaic current is related to the charge transfer redox reaction at the electrode. In other words, the total current in CV measurements consists of faradaic and capacitive currents. Figure 3-3e shows that the capacitive current was dominant for both electrodes at all scan rates from 0.4 to 1.0 mV s^{-1} due to the high surface area of the one-dimensional structure (capacitive current: 65.8% for O-dGNFs and 78.5% for O-dGZNFs). In particular, the O-dGZNF electrode, which has a higher BET surface area, showed a higher capacitive current than that of the O-dGNF electrode. However, the dominant current switched to the faradaic current after the 50th cycle for both electrodes; this change can be ascribed to the formation of lithium composites, such as Li_2O and Li_2CO_3, as well as metallic bonds (Ge-Ge or Ge-Zn). In particular, Zn has better intrinsic electronic conductivity than Ge, leading to a higher charge transfer rate and a greater faradaic current in O-dGZNFs. In addition, the lithium composites detected in the XPS results in Supplementary Figure 14a-c act as ion conductors that can enhance the ion diffusion rate in the electrode[44-46]. For evidence, we calculated the Li ion diffusion coefficient by linearly fitting the plots of the square root of the scan rate ($v^{1/2}$) with respect to the peak current (I_p) (Figure 3-3f) based on the Randles-Sevcik equation (Equation (2)):

$$i_p = 268,600 n^{3/2} A D^{1/2} C v^{1/2} \quad \text{Equation (2)}$$

where n is the number of transported electrons, A is the area of the electrodes in a coin-type cell, D is the diffusion coefficient of Li ions in the electrode, and C is the concentration of Li salt in

the electrolyte. The slope, which is related to the Li ion diffusion coefficient, increased after 50 cycles as the ion diffusivity increased (Figure 3-3f). The Li ion diffusion coefficients of cycled electrodes were 1.2-1.4 times higher than those of pristine electrodes. Such increased Li ion diffusion coefficients suggest better ionic conductivity arising from the formation of lithium composites (Li_2O and Li_2CO_3) during cycling. After the 1st, 10th, and 50th cycles, the Li ion diffusion coefficients gradually increased; this increase was proportional to the increased amount of lithium composites (Supplementary Figure 17 and Supplementary Table 1).

Regarding the relationship between metallic bonds and electronic conductivity, existing Ge-O-Ge or Ge-Zn-O bonds would be reduced to Ge-Ge or Ge-Zn when the oxygen atoms are combined with lithium and carbon during cycling. The XPS spectra in Figure 3-4a and b and Supplementary Figure 14e show the development of more Ge^0 bonds and peak shifts compared to those observed in the XPS results of O-dGNFs and O-dGZNFs in Figure 3-2b and c and Supplementary Figure 9. In particular, the Ge-Zn-O peak in O-dGZNFs was located at approximately 32 eV (Ge 3d) and 1021/1044 eV (Zn 2p), but all peaks of Ge-Zn-O were partially shifted, to 31.5, 1020.6, and 1043.4 eV, arising from oxygen defects within the bonds. The gradual emergence of metallic bonds in the NFs, corroborated by XPS analysis, can also account for the rising faradaic current because electronic conductivity is also improved with increased metallic bonds as well as increased Li ion diffusivity. Furthermore, FT-EXAFS analysis proved the maintenance of intermolecular bonding and oxygen removal in O-dGNFs-50th and O-dGZNFs-50th in various charge/discharge states compared with the corresponding pristine states before cycling (Figure 3-4c, d). In accordance with the trends mentioned above, the intensity of Ge-O significantly decreased for both O-dGNFs-50th and O-dGZNFs-50th. The peak of O-dGNFs-50th coincides with the reference Ge peak (2.14 Å), whereas O-dGZNFs-50th still exhibits a peak at 2.17 Å; these results demonstrate the reversible characteristics of Ge-Zn bonds during cycling. When the samples were discharged, the Ge-Ge peak was relocated to 2.19 and 2.20 Å, signifying the emergence of Li-Ge bonds from metallic Ge-Ge and Ge-Zn bonds; this result is also supported by X-ray absorption near-edge structure (XANES) profiles (Supplementary Figure 18)[39, 47]. To further compare the electrochemical/structural stability of O-dGZNFs with that of O-dGNFs, real-time characterization was conducted using *in situ* TEM and electrochemical impedance spectroscopy (EIS).

***In situ* observation of the structural and electrochemical behavior of O-dGZNFs.** To demonstrate the behavior of a single NF during cycling in real time, *in situ* TEM experiment was carried out with *I-V* curve analysis to examine the structural and phase evolution of an O-dGZNF as well as the electronic conductivity of a single NF during the electrochemical discharge/charge process.[48] The fine structure of the Ge-Zn distorted array can unpredictably affect the structural

stability and electrochemical properties throughout the whole process. For *in situ* TEM, all potentiostatic measurements were analyzed using a nanobattery that consisted of a single NF-based working electrode (sample) and counter electrode (Li metal) with naturally formed Li_2O as a solid-state electrolyte on the Li metal, as illustrated in Supplementary Figure 19. Time-resolved snapshots of the O-dGZNF were taken at 0, 900, 982, 1144, and 1897 s, showing the morphological evolution of the material from the discharged state to the charged state (Figure 3-5a-e). Before lithiation, the O-dGZNF was 63 nm in diameter (Figure 3-5a, k) with no noticeable Ge diffraction patterns due to the distorted structure and amorphous rings (Figure 3-5f). When a negative bias of -2 V was applied to initiate lithiation (discharge process) on the O-dGZNF, Li_2O was initially formed due to the native oxide layer and oxygen atoms that came from Ge-Zn-O bonds (Figure 3-5b, g). Then, upon further lithiation, Ge and Zn atoms solely reacted with Li ions by breaking Li_xGe and LiZn bonds, as shown in Figure 3-5c and h[43]. Finally, crystalline $Li_{15}Ge_4$ was completely formed from amorphous Li_xGe and showed a diameter of 91 nm, indicating 44% expansion (Figure 3-5d, i, l, and Supplementary Movie 1)[49]. After 1144 s, delithiation (charge process) was launched by applying a positive bias of 2 V, and Li was extracted from the O-dGZNF, as shown in Supplementary Movie 2. Afterward, the diameter of the NF was reduced to 82 nm (31% expansion with respect to pristine NF), while considerable amounts of Li-Ge and Li-Zn alloys were converted back to a-Ge and Ge-Zn (Figure 3-5e, j, m); these results corresponded to the XPS results of cycled samples in Figure 3-4 and Supplementary Figure 14. The overall volume change of the NF during one cycle in real time was shown in Figure 3-5n. For comparison, *in situ* TEM was also conducted for the electrochemical discharge process of an O-dGNF under the same conditions. Although the phase transition (formation of Li_2O and alloyed Ge) was similar upon lithiation, the overall volume expansion after delithiation was larger (51% diameter change), even though the NF was thinner (Supplementary Figure 20 and Movie 3). Based on these results, Zn helped to alleviate volume expansion; this assistance can be ascribed to better structural integrity arising from the formation of Ge-Zn-O and a lower theoretical volume change in Zn.

To comprehend such trends at the bulk scale, *ex situ* SEM analysis was performed to further compare the degrees of volume change in O-dGZNFs and O-dGNFs. The cross-sectional SEM images in Supplementary Figure 21 showed a smaller thickness change in O-dGZNFs (11.6%) than in O-dGNFs (13.3%) after the 1st cycle. The intermolecular introduction of Zn atoms, which partially act as buffering layers, into the Ge-based NFs resulted in a lower degree of volume change. As a result, the O-dGNF electrode finally underwent a 211% volume expansion after 300 cycles due to the agglomeration of Ge particles and fracturing during cycling, whereas the O-dGZNF electrode only showed a 100% volume change. In addition, *ex situ* TEM analysis after 50 cycles (Supplementary Figure 22) corroborated the stable formation of an SEI layer on the O-

dGZNFs, in contrast to O-dGNFs; the introduction of Zn also resulted in more stable interfacial properties. The large volume expansion of O-dGNFs was attributed to the pulverization of the active materials, leading to unsustainable cycle retention (Figure 3-3d). In addition, the electronic characteristics of O-dGNF and O-dGZNF were verified through *in situ* conductivity measurements (Figure 3-5o) of each single NF. The conductivity was measured at three different states (state i, ii, and iii, corresponding to Figure 3-5f, g, and i, respectively) of lithiation in a voltage range from -10 to 10 V. When we simply calculated the electrical conductance using Ohm's law (R = V/I or G = I/V, where R, G, V, and I indicate the electrical resistance, conductance, voltage, and current, respectively), a small difference in conductance between the two single NFs was apparent in state i. In contrast, the electrical conductance of the O-dGZNF in state ii was 36 times higher than that of O-dGNF because metallic Ge-Zn bonds were formed due to Li_2O formation from Ge-Zn-O. Furthermore, the conductance of O-dGZNF in state iii was still 31 times higher than that of O-dGNF even after complete lithiation of both NFs – this result is attributed to the higher intrinsic conductivity of Zn (1.7×10^7 S m^{-1}) than that of Ge (2×10^3 S m^{-1}) in the bulk; furthermore, lithiated Ge exhibits enhanced electrical properties. This result clearly demonstrates that the intermolecular introduction of Zn leads to dramatically improved electrical conductance and can be expected to provide a facile electron pathway upon discharge/charge.

Additionally, *in situ* galvanostatic electrochemical impedance spectroscopy (GS-EIS) (Figure 3-5p) was performed at 1.0 C-rate during lithiation to obtain a comprehensive understanding of the effect of Zn on electrochemical performance because the electrochemical kinetics of electrodes are strongly related to the charge transfer resistance (R_{CT}). The overall R_{CT} value of the O-dGZNF electrode including intermolecular Zn was significantly less than that of the O-dGNF electrode owing to the enhanced electronic conductivity of O-dGZNFs. Moreover, the improved ionic conductivity resulting from the random distribution of Li_2O and Li_2CO_3 in NFs helps Li ions easily penetrate the active materials and maintain a low R_{CT} value. However, R_{CT} typically increases in the stage of deep lithiation due to the formation of Li_2O and Li_2CO_3, which interrupt the movement of electrons and act as an insulator despite supporting fast Li ion diffusion, shown in O-dGNF electrode. In contrast, the O-dGZNF electrode sustained a low value of R_{CT} regardless of the formation of Li_2O/Li_2CO_3, attributed to the intermolecular distribution of Zn, which has outstanding electronic conductivity. These results suggest that randomly formed lithium composites decrease the resistance with an elevated ion diffusion rate and that the intermolecular interactions of Zn in the electrode significantly provide a facile electron pathway while simultaneously suppressing a resistance increase.

Extensive electrochemical performance characterization and practical confirmation of O-dGZNFs. The unstable structure of Ge suffers from electrochemical volume expansion during

lithiation, which triggers undesired side reactions, such as delamination and pulverization of the electrode with the continuous consumption of electrolyte. The structural evolution of intermolecularly connected O-dGZNFs exhibited outstanding electrochemical performance under harsh conditions (high C-rates) and ultralong cycle retention at 3.0 C-rate. The morphological structure of O-dGNFs was broken down due to uncontrollable volume expansion with uneven interfacial properties (Supplementary Figure 22a), which led to poor rate capability (Figure 3-6a). Such unstable structures inhibit facile electron transport at high current rates, leading to rapid capacity fading at high C-rates. In contrast, the O-dGZNFs became porous and hollow over the course of 50 cycles while relatively uniform interfacial layers containing Li_2O and Li_2CO_3 were formed, and the structural integrity of the material was maintained (Supplementary Figure 22b). As a result, O-dGZNFs can provide fast electron/ionic transport at high current rates and retain considerable capacity (~50% at 20 C compared with that at 0.2 C-rate). Furthermore, the O-dGZNFs showed a capacity recovery of 98.7% when the C-rate changed from 20 C to 0.2 C-rate. As O-dGZNFs possess suitable electrode architectures that allow facile ionic/electronic transport with considerable structural stability, this material also exhibits ultralong cyclability (capacity retention of 73%) at high C-rates (3.0 C-rate) without any dramatic capacity decay from electrode delamination or pulverization (Figure 3-6b).

Due to their practical feasibility, both O-dGNFs and O-dGZNFs were finally paired with a $LiCoO_2$ (LCO) cathode, which exhibited an electrode thickness of approximately 52.2 μm and typical electrochemical characteristics (Supplementary Figure 23). Because one-dimensional materials generally form a considerable proportion of the SEI layer due to their high surface area, the anodes were treated through a prelithiation process before full cell assembly. The full cells of O-dGNFs and O-dGZNFs initially exhibited reversible capacities of 2.11 and 2.02 mAh cm^{-2} after the formation cycle (Supplementary Figure 24a). Discharge capacity of both electrodes is higher than initial charge capacity owing to prelithiated anodes. Further cycle retention tests at 1.0 C-rate (Figure 3-6c) confirmed the significantly superior performance of O-dGZNFs when assembled in a full cell, delivering a reversible areal capacity of 0.95 mAh cm^{-2} with a capacity retention of 60% for 400 cycles, in contrast to O-dGNFs (capacity retention of only 23% with an areal capacity of < 0.5 mAh cm^{-2}). The demonstration of LED light is further showcased for O-dGZNFs in Supplementary Movie 4, which highlights the practical operation of such full cells. Moreover, the rate capabilities of O-dGZNFs and O-dGNFs assembled in full cells were further characterized and are shown in Supplementary Figure 24b; superior rate capabilities were also observed for O-dGZNFs in assembled full cells.

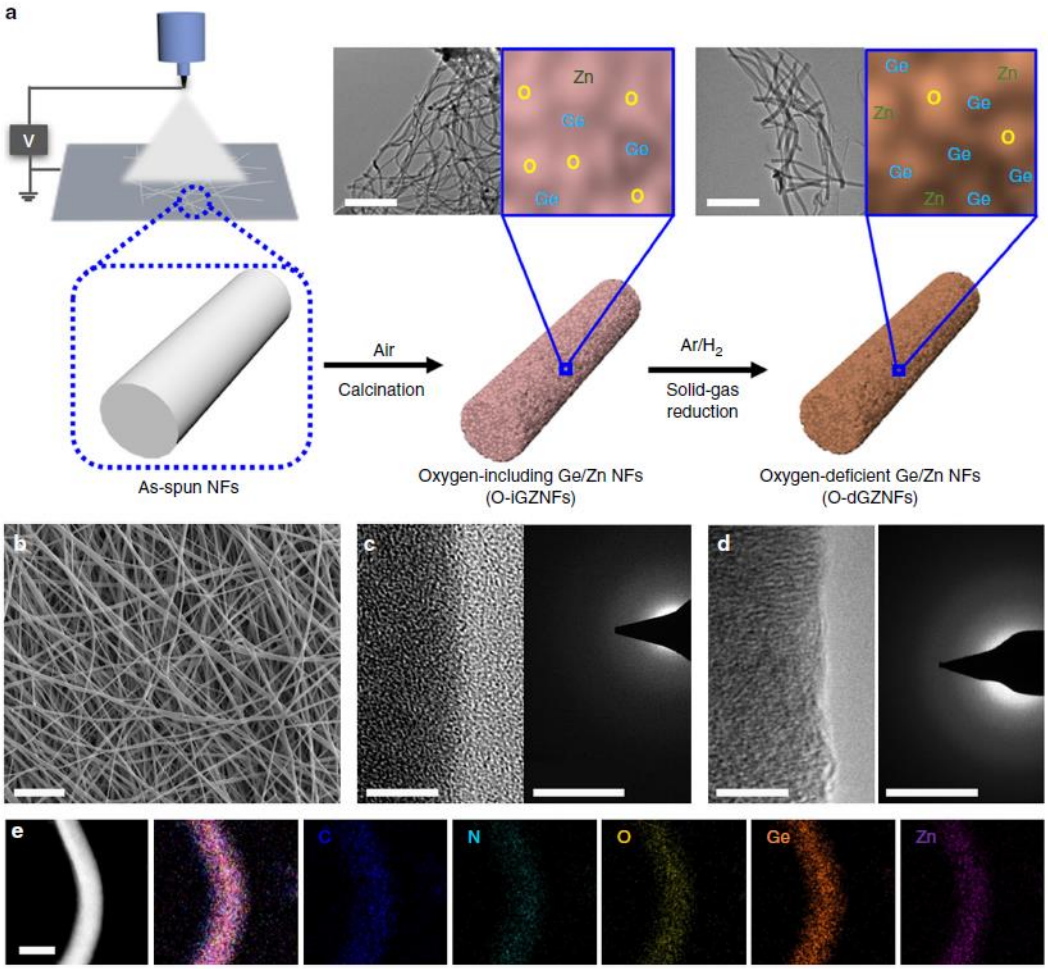

Figure 3-1. Morphological structure evolution. (a) Schematic illustration of the whole synthetic process. The inset TEM images in a correspond to O-iGZNFs and O-dGZNFs. (b) SEM image of as-spun NFs. HR-TEM images and SAED patterns of (c) O-iGZNFs and (d) O-dGZNFs. (e) HAADF-STEM mapping of O-dGZNFs: red-carbon, orange-nitrogen, yellow-oxygen, cyan-germanium, and green-zinc. Scale bars: (a) 500 nm, (b) 10 μm, (c, d) 5 nm and 5 1/nm, and (e) 50 nm.

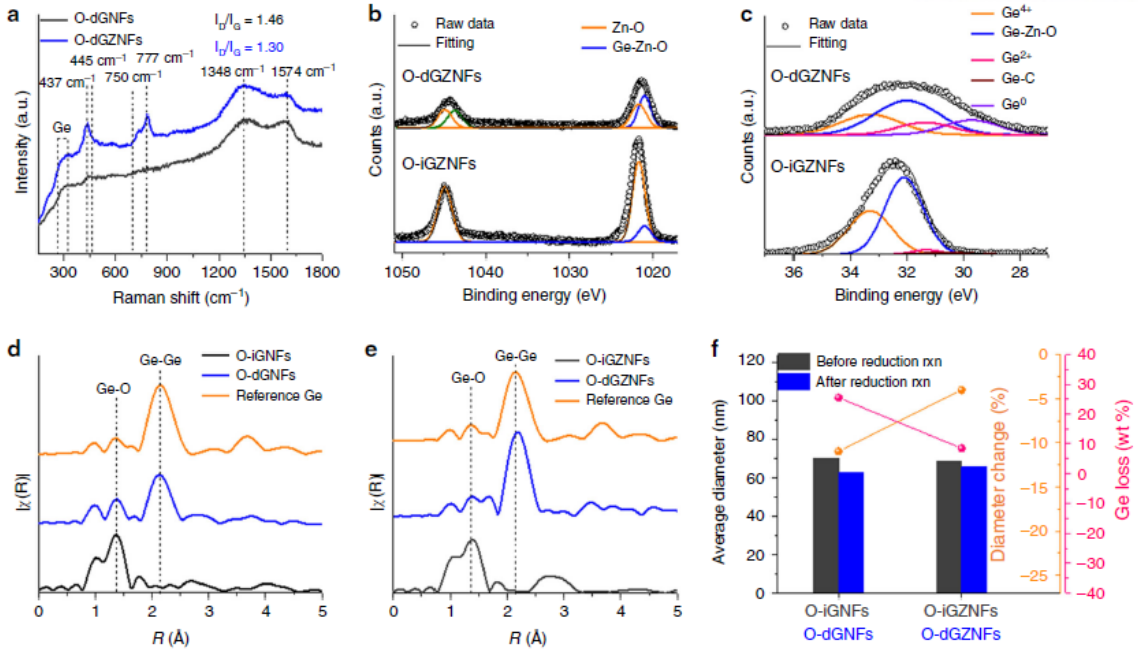

Figure 3-2. Structural analysis of the synthesis. (a) Raman spectra of O-dGNFs and O-dGZNFs. Core-level XPS spectra of O-iGZNFs and O-dGZNFs in (b) Zn 2p and (c) Ge 3d. EXAFS spectra of the (d) O-dGNF and (e) O-dGZNF series. Pure Ge was used as a reference sample. (f) Diameter change and Ge loss in O-dGNFs and O-dGZNFs.

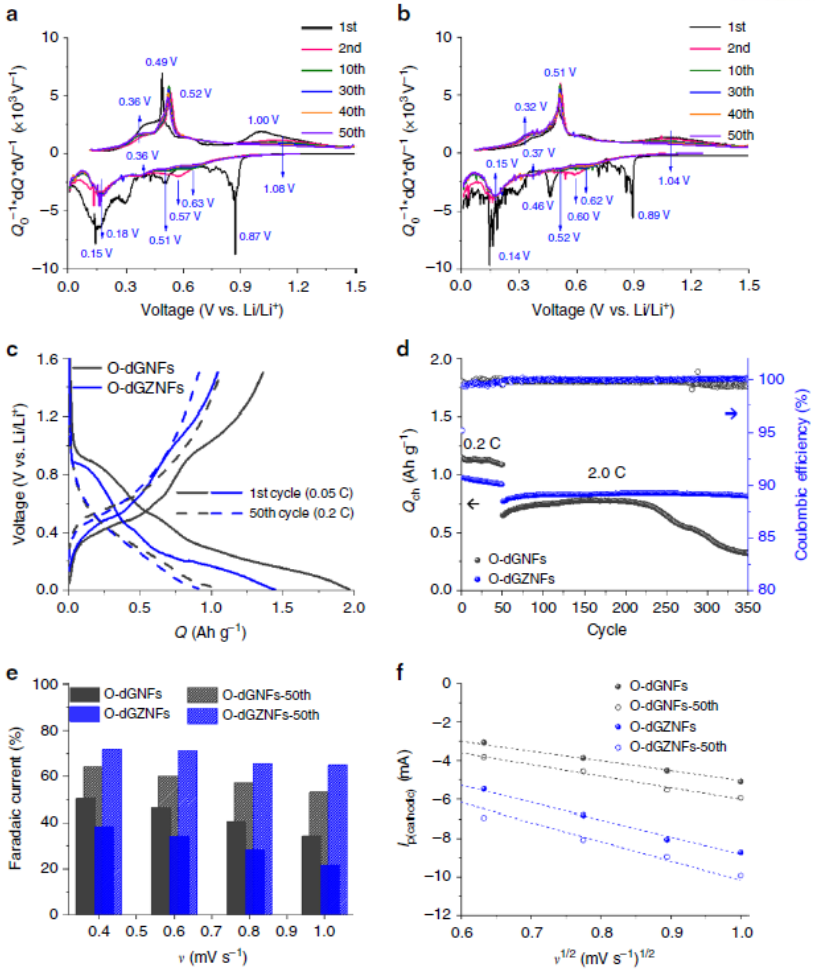

Figure 3-3. Electrochemical properties of O-dGNF and O-dGZNF electrodes. Differential capacities of (a) O-dGNFs and (b) O-dGZNFs for featured cycles. (c) Discharge/charge profiles at the 1st cycle (bold line) and 50th cycle (dashed line). (d) Charging capacity retention at 0.2 and 2.0 C-rate. (e) Comparison of the faradaic current of pristine and 50-cycled electrodes at various scan rates. (f) Plots of squared scan rate vs. peak current calculated by the Randles–Sevcik equation (Eq. (2)).

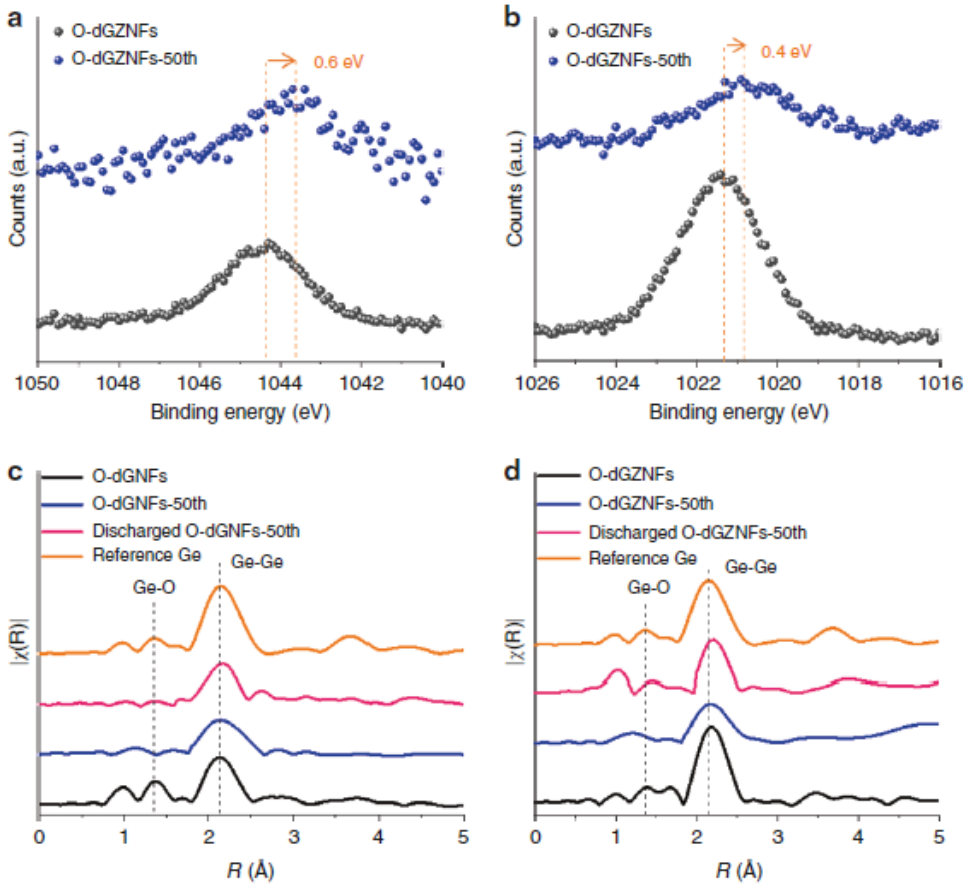

Figure 3-4. Physical analysis of O-dGNFs and O-dGZNFs at various states. (a, b) Core-level XPS spectra of pristine and O-dGZNFs-50th electrodes after partial etching to remove the SEI layer in Zn 2p. EXAFS spectra of (c) O-dGNFs and (d) O-dGZNFs at various states.

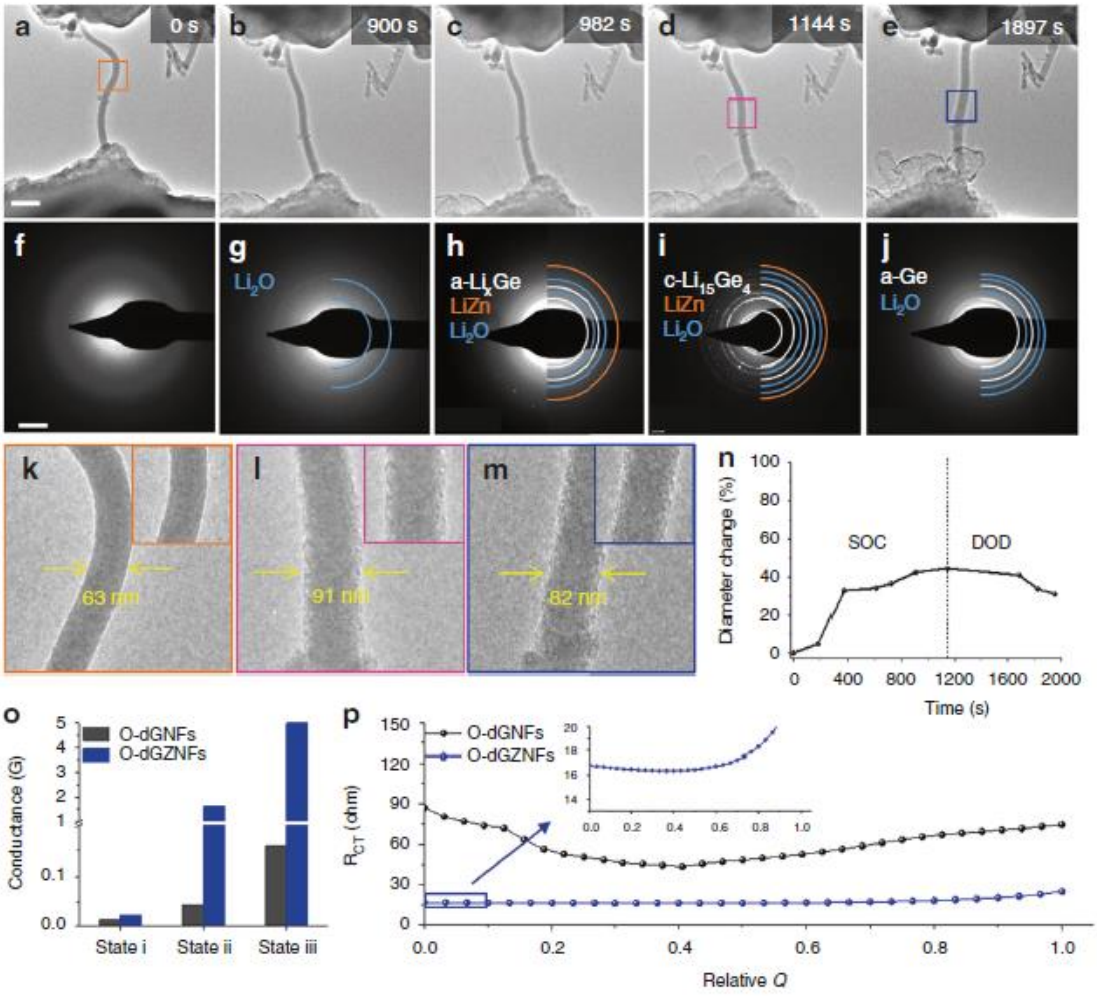

Figure 3-5. *In situ* characterization of O-dGNFs and O-dGZNFs. *In situ* TEM observations were conducted with an O-dGZNF sample. Time-resolved TEM images for (a–d) lithium insertion and e lithium extraction in real time. (f–j) Each SAED pattern corresponds to the TEM image above. (k–m) Magnified TEM images of featured states. (n) Curve of diameter change vs. time upon lithiation/delithiation. (o) *In situ* electrical conductivity measurement of O-dGNFs and O-dGZNFs during the lithiation process at three points, marked as state i, ii, and iii and corresponding to f, g, and i, respectively. (p) *In situ* EIS galvanostatic measurements during lithiation at 1.0 C-rate of O-dGNFs and O-dGZNFs. Scale bars: (a) 200 nm and (f) 5 1/nm.

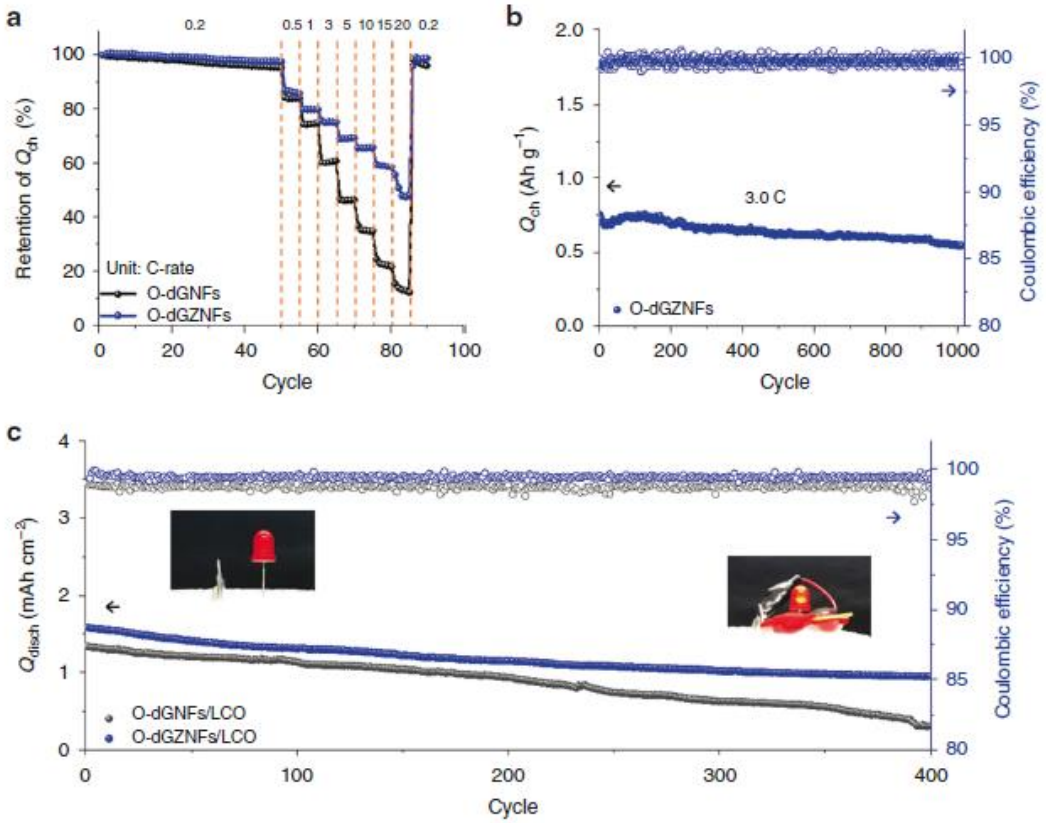

Figure 3-6. Rate capability and long-term cyclic stability in both half and full cells. (a) Rate capability of O-dGNFs and O-dGZNFs. (b) Cyclic performance of OdGZNFs at 3.0 C-rate. (c) Electrochemical performance of full cells assembled with LCO at 1.0 C-rate. Inset photographs indicate the charged O-dGZNFs/LCO full cell before and after closing the circuit.

3.4 Conclusion

Ge and Zn atoms are homogeneously distributed in our onedimensional, oxygen-deficient, disordered Ge–Zn NFs (OdGZNFs). The delicate formation of Ge–Zn bonds suppressed Ge sublimation during the synthetic process, which resulted in a higher yield of Ge after the reduction process. The intermolecular interactions of Ge–Zn in NFs not only contributed to enhanced structural integrity but also enabled faster electron and ionic transport, as evidenced by the higher electronic conductivity and Li ion diffusivity of O-dGZNFs compared with those of O-dGNFs. In addition to the superior architectures of O-dGZNFs compared with those of O-dGNFs, more uniform interfacial layers were formed on the OdGZNFs, which additionally act as fast ionic conductors. As the dual functionalities of Zn not only improve electronic conductivity but also maintain structural integrity, the O-dGZNFs exhibited outstanding rate capability (~50% capacity retention between 0.2 and 20 C-rate) and cycle retention (73% at 3.0 C-rate) with 546 mAh g−1 even after 1000 cycles. Furthermore, stable full cell operation of O-dGZNFs was demonstrated with LCO as a cathode for 400 cycles at a relatively high C-rate (1.0 C-rate). This work sheds light on the utilization of intermolecular interactions of metal atoms (Ge and Zn) to ensure facile ionic/electronic transport and stable interfaces/morphologies. This approach could be extended to other electrode materials to enable advanced rechargeable energy storage systems.

3.5 Reference

1. Son, I. H.; Park, J. H.; Park, K.; Han, S.; Shin, J.; Doo, S.-G.; Hwang, Y.; Jang, H.; Choi, J. W. Graphene balls for lithium rechargeable batteries with fast charging and high volumetric energy densities. *Nat. Commun.* **2017**, *8*, 1561.

2. Nitta, N.; Wu, F. X.; Lee, J. T.; Yushin, G. Li-ion battery materials: present and future. *Mater. Today* **2015**, *18*, 252–264.

3. Lu, J.; Wu, T. P.; Amine, K. State-of-the-art characterization techniques for advanced lithium-ion batteries. *Nat. Energy* **2017**, *2*, 17011.

4. Arico, A. S.; Bruce, P.; Scrosati, B.; Tarascon, J. M.; Van Schalkwijk, W. Nanostructured materials for advanced energy conversion and storage devices. *Nat. Mater.* **2005**, *4*, 366–377.

5. An, Y.; Fei, H.; Zeng, G.; Ci, L.; Xi, B.; Xiong, S.; Feng, J. Commercial expanded graphite as a low-cost, long-cycling life anode for potassium-ion batteries with conventional carbonate electrolyte. *J. Power Sources* **2018**, *378*, 66–72.

6. An, Y.; Zhang, Z.; Fei, H.; Xu, X.; Xiong, S.; Feng, J.; Ci, L. Lithium metal protection enabled by in-situ olefin polymerization for high-performance secondary lithium sulfur batteries. *J. Power Sources* **2017**, *363*, 193–198.

7. An, Y.; Fei, H.; Zeng, G.; Xu, X.; Ci, L.; Xi, B.; Xiong, S.; Feng, J.; Qian, Y. Vacuum distillation derived 3D porous current collector for stable lithium-metal batteries. *Nano Energy* **2018**, *47*, 503–511.

8. An, Y.; Fei, H.; Zeng, G.; Ci, L.; Xiong, S.; Feng, J.; Qian, Y. Green, scalable, and controllable fabrication of nanoporous silicon from commercial alloy precursors for high-energy lithium-ion batteries. *ACS Nano* **2018**, *12*, 4993–5002.

9. An, Y.; Zhang, Z.; Fei, H.; Xiong, S.; Ji, B.; Feng, J. Ultrafine TiO_2 confined in porous-nitrogen-doped carbon from metal-organic frameworks for high-performance lithium sulfur batteries. *ACS Appl. Mater. Interfaces* **2017**, *9*, 12400–12407.

10. An, Y.; Fei, H.; Zhang, Z.; Ci, L.; Xiong, S.; Feng, J. A titatnium-based metal-organic framework as an ultralong cycle life anode for PIBs. *Chem. Commun.* **2017**, *53*, 8360.

11. Choi, S.; Kim, J.; Choi, N.-S.; Kim, M. G.; Park, S. Cost-effective scalable synthesis of mesoporous germanium particles via a redox-transmetalation reaction for high-performance energy storage devices. *ACS Nano* **2015**, *9*, 2203–2212.

12. Park, M.-H.; Cho, Y.; Kim, K.; Kim, J.; Liu, M.; Cho, J. Germanium nanotubes prepared by using the kirkendall effect as anodes for high-rate lithium batteries. *Angew. Chem. Int. Ed.* **2011**, *50*, 9647–9650.

13. Li, W.; Li, M.; Yang, Z.; Xu, J.; Zhong, X.; Wang, J.; Zeng, L.; Liu, X.; Jiang, Y.; Wei, X.; Gu, Li.; Yu, Y. Carbon-coated germanium nanowires on carbon nanofibers as self-supported electrodes for flexible lithium-ion batteries. *Small* **2015**, *11*, 2762–2767.

14. Mo, R. W.; Rooney, D.; Sun, K. N.; Yang, H. Y. 3D nitrogen-doped graphene foam with encapsulated germanium/nitrogen-doped graphene yolk-shell nanoarchitecture for high-performance flexible Li-ion battery. *Nat. Commun.* **2017**, *8*, 13949.

15. Hwang, J.; Jo, C.; Kim, M. G.; Chun, J.; Lim, E.; Kim, S.; Jeong, S.; Kim, Y.; Lee, J. Mesoporous Ge/GeO_2/carbon lithium-ion battery anodes with high capacity and high reversibility. *ACS Nano* **2015**, *9*, 5299–5309.

16. Yoon, S.; Jung, S.-H.; Jung, K.-N.; Woo, S.-G.; Cho, W.; Jo, Y.-N.; Cho, K. Y. Preparation of nanostructured Ge/GeO_2 composite in carbon matrix as an anode material for lithium-ion batteries. *Electrochim. Acta* **2016**, *188*, 120–125.

17. Wang, X.-L.; Han, W.-Q.; Chen, H.; Bai, J.; Tyson, T. A.; Yu, X.-Q.; Wang, X.-J.; Wang, X.-Q. Amorphous hierarchical porous GeO_x as high-capacity anodes for Li ion batteries with very long cycling life. *J. Am. Chem. Soc.* **2011**, *133*, 20692–20695.

18. Seng, K. H.; Park, M.-H.; Guo, Z. P.; Liu, H. K.; Cho, J. Catalytic role of Ge in highly reversible GeO_2/Ge/C nanocomposite anode material for lithium batteries. *Nano Lett.* **2013**, *13*, 1230–1236.

19. Liu, J.; Song, K.; Zhu, C.; Chen, C.-C.; van Aken, P. A.; Maier, J.; Yu, Y. Ge/C nanowires as high-capacity and long-life anode materials for Li-ion batteries. *ACS Nano* **2014**, *8*, 7051–7059.

20. Li, D.; Wang, H. Q.; Liu, H. K.; Guo, Z. P. A new strategy for achieving a high performance anode for lithium ion batteries-encapsulating germanium nanoparticles in carbon nanoboxes. *Adv. Energy Mater.* **2016**, *6*, 1501666.

21. Liu, X.; Hao, J.; Liu, X.; Chi, C.; Li, N.; Endres, F.; Zhang, Y.; Li, Y.; Zhao, J. Preparation of Ge nanotube arrays from an ionic liquid for lithium ion battery anodes with improved cycling stability. *Chem. Commun.* **2015**, *51*, 2064–2067.

22. Xiao, W.; Zhou, J.; Yu, L.; Wang, D. H.; Lou, X. W. Electrolytic formation of crystalline silicon/germanium alloy nanotubes and hollow particles with enhanced lithium-storage properties. *Angew. Chem. Int. Ed.* **2016**, *55*, 7427–7431.

23. He, W.; Tian, H. J.; Wang, X. L.; Xin, F. X.; Han, W. Q. Three-dimensional interconnected network GeO_x/multi-walled CNT composite spheres as high performance anodes for lithium ion batteries. *J. Mater. Chem. A* **2015**, *3*, 19393–19401.

24. Hsieh, M. H.; Li, G. A.; Chang, W. C.; Tuan, H. Y. A. Germanium nanoparticles/molybdenum disulphide (MoS_2) nanocomposite as a high capacity, high-rate anode material for lithium-ion batteries. *J. Mater. Chem. A* **2017**, *5*, 4114–4121.

25. Ryu, J.; Hong, D.; Shin, S.; Choi, W.; Kim, A.; Park, S. Hybridizing germanium anodes with polysaccharide-derived nitrogen-doped carbon for high volumetric capacity of Li-ion batteries. *J. Mater. Chem. A* **2017**, *5*, 15828–15837.

26. Wang, B.; Wen, Z.; Jin, J.; Hong, X.; Zhang, S.; Rui, K. A novel strategy to prepare Ge@C/rGO hybrids as high-rate anode materials for lithium ion batteries. *J. Power Sources* **2017**, *342*, 521–528.

27. Kim, T.-H.; Park, S. Y.; Lee, T. H.; Jeong, J.; Kim, D. H.; Swihart, M. T.; Song, H.-K.; Kim, J. Y.; Kim, S. ZnO decorated germanium nanoparticles as anode materials in Li-ion batteries. *Nanotechnology* **2017**, *28*, 095402.

28. Xie, Y.; Wu, F.; Sun, X.; Chen, H.; Lv, M.; Ni, S.; Liu, G.; Xu, X. Quinary wurtzite Zn–Ga–Ge–N–O solid solutions and their photocatalytic properties under visible light irradiation. *Sci. Rep.* **2016**, *6*, 19060.

29. Sun, Y.; Yang, G. Z.; Cui, H.; Wang, J.; Wang, C. X. $Zn_xGe_{1-x}O$ 3D micronano structures with excellent performance as anode material in lithium ion battery. *ACS Appl. Mater. Interfaces* **2015**, *7*, 15230–15239.

30. Lee, Y.-W.; Kim, D.-M.; Kim, S.-J.; Kim, M. C.; Choe, H.-S.; Lee, K.-H.; Sohn, J. I.; Cha, S. N.; Kim, J. M.; Park, K.-W. In situ synthesis and characterization of Ge embedded electrospun carbon nanostructures as high performance anode material for lithium-ion batteries. *ACS Appl. Mater. Interfaces* **2016**, *8*, 7022–7029.

31. Hidalgo, P.; Lopez, A.; Mendez, B.; Piqueras, J. Synthesis and optical properties of Zn_2GeO_4 microrods. *Acta Mater.* **2016**, *104*, 84–90.

32. Wu, S. P.; Wang, Z. L.; Ouyang, X.; Lin, Z. Q. Core–shell Zn_2GeO_4 nanorods and their size-dependent photoluminescence properties. *Nanoscale* **2016**, *8*, 6884.

33. Wang, M. S.; Jiang, L. X.; Kim, E. J.; Hahn, S. H. Electronic structure and optical properties of $Zn(OH)_2$: LDA+U calculations and intense yellow luminescence. *RSC Adv.* **2015**, *5*, 87496–87503.

34. Qian, L.; Chen, J. F.; Li, Y. H.; Wu, L.; Wang, H. F.; Chen. A. P.; Hu, P.; Zheng, L. R.; Yang, H. G. Orange zinc germanate with metallic Ge–Ge bonds as a chromophore-like center for visible-light-driven water splitting. *Angew. Chem. Int. Ed.* **2015**, *54*, 11467–11471.

35. Kumar, D. R.; Manoj, D.; Santhanalakshmi, J. Au–ZnO bullet-like heterodimer nanoparticles: synthesis and use for enhanced nonenzymatic electrochemical determination of glucose. *RSC Adv.* **2014**, *4*, 8943–8952.

36. Echeverria, J.; Falceto, A.; Alvarez, S. Zinc–zinc double bonds: a theoretical study. *Angew. Chem. Int. Ed.* **2017**, *56*, 10151–10155.

37. Zhao, J.; Yang, L. J.; McLeod, J. A.; Liu, L. J. Reduced GeO_2 nanoparticles: electronic

structure of a nominal GeO_x complex and its stability under H_2 annealing. *Sci. Rep.* **2015**, *5*, 17779.

38. Yang, J.; Muhammad, S.; Jo, M. R.; Kim, H.; Song, K.; Agyeman, D. A.; Kim, Y.-I.; Yoon, W.-S.; Kang, Y.-M. In situ analyses for ion storage materials. *Chem. Soc. Rev.* **2016**, *45*, 5717–5770.

39. Agarkova, G. A.; Sadykov, R. M. Kinetics of low-temperature reduction of germanium dioxide by hydrogen. *J. Appl. Chem.* **1971**, *44*, 1629.

40. Lee, J.-I.; Ko, Y.; Shin, M.; Song, H.-K.; Choi, N.-S.; Kim, M. G.; Park, S. High-performance silicon-based multicomponent battery anodes produced via synergistic coupling of multifunctional coating layers. *Energy Environ. Sci.* **2015**, *8*, 2075–2084.

41. Gao, J., Gong, B.; Zhang, Q.; Wang, G.; Dai, Y.; Fan, W. Study of the surface reaction mechanism of $Li_4Ti_5O_{12}$ anode for lithium-ion cells. *Ionics* **2015**, *21*, 2409–2416.

42. Lee, J.; Choi, W. Surface modification of over-lithiated layered oxides with PEDOT:PSS conducting polymer in lithium-ion batteries. *J. Electrochem. Soc.* **2015**, *162*, A743–A748.

43. Cheong, J. Y.; Chang, J. H.; Seo, H. K.; Yuk, J. M.; Shin, J. W.; Lee, J. Y.; Kim, I.-D. Growth dynamics of solid electrolyte interphase layer on SnO_2 nanotubes realized by graphene liquid cell electron microscopy. *Nano Energy* **2016**, *25*, 154–160.

44. Strange, J. H.; Rageb, S. M.; Chadwick, A. V.; Flack, K. W.; Harding, J. H. Conductivity and NMR-study of ionic mobility in lithium-oxide. *J. Chem. Soc. Faraday Trans.* **1990**, *86*, 1239–1241.

45. Chadwick, A. V.; Flack, K. W.; Strange, J. H.; Harding, J. Defect structures and ionic transport in lithium-oxide. *Solid State Ion.* **1988**, *28*, 185–188.

46. Mizusaki, J.; Tagawa, H.; Saito, K.; Uchida, K.; Tezuka, M. Lithiumcarbonate as a solid electrolyte. *Solid State Ion.* **1992**, *53*, 791–797.

47. Lim, L. Y.; Liu, N.; Cui, Y.; Toney, M. F. Understanding phase transformation in crystalline Ge anodes for Li-ion batteries. *Chem. Mater.* **2014**, *26*, 3739–3746.

48. Yuan., Y.; Amine, K.; Lu, J.; Shahbazian-Yassar., R. Understanding materials challenges for rechargeable ion batteries with in situ transmission electron microscopy. *Nat. Commun.* **2017**, *8*, 15806.

49. Liu, X. H.; Huang, S.; Picraux, S. T.; Li, J.; Zhu, T.; Huang, J. Y. Reversible nanopore formation in Ge nanowires during lithiation-delithiation cycling: an in situ transmission electron microscopy study. *Nano Lett.* **2011**, *11*, 3991–3997.

***** *Chapter III is reproduced in part with permission of "Gyujin Song,† Jun Young Cheong,† Chanhoon Kim, Langli Luo, Chihyun Hwang, Sungho Choi, Jaegeon Ryu, Sungho Kim, Woo-Jin Song, Hyun-Kon Song, Chongmin Wang,* Il-Doo Kim,* Soojin Park*, Atomic-scale combination*

of germanium-zinc nanofibers for structural and electrochemical evolution, Nature Communications, 2019, 10, 2364". Copyright 2019 Springer Nature.

Chapter IV. Stress-tolerant nanoporous germanium nanofibers for long cycle life lithium storage with high structural stability

4.1 Introduction

One-dimensional (1D) nanosized electrode materials (nanowires, nanofibers, nanotubes, *etc.*) have highly contributed to improve performance of lithium-ion batteries (LIBs).[1-12] For example, high-capacity Si and Ge nanowire (NW) anodes which were firstly reported by Cui's group showed stable cycling lives with reversible capacities higher than 3500 (for Si NWs) and 1100 mAh g^{-1} (for Ge NWs) due to their large surface area which enables a facile access of electrolytes for rapid lithium-ion diffusion and effective accommodation of a large strain without pulverization during charge/discharge processes.[13,14] The small diameter of high-capacity NWs allows for effective accommodation of their huge volume changes (above 300%) during cycling without initiation of fracture which are commonly observed in bulk or micrometer-sized high-capacity anodes.[15,16] These NWs are usually prepared onto stainless steel current collectors by a vapor–liquid–solid method using a chemical vapor deposition (CVD) which is the most conventional method for growing 1D electrode materials.[13,14] However, the current CVD technology with lack of high throughput and low cost has restricted its availability and only contributed to synthesis of research-level NW anodes for LIBs.[17] Furthermore, highly flammable and volatile precursors for growing the NWs are usually toxic and morphological control such as introduction of porous structure is also limited.[18,19] Meanwhile, a large irreversible capacity loss in the first cycle, which is primarily attributed to the inherently large interfacial contact area between the NWs and electrolyte, also hampers practical utility of them.[14] In order to circumvent this intrinsic problem of the NW anodes, introduction of nanostructure in micrometer scale with moderate porosity can be an effective strategy not only for avoiding the severe side reaction with electrolyte but also for accommodation of huge volume expansion during lithiation.[20,21] For example, nanoporous 1D structure with micrometer length can provide both advantages of nano- and micrometer-sized high-capacity anodes including a facile Li-ion diffusion owing to short ion diffusion length and low reactivity in electrolyte.[1,2] Further, the empty spaces in nanoporous 1D structures also effectively accommodate the huge volume changes associated with repeated charge/discharge process.[1] Considering these features, utilizing the nanoporous 1D structure in high-capacity anodes is very appealing strategy. However, easy and high-throughput preparation method for the nanoporous 1D structure has not been reported.

Here, we report nanoporous Ge nanofibers (NPGeNFs) whose typical length is several tens

of micrometer and diameter is less than 200 nm *via* a combination of simple electrospinning and low energetic zincothermic reduction reaction. In contrast with the conventional CVD method, our method provides high tunability and controllability in terms of macro/microscopic morphologies such as porosity, length, and diameter for enhancing the electrochemical performance of electrodes. In this regard, we introduced the nanoporosity in the GeNFs (NPGeNFs) which facilitate the electrolyte penetration and shorten the transport distance of Li ions, resulting in favorable charge transfer at electrode/electrolyte interfaces, rather than leading to severe side reaction, which commonly occurs in NW anodes. Furthermore, the nanopores formed in the NPGeNFs effectively accommodate volume expansion upon lithiation and guarantee the reversibility of structural changes during cycles. With this rational design, the NPGeNFs delivered a high initial reversible capacity of 1373 mAh g^{-1} and outstanding capacity retention (80%) after 500 cycles at 3.0 C with extremely low capacity decay rate of 0.039% per cycle. Notably, stable capacity retention with considerable Coulombic efficiency in the full cell configuration with commercial $LiCoO_2$ indicated a high feasibility of the NPGeNFs as high performance anodes for LIBs.

4.2 Experimental method

Synthesis of Nanofibers. The NFs were prepared via a combination of electrospinning and a zincothermic reduction reaction. For the preparation of NPGeNFs, 0.6 g of germanium(IV) ethoxide (Sigma-Aldrich) and 0.87 g of TEOS (Sigma-Aldrich) were added in an 8 mL solution consisting of the same volume of dimethylformamide (DMF, Sigma-Aldrich) and ethanol. For HNPGeNFs, 0.6 g of germanium(IV) ethoxide and 1.74 g of TEOS and for L- NPGeNF, 1.2 g of germanium(IV) ethoxide and 0.87 g of TEOS were added in each 8 mL of solution consisting of the same volume of DMF and deionized (DI) water. After addition of 0.02 mL
(0.04 mL for the H-NPGeNF) of acetic acid (Alfa Aesar) in each solution, the solutions were vigorously stirred at room temperature for 6 h. Then, 1 g of PVP (Mw = 1 300 000 g mol^{-1}) was added in each solution and further stirred at room temperature for 12 h. For electrospinning, each solution was loaded into a plastic syringe that
was fixed at 20 cm from a stainless foil wrapped on a cylinder collector with a diameter of 8 cm. During the electrospinning, a voltage of 15.8 kV was applied from a high-voltage dc power supply to the tip of a stainless steel needle (21 gauge) connected to the syringe. The flow rates were adjusted to 1.5 mL h^{-1}, and the rotating speed of the cylinder collector was 100 rpm. The electrospinning was conducted at a constant temperature of 20 °C and relative humidity of 30%. After the electrospinning process, as-spun fiber mats were scrapped off from the stainless steel foil using a razor blade and moved to an alumina crucible. Then, the as-spun fiber mat was calcined at 600 °C for 5 h in a muffle furnace (Vulcan 3-550, Ney) with a ramping rate of 1.5 °C min^{-1}. Then, the as-calcined fiber mat was uniformly mixed with Zn metal powder in the atomic ratio of GeO_2 portion to Zn for each sample, moved to a stainless steel reactor, and heated at 600 °C for 3 h in an alumina furnace under an argon (Ar) atmosphere (ramping rate: 3 °C min^{-1}), named zincothermic reduction reaction. Afterward, HCl and HF etching treatments were conducted to remove ZnO byproducts formed during GeO_2 reduction and SiO_2 remaining in NFs, respectively. The NFs after calcination, ZRR, HCl, and HF treatment were labeled as GeO_2/SiO_2, $Ge/SiO_2/ZnO$, Ge/SiO_2, and HPGeNF, respectively. For the preparation of GeNFs, 0.4 g of GeO_2 was dissolved in 50 mL of DI water. Then, 7.5 g of PVP was added into the solution and stirred at 500 rpm for 6 h. Then, the electrospinning solution was loaded into the syringe, where the electrospinning process took place. The electrospinning was conducted with the following conditions: flow rate of 0.5 mL h^{-1}, an applied voltage of 16.0 kV, and a distance of 15 cm between the tip of the syringe and the current collector using a 25 gauge needle. The same processing procedures were applied to GeO_2 NFs for the calcination and reduction process. In the

case of GeNFs, only HCl treatment was conducted because no SiO_2 was included. **Characterization**. To characterize the morphologies of NFs, a transmission electron microscope (TEM, Titan cubed G2 60- 300, FEI) with an operating voltage of 300 kV and field-emission scanning electron microscopy (FE-SEM, S-4800, Hitach) were used. For the conformation of atomic distribution, HAADF-STEM mapping was conducted using the same TEM instrument. To understand the decomposition behavior of PVP and formation of the SiO_2/GeO_2 composite NFs, TGA (TG 209 F3, Netzsch) was conducted. XRD patterns were acquired using a Bruker D8-Advance with a 3 kW Cu Kα wavelength in the range of 20° and 80° to investigate sample crystallinity. BET and Barrett−Joyner−Halenda (BJH) analysis, for confirming surface area and pore distribution, were conducted by an Auto Physisorption analyzer (ASAP2020 analysis).

In Situ **TEM Observation**. The open cell, which was composed of Li metal as the counter electrode and samples as the working electrode loaded on a tungsten (W) tip and aluminum (Al) wire, respectively, was fabricated to observe the lithiation/delithiation process in real time using a Nanofactory STM holder and tested by an environmental TEM (ETEM, Titan, FEI). Li metal was scratched out in an Ar-filled glovebox, and it was transferred to the ETEM. While exposed to air (< 2 s), a lithium oxide solid-state electrolyte on a Li metal surface was formed. The −2 V/2 V bias was applied through the potentiostat to conduct lithiation/delithiation observation. **Electrochemical Test**. All electrodes were casted on Cu foil and composed of three kinds of components, active material, conductive materials, and binder in the ratio of 70:15:15 (w/w/w). Super-P carbon black and poly(acrylic acid)/carboxymethyl cellulose (1:1 weight ratio) was selected as the conductive material and the binder, respectively (loading mass ∼1 mg cm^{-2}). Then, the electrodes were transferred to an Ar-filled glovebox for cell assembly using 2016 cointype cells (Welcos), paired with a Li metal counter/reference electrode. A polypropylene membrane (Celgard) as a separator and ethylene carbonate/diethyl carbonate (3:7 v/v) with 10 wt % fluoroethylene carbonate additive and 1.3 M $LiPF_6$ salt as an electrolyte were chosen. All galvanostatic measurements were tested using a WBCS-3000 battery cycler (Wanatech) in the potential window of 0.005−1.5 V (first cycle)/0.01−1.5 V (further cycle) for the half cell and 2.5−4.29 V for the full cell at a continuous 25 °C. For the full cell test, the electrode was combined with lithium cobalt oxide ($LiCoO_2$, LCO) consisting of LCO:Super-P:polyvinylidene fluoride binder (90:5:5 w/w/w) (loading mass: 13 mg cm^{-2}). EIS results were obtained in the frequency range of 10^{-2}–10^6 Hz.

4.3 Results and discussion

Preparation and Characterization of the NPGeNFs. As shown in Figure 4-1a, the NPGeNFs were simply achievd *via* a combination of electrospinning and zincothermic reduction reaction (ZRR). Electrospun poly(vinyl pyrrolidone) (PVP) NFs containing tetraethylorthosilicate (TEOS) and germanium (IV) ethoxide (TEOG) were converted into inorganic composite NFs during calcination at 600 °C in air atmosphere. The shrinkage of the electrospun polymer NFs was observed due to removal of polymer during the calcination (Figure 4-1b and S1). According to thermogravimetric analysis (TGA) under oxygen atmosphere, the PVP was almost completely burned away above 600 °C and inorganic NFs were obtained (Figure S2). As can be clearly seen in Figure 4-1c, Ge, Si, and O elements were homogeneously distributed in the composite NFs. Subsequently, *in situ* reduction of the composite NFs using Zn vapor was carried out in stainless steel reactor at 600 °C for 3 h under inert atmosphere. In general, the ZRR was known as lower energetic reaction than other metallothermic reduction (using Mg or Al).[22,23] Therefore, this method is suitable for fabrication of delicate nanostructures. The nanopores were observed on the NFs due to the oxygen deficiency and finally the NPGeNFs were obtained after removing residual ZnO using dilute HCl (Figure 4-1d, S3, and S4). After etching process of SiO_2 using the dilute HF solution, abundant nanopores (diameter: 1-50 nm) were finally formed in the NPGeNFs along with the lattice fringe with a *d* spacing of 0.31 nm that exactly corresponds to the (111) plane of Ge, as shown in the high-resolution TEM (HRTEM) image and Brunauer-Emmett-Teller (BET) analysis in Figure 4-1e,f, and Figure S5a.[24] The XRD patterns display the components of each step clearly in Figure 4-1g and Figure S5b. After calcination step, the obtained inorganic NFs were composed of GeO_2 (JCPDF#03-065-6772) and SiO_2 (JCPDF#99-000-0356). The final products, NPGeNFs, showed pure Ge peaks such as 27.3, 45.4, 53.8, 66.1, and 72.9° corresponding to (111), (220), (311), (400), and (331), respectively (JCPDF#03-065-0333).

The nanoporous structure of the NPGeNFs takes a significant advantage of effective contact between electrolyte and electrode surface and facilitates charge transfer across the electrode-electrolyte interface without accompanying disadvantages of highly porous structure such as large irreversible capacity in the first cycle. The nanoporous morphology of NPGeNFs can be easily tunable by controlling composition of electrospinning solution (Figure S6). Increasing TEOS content in the electrospinning solution resulted in higher nanoporous morphology in NPGeNFs (hereafter, H-NPGeNFs), while lower nanoporous morphology in NPGeNFs (hereafter, L-NPGeNFs) was obtained with decreased TEOS content, as shown in (Figure S7) because the nanoporosity of NPGeNFs is determined by the removal of SiO_2 and ZnO from Ge/SiO_2

nanofibers after the ZRR. Therefore, the content of SiO_2 in the Ge/SiO_2 nanofibers can greatly affect the porous morphology of NPGeNFs. With higher TEOS content in electrospun nanofibers, the higher amount of SiO_2 is generated in the GeO_2/SiO_2 nanofibers, resulting in larger amount of removal of SiO_2 after ZRR and subsequent etching processes. As a result, NPGeNFs with more nanoporous morphology is obtained. On the other hand, NPGeNFs with less nanoporous morphology are obtained from as-spun nanofibers with low content of TEOS because small amount of SiO_2 is developed and etched in the GeO_2/SiO_2 nanofibers. In order to compare the effectiveness of nanoporous structure of NPGeNFs, we also synthesized nonporous germanium NFs (hereafter, GeNFs). Crystalline GeNFs showed lower porous surface morphology having smooth surface compared to those of H-NPGeNFs, NPGeNFs, and L-NPGeNFs (Figure S8 and S9).

***In Situ* TEM Observation of Lithiation/Delithiation**. Morphological changes of the NPGeNFs were investigated by *in situ* TEM during lithiation and delithiation processes. An open cell consisted of the NPGeNFs loaded on platinum wire substrate as the working electrode and a Li probe as the counter electrode. Then, native Li_2O surface layer grown on Li surface served as a solid electrolyte, as schematically shown in Figure 4-2a. External bias of -2 V/2 V was applied between the working and the counter electrodes for lithiation/delithiation processes. A time series of lithiation/delithiation of the NPGeNFs was displayed in Figure 4-2b. The time-lapse TEM images of the NPGENFs demonstrate large volume expansion and morphology change during the lithiation/delithiation. Owing to the nanoporous 1D structure, the NPGeNFs showed highly suppressed diameter change less than 25% after fully lithiation (Figure 4-2c and Supporting Video 1). Interestingly, the suppressed volume expansion was almost maintained during the delithiation (Supporting Video 2). A typical selected area electron diffraction (SAED) pattern for pristine NPGeNFs showed structural changes, that is a crystalline-to-amorphous phase transformation, accompanying alloy phases such as Li_xGe during the lithium alloying and dealloying (Figure 4-2d). The expanded volume of the NPGeNFs after delithiation is related to the pore memory effect, which is an interesting phenomenon of Ge anodes during lithiation/delithiation processes.[25,26] As shown in Figure 4-2e,f, nanopores in the NPGeNFs disappeared after full lithiation. Surprisingly, however, the previous nanopores in the NPGeNFs reappeared at the same locations with similar sizes and shapes. In addition, new nanopores appeared after delithiation. This “pore memory effect” can be explained on the basis of work by Liu *et al.* where they investigated reversible nanopore formation in Ge nanowires by *in situ* TEM.[25] First, after the nanopores are created in the NPGeNFs, Li diffusion will take place preferentially along the free surface of internal pores because surface diffusion is much faster than bulk diffusion. Therefore, regions near the pore were first lithiated and delithiated in subsequent cycles. Then, the pores were greatly constricted during

lithiation, but never fully closed, so when delithiation started, the pores could recover their old tracks. Meanwhile, the NPGeNFs sustained their expanded volume due to the generation of new nanopores near previous nanopores after delithiation. This interesting feature is beneficial for the battery performance because the reversible porous structure effectively alleviates repeated volume change of the NPGeNFs rather than fracture. Furthermore, new nanopores, which were developed near the previous nanopores, can also contribute to alleviate volume expansion.

Electrochemical Properties. Electrochemical properties of the NPGeNFs were investigated using CR 2016 coin-type cells. First of all, cyclic voltammetry (CV) was initially investigated, as shown in Figure 4-3a. The CV measurement was performed at a scan rate of 0.1 mV s^{-1} between 0 and 3.0 V. During the first cathodic scan, one peak at around 0.1 V was clearly observed, which can be ascribed to the formation of Li_xGe alloys and a solid electrolyte interface layer (SEI). The oxidation peak at around 0.58 V is attributed to the dealloying reaction of Li_xGe. In the second cycle, both the cathodic and anodic peaks were shifted or newly developed because of amorphization of Ge in the first lithiation process. Generally, amorphous Ge showed more favorable lithium insertion/deinsertion kinetics than crystalline Ge, resulting in the narrowing potential hysteresis.[20] Therefore, more sharp anodic/cathodic peaks were developed in the second CV curve. From the 3rd CV curve, both anodic and cathodic curves were gradually overlapped, indicating high reversibility of NPGeNFs.[27] Figure 4-3b and Figure S10a show the first galvanostatic discharge/charge profiles of GeNFs, H-NPGeNFs, NPGeNFs, and L-NPGeNFs in the potential window of 0.005-1.5 V. For a formation of smooth SEI layer, all cells were scanned at a rate of 0.05 C during the first cycle. The first discharge capacities of the GeNFs, H-NPGeNFs, NPGeNFs, and L-NPGeNFs were 1587, 1704, 1678, and 1619 mAh g^{-1} (with initial Coulombic efficiencies (ICEs) of 83.8, 71.6, 81.8 and 82.7%), respectively. Notably, all samples showed different ICEs, which can be explained by their different surface areas. In general, anode materials with a large surface area suffer from severe side reactions, leading to low ICEs. For this reason, the H-NPGeNFs (55.4 m^2/g), which have high surface area compared to other samples, showed noticeably lower ICE than other samples, *i.e.*, GeNFs (4.5 m^2/g), NPGeNFs (33.6 m^2/g), and L-NPGeNFs (20.9 m^2/g). On the contrary, the L-NPGeNFs showed a low surface area, resulting in the highest ICE.

In order to compare the Li^+ storage properties, rate capabilities and long-term cyclabilities of the samples were measured at the same charge/discharge current densities. The NPGeNFs exhibited highly improved rate capabilities compared to GeNFs and other samples throughout stepwise current densities (Figure 4-3c and Figure S10b). Furthermore, the capacity under highest current density (30 C) was almost recovered when current rate was returned to 0.2 C. Similar with the rate capability result, the NPGeNFs also exhibited outstanding capacity retention of 99.5%

(corresponding to an average capacity decay of 0.016% per cycle) compared to the GeNFs (capacity retention: 38%) after 300 cycles at 2.0 C, as shown in Figure 4-3d. By contrast, the L-NPGeNFs and H-NPGeNFs showed poor capacity retention of 62.8% and 92.8%, respectively. Moreover, the GeNFs exhibited even worse capacity value of 383 mAh g^{-1} (corresponding to the capacity retention of 39.2%) after 300 cycles (Figure 4-3d and Figure S10c). Meanwhile, stable cycle performances have been frequently achieved in electrodes with low active mass loading. From a practical point of view, however, reasonably thick electrodes with high mass loading are required to provide sufficient areal capacity (2 mAh cm^{-2}) in many cases.[28] Normally, transport of Li ions is more sluggish in the thick electrode compared to thin electrodes, resulting in degradation of reversible capacity and cycle retention.[29] On the other hand, the NPGeNFs showed higher reversible areal capacity (2.28 mAh cm^{-2}) in the first cycle and retained durable cycling performance over 150 cycles at an increased areal mass loading of 2 mg cm^{-2} owing to the 1D nanoporous morphology of the NPGeNFs which facilitates the diffusion of Li ions across the electrodes (Figure S11).

This excellent cycle performance of the NPGeNFs was further confirmed with electrochemical impedance spectroscopy (EIS) measurements (Figure S12). The NPGeNFs showed almost same charge-transfer resistance (R_{CT}) after both 1st and 100th cycles. By contrast, the GeNFs showed a drastic increase of $R_{CT,}$ resulting in significant capacity degradation after 100 cycles, as clearly shown in Figure 4-3d. Such noticeable rate capability and cycle stability clearly verify the excellent electrochemical property of the NPGeNFs. The cycling stability of the NPGeNFs was further evaluated at much higher current density of 3 C, as displayed in Figure 4-3e. The NPGeNFs retained a high capacity of 678 mAh g^{-1} even after 500 cycles at 3 C, demonstrating a capacity retention of 80.4% and a very small capacity fading of 0.039% per cycle. Moreover, outstanding capacity retention (86.0%) was also obtained even at high rate of 5 C, indicating the excellent electrochemical stability of NPGeNFs (Figure S13).

A huge volume expansion of high-capacity alloying (Ge, Si, Sn, *etc.*) anodes during lithiation results in a serious fracture of electrodes and yields additional electrode/electrolyte interfaces, where further electrolyte decomposition takes place for more SEI layer growth. Both pulverization of active materials and formation of more SEI layers lead to fast capacity fade of LIBs. Thus, rational electrode design with high damage tolerance is important for the high-capacity alloying anodes. The fracture endurance of macroscopic architectures of the NPGeNFs was further investigated in the same manner as the nanoscale dimension. Instead of TEM analysis for discrete NPGeNFs, we conducted cross-sectional SEM analysis for tens-of-micrometer-thick NPGeNF electrode (Figure S14). It should be noted that the volume change of the NPGeNF electrode was only 14.8% which is comparable to that of commercial graphite anodes (10%),

despite its high reversible capacity (1373 mAh g^{-1}) and a large amount of active material (70 wt%) in the electrode. The above-mentioned interesting feature in nanoscale dimension, retaining expanded volume after full delithiation, was also observed in the NPGeNFs electrode. Moreover, TEM images of intact NPGeNFs after 100 cycles indicated a high durability of the NPGeNFs against pulverization (Figure S15). Compared with previously reported Ge nanowire anodes, the NPGeNFs delivered highly improved ICEs and excellent cycle performance, as shown in Table S1.[16,17, 30-33]

In order to confirm the relevance of the NPGeNFs as a promising anode for high-capacity LIB applications, we fabricated a full cell, where the NPGeNF anode was assembled with a commercial $LiCoO_2$ cathode with high mass loading of 13 mg cm^{-2}. The N/P ratio (areal capacity ratio between negative and positive electrodes) was 1.08. The NPGeNF anode was electrochemically prelithiated prior to device assembly for minimization of irreversible capacity. In general, the prelithiation process of high-capacity alloying anodes effectively compensates for their capacity loss and promotes a formation of stable SEI layer.[34] The first galvanostatic charge/discharge voltage profiles of the as-prepared full cell in the potential window of 2.5–4.29 V at 0.1 C were shown in Figure 4-4a. The full cell delivered a reversible capacity of 135 mAh g^{-1} with higher ICE (84%) compared to the NPGeNF half cell (81.8%), which can be attributed to the prelithiation process. Furthermore, the full cell showed stable capacity retention of 73.3% (77.1 mAh g^{-1}) over 200 cycles at a rate of 0.5 C with average Coulombic efficiency of 99.9% (Figure 4-4b,c). It is noteworthy that the full cell delivered an energy density of ~350 Wh kg^{-1}, which is much higher than that of current LIB.[35]

The superior electrochemical properties of both half and full cells can be attributed to the rationally designed structural feature of the NPGeNFs. The nanoporous structure with moderate porosity significantly contributed to the alleviation of volume expansion and reducing lithium ion diffusion length while minimizing side reaction. Concurrently, high durability of the NPGeNFs throughout micrometer length plays a critical role in reliable long-term operation of cells under fast charging/discharging.

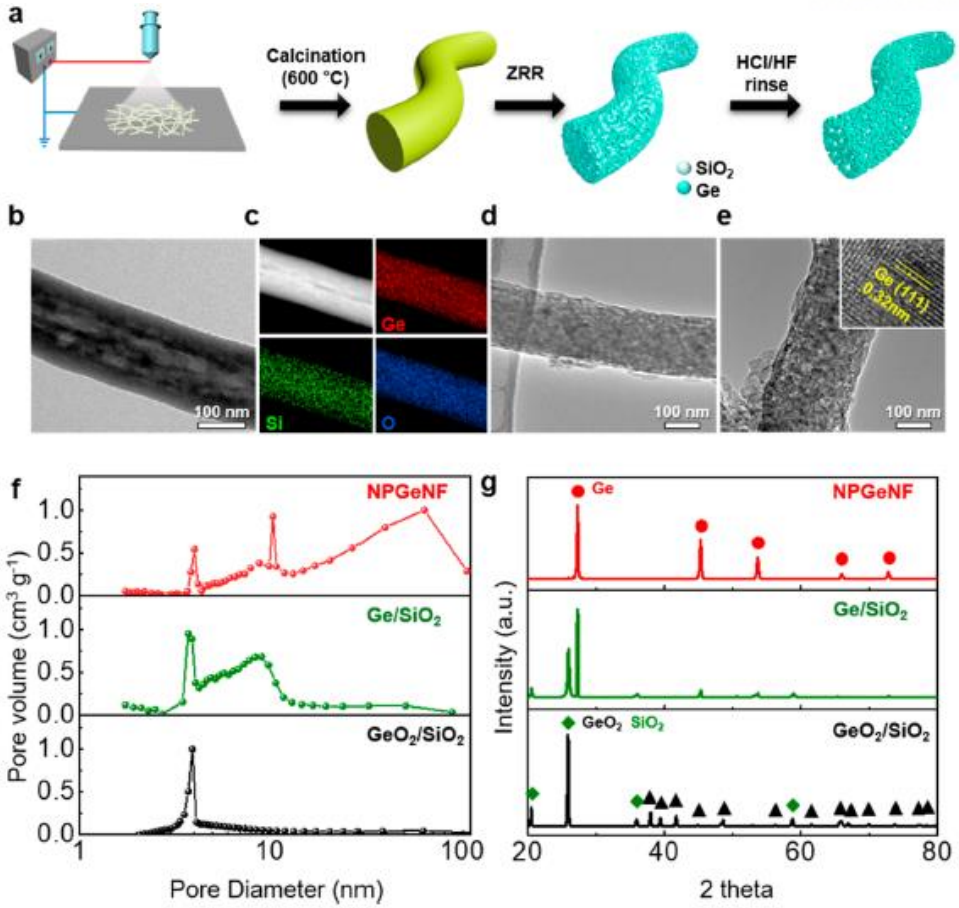

Figure 4-1. Characterization for a series of NPGeNFs. (a) Schematic illustration of the synthetic route. (b) TEM images and (c) HADDFSTEM mapping images after calcination at 600 °C in air. TEM images of (d) HCl and (e) HF treatment. (f) BJH analysis and (g) XRD patterns of each step.

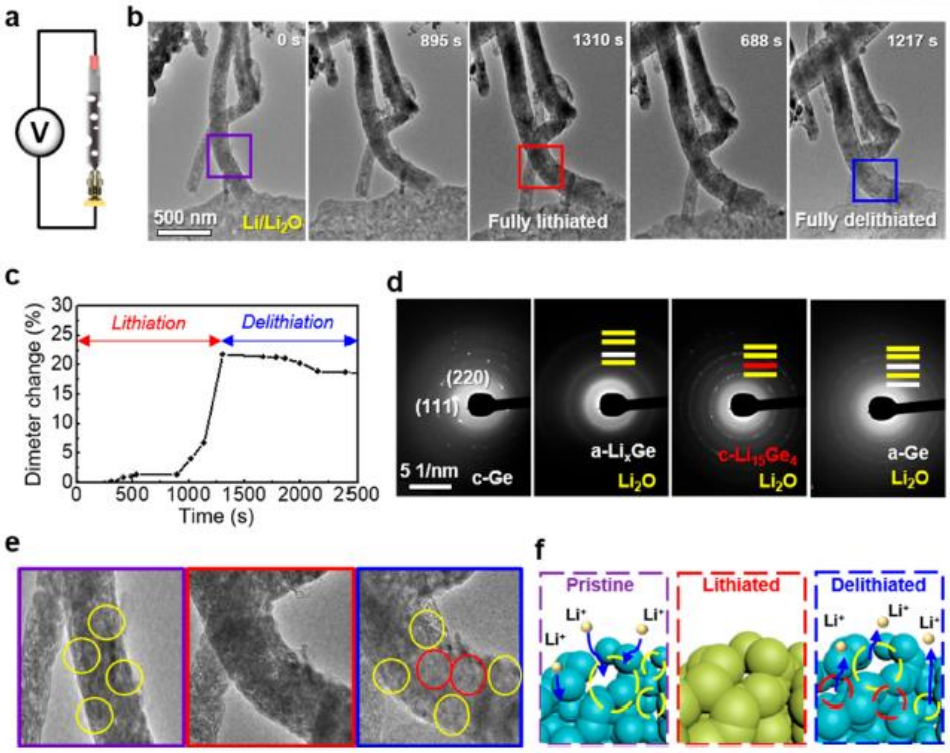

Figure 4-2. *In situ* TEM measurement. (a) Schematic illustration of an in situ TEM cell. An NPGeNF as working electrode was attached to aluminum metal, the Li metal on tungsten was used as the reference electrode/counter electrode, and Li2O covered with Li metal was used as the solid electrolyte. (b) Time-resolved TEM images for lithiation and delithiation. (c) Plot of diameter changes vs time. (d) SAED patterns corresponding to featured TEM images (0, 895, 1310, and 1217 s). TEM images are of the schematic images for pore stabilization and development during lithiation/delithiation processes. (e) Magnified TEM images of pristine, fully lithiated, and fully delithiated NPGeNF. (f) Schematic illustration of the pore memory effect.

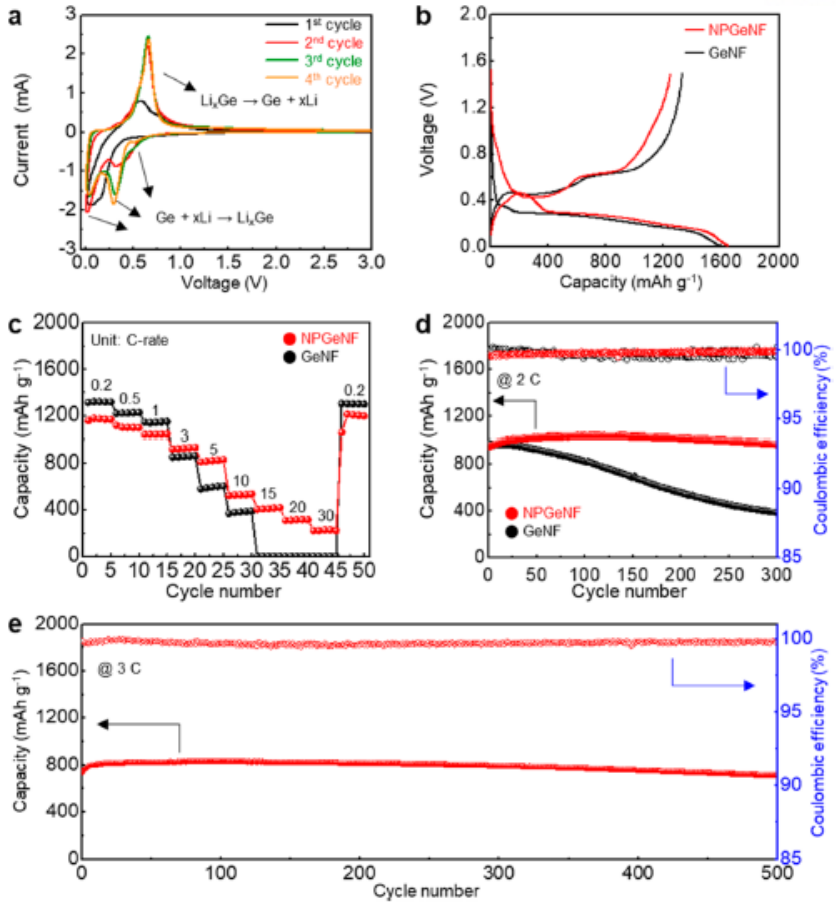

Figure 4-3. Electrochemical properties of NPGeNF and GeNF electrodes. (a) Cyclic voltammetry curves of the NPGeNF electrode. (b) Galvanostatic first cycle discharge/charge voltage profiles at 0.05 C in a potential window of 0.005−1.5 V. (c) Rate capability at various C rates (the same discharge/charge rate). (d) Cycle performance at 2 C. (e) Long-term cycle performance at 3 C during 500 cycles.

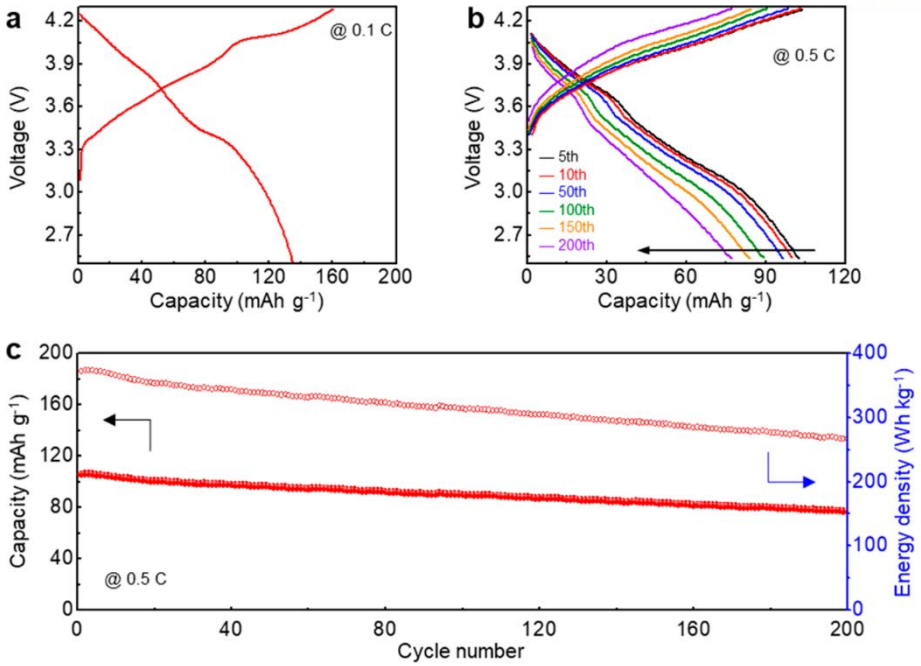

Figure 4-4. Electrochemical properties of an LCO/NPGeNF full cell. (a) Galvanostatic first-cycle discharge/charge voltage profiles at 0.1 C in a potential window of 2.5−4.29 V. (b) Voltage profiles of the LCO/NPGeNF full cell plotted for the fifth, 10th, 50th, 100th, 150th, and 200th cycles. (c) Cycle performance at 0.5 C.

4.4 Conclusion

In summary, we have successfully developed 1D nanoporous Ge with moderate porosity by combining a simple electrospinning with a low-energetic zinc reduction process. The NPGeNFs with micrometer length exhibited excellent Li-ion storage properties including high rate capabilities and long-term cyclability. Furthermore, the NPGeNFs-LCO full cell retained a stable capacity retention with high energy density over 200 cycles. Noteworthy, the methodology described herein facilitates the synthesis of NPGeNF anodes as well as offers the precise control of nanoporosity in a straightforward way compared with a lab-scale NW fabrication via the conventional CVD process with lack of high throughput. We believe that our approach is a significant step toward theintroduction of customized geometries into 1D nanomaterials.

4.5 Reference

1. Wei, Q. L.; Xiong, F. Y.; Tan, S. S.; Huang, L.; Lan, E. H.; Dunn, B.; Mai, L. Q. Porous One-Dimensional Nanomaterials: Design, Fabrication and Applications in Electrochemical Energy Storage. *Adv. Mater.* **2017**, *29*, 1602300.

2. Kim, C.; Jung, J. W.; Yoon, K. R.; Youn, D. Y.; Park, S.; Kim, I. D. A High-Capacity and Long-Cycle-Life Lithium-Ion Battery Anode Architecture: Silver Nanoparticle-Decorated SnO_2/NiO Nanotubes. *ACS Nano* **2016**, *10*, 11317−11326.

3. Jung, J. W.; Ryu, W. H.; Yu, S.; Kim, C.; Cho, S. H.; Kim, I. D. Dimensional Effects of MoS_2 Nanoplates Embedded in Carbon Nanofibers for Bifunctional Li and Na Insertion and Conversion Reactions. *ACS Appl. Mater. Interfaces* **2016**, *8*, 26758−26768.

4. Koo, W. T.; Jang, H. Y.; Kim, C.; Jung, J. W.; Cheong, J. Y.; Kim, I. D. MOF Derived $ZnCo_2O_4$ Porous Hollow Spheres Functionalized with Ag Nanoparticles for a Long-Cycle and High-Capacity Lithium Ion Battery Anode. *J. Mater. Chem. A* **2017**, *5*, 22717−22725.

5. Jung, J.-W.; Ryu, W.-H.; Shin, J.; Park, K.; Kim, I.-D. Glassy Metal Alloy Nanofiber Anodes Employing Graphene Wrapping Layer: Toward Ultralong-Cycle-Life Lithium-Ion Batteries. *ACS Nano* **2015**, *9*, 6717−6727.

6. Yao, X.; Guo, G. L.; Zhao, Y.; Zhang, Y.; Tan, S. Y.; Zeng, Y. F.; Zou, R. Q.; Yan, Q. Y.; Zhao, Y. L. Synergistic Effect of Mesoporous Co_3O_4 Nanowires Confined by N-Doped Graphene Aerogel for Enhanced Lithium Storage. *Small* **2016**, *12*, 3849−3860.

7. Yan, C. S.; Chen, G.; Zhou, X.; Sun, J. X.; Lv, C. D. Template-Based Engineering of Carbon-Doped Co_3O_4 Hollow Nanofibers as Anode Materials for Lithium-Ion Batteries. *Adv. Funct. Mater.* **2016**, *26*, 1428−1436.

8. Choi, S.; Kim, J.; Hwang, D. Y.; Park, H.; Ryu, J.; Kwak, S. K.; Park, S. Generalized Redox-Responsive Assembly of Carbon-Sheathed Metallic and Semiconducting Nanowire Heterostructures. *Nano Lett.* **2016**, *16*, 1179−1185.

9. Liu, N.; Hu, L.; McDowell, M. T.; Jackson, A.; Cui, Y. Prelithiated Silicon Nanowires as an Anode for Lithium Ion Batteries. *ACS Nano* **2011**, *5*, 6487−6493.

10. Peled, E.; Patolsky, F.; Golodnitsky, D.; Freedman, K.; Davidi, G.; Schneier, D. Tissue-Like Silicon Nanowires-Based Three-Dimensional Anodes for High-Capacity Lithium Ion Batteries. *Nano Lett.* **2015**, *15*, 3907−3916.

11. Lim, Y. R.; Jung, C. S.; Im, H. S.; Park, K.; Park, J.; Cho, W. I.; Cha, E. H. Zn_2GeO_4 and Zn_2SnO_4 Nanowires for High-Capacity Lithium- and Sodium-Ion Batteries. *J. Mater. Chem. A* **2016**, *4*, 10691−10699.

12. Wang, N. N.; Bai, Z. C.; Qian, Y. T.; Yang, J. Double-Walled Sb@TiO_{2-X} Nanotubes as a Superior High-Rate and Ultralong-Lifespan Anode Material for Na-Ion and Li-Ion Batteries. *Adv. Mater.* **2016**, *28*, 4126−4133.

13. Chan, C. K.; Peng, H. L.; Liu, G.; McIlwrath, K.; Zhang, X. F.; Huggins, R. A.; Cui, Y. High-Performance Lithium Battery Anodes Using Silicon Nanowires. *Nat. Nanotechnol.* **2008**, *3*, 31−35.

14. Chan, C. K.; Zhang, X. F.; Cui, Y. High Capacity Li Ion Battery Anodes Using Ge Nanowires. *Nano Lett.* **2008**, *8*, 307−309.

15. Kim, C.; Hwang, G.; Jung, J. W.; Cho, S. H.; Cheong, J. Y.; Shin, S.; Park, S.; Kim, I. D. Fast, Scalable Synthesis of Micronized Ge_3N_4@C with a High Tap Density for Excellent Lithium Storage. *Adv. Funct. Mater.* **2017**, *27*, 1605975.

16. Kim, G. T.; Kennedy, T.; Brandon, M.; Geaney, H.; Ryan, K. M.; Passerini, S.; Appetecchi, G. B. Behavior of Germanium and Silicon Nanowire Anodes with Ionic Liquid Electrolytes. *ACS Nano* **2017**, *11*, 5933−5943.

17. Xiao, W.; Zhou, J.; Yu, L.; Wang, D. H.; Lou, X. W. Electrolytic Formation of Crystalline Silicon/Germanium Alloy Nanotubes and Hollow Particles with Enhanced Lithium-Storage Properties. *Angew. Chem., Int. Ed.* **2016**, *55*, 7427−7431.

18. Kim, W.-S.; Hwa, Y.; Shin, J.-H.; Yang, M.; Sohn, H.-J.; Hong, S.-H. Scalable Synthesis of Silicon Nanosheets from Sand as an Anode for Li-Ion Batteries. *Nanoscale* **2014**, *6*, 4297−4302.

19. Morales-Narvaez, E.; Sgobbi, L. F.; Machado, S. A. S.; Merkoci, A. Graphene-Encapsulated Materials: Synthesis, Applications and Trends. *Prog. Mater. Sci.* **2017**, *86*, 1−24.

20. Liu, S.; Feng, J.; Bian, X.; Qian, Y.; Liu, J.; Xu, H. Nanoporous Germanium as High-Capacity Lithium-Ion Battery Anode. *Nano Energy* **2015**, *13*, 651−657.

21. Yang, Y. H.; Liu, S.; Bian, X. F.; Feng, J. K.; An, Y. L.; Yuan, C. Morphology- and Porosity-Tunable Synthesis of 3D Nanoporous SiGe Alloy as a High-Performance Lithium-Ion Battery Anode. *ACS Nano* **2018**, *12*, 2900−2908.

22. Choi, S.; Kim, J.; Choi, N. S.; Kim, M. G.; Park, S. Cost-Effective Scalable Synthesis

of Mesoporous Germanium Particles *via* a Redox-Transmetalation Reaction for High-Performance Energy Storage Devices. *ACS Nano* **2015,** *9*, 2203−2212.

23. Choi, S.; Cho, Y. G.; Kim, J.; Choi, N. S.; Song, H. K.; Wang, G. X.; Park, S. Mesoporous Germanium Anode Materials for Lithium-Ion Battery with Exceptional Cycling Stability in Wide Temperature Range. *Small* **2017**, *13*, 1603045.

24. Seng, K. H.; Park, M.-H.; Guo, Z. P.; Liu, H. K.; Cho, J. Self-Assembled Germanium/Carbon Nanostructures as High-Power Anode Material for the Lithium-Ion Battery. *Angew. Chem., Int. Ed.* **2012**, *51*, 5657−5661.

25. Liu, X. H.; Huang, S.; Picraux, S. T.; Li, J.; Zhu, T.; Huang, J. Y. Reversible Nanopore Formation in Ge Nanowires During Lithiation-Delithiation Cycling: An *In Situ* Transmission Electron Microscopy Study. *Nano Lett.* **2011**, *11*, 3991−3997.

26. Liu, X. H.; Liu, Y.; Kushima, A.; Zhang, S.; Zhu, T.; Li, J.; Huang, J. Y. *In Situ* Tem Experiments of Electrochemical Lithiation and Delithiation of Individual Nanostructures. *Adv. Energy Mater.* **2012**, *2*, 722−741.

27. Wang, X. Y.; Fan, L.; Gong, D. C.; Zhu, J.; Zhang, Q. F.; Lu, B. G. Core-Shell Ge@Graphene@TiO_2 Nanofibers as a High-Capacity and Cycle-Stable Anode for Lithium and Sodium Ion Battery. *Adv. Funct. Mater.* **2016**, *26*, 1104−1111.

28. Hwang, J.; Jo, C.; Kim, M. G.; Chun, J.; Lim, E.; Kim, S.; Jeong, S.; Kim, Y.; Lee, J. Mesoporous Ge/GeO_2/Carbon Lithium-Ion Battery Anodes with High Capacity and High Reversibility. *ACS Nano* **2015**, *9*, 5299−5309.

29. Billaud, J.; Bouville, F.; Magrini, T.; Villevieille, C.; Studart, A. R. Magnetically Aligned Graphite Electrodes for High-Rate Performance Li-Ion Batteries. *Nat. Energy* **2016**, *1*, 16097.

30. Yuan, F.-W.; Yang, H.-J.; Tuan, H.-Y. Alkanethiol-Passivated Ge Nanowires as High-Performance Anode Materials for Lithium-Ion Batteries: The Role of Chemical Surface Functionalization. *ACS Nano* **2012**, *6*, 9932−9942.

31. Lee, G.-H.; Shim, H.-W.; Kim, D.-W. Superior Long-Life and High-Rate Ge Nanoarrays Anchored on Cu/C Nanowire Frameworks for Li-Ion Battery Electrodes. *Nano Energy* **2015**, *13*, 218−225.

32. Gu, J.; Collins, S. M.; Carim, A. I.; Hao, X.; Bartlett, B. M.; Maldonado, S. Template-Free Preparation of Crystalline Ge Nanowire Film Electrodes *via* an Electrochemical Liquid-Liquid-Solid Process in Water at Ambient Pressure and Temperature for Energy

Storage. *Nano Lett.* **2012**, *12*, 4617−4623.

33. Kim, H.; Son, Y.; Park, C.; Lee, M.-J.; Hong, M.; Kim, J.; Lee, M.; Cho, J.; Choi, H. C. Germanium Silicon Alloy Anode Material Capable of Tunable Overpotential by Nanoscale Si Segregation. *Nano Lett.* **2015**, *15*, 4135−4142.

34. Kim, H. J.; Choi, S.; Lee, S. J.; Seo, M. W.; Lee, J. G.; Deniz, E.; Lee, Y. J.; Kim, E. K.; Choi, J. W. Controlled Prelithiation of Silicon Monoxide for High Performance Lithium-Ion Rechargeable Full Cells. *Nano Lett.* **2016**, *16*, 282−288.

35. Cho, J.; Jeong, S.; Kim, Y. Commercial and Research Battery Technologies for Electrical Energy Storage Applications. *Prog. Energy Combust. Sci.* **2015**, *48*, 84−101.

Chapter V. Intramolecuar deformation of zeotype-borogermanate toward a three-dimensional porous germanium anode for high-rate lithium storage

5.1 Introduction

Zeolite is a well-known porous material with three-dimensional (3D) crystalline structure, which possesses the unique properties such as physical/chemical stabilities, non-toxicity, and large internal pore volumes with well-defined aperture. The zeolite, which was formed naturally but produced industrially in a large scale, has been commercially applied to catalysts, ion-exchangers, and adsorbents.[1,2] In addition, their characteristics have also been exploited as supporting materials for cathode, anode, and separator in lithium-ion batteries (LIBs).[3–5] Although conventional zeolites have intrinsic limitation to directly apply to the LIBs due to their poor performance caused by low conductivity and numerous inactive sites, their unique architectures have received significant attention especially in terms of porous material. On the other hand, multiscale hyperporous Si flakes and ultrathin Si nanosheets from Si-rich zeolite series of talc and clay minerals have been synthesized *via* a selective magnesiothermic reduction and have been applied to LIB anode.[6,7] However, methods mentioned above require a harmful etchant such as strong nitric acid and subsequent hydrofluoric acid. Also, the synthetic method for conversion from zeolite to porous Ge anode materials has been still undeveloped.

Recently, alloy-type materials have emerged for high-performance LIBs.[8–10] In particular, Ge-based anode materials have emerged as one of the most promising candidates compared with Si-based materials in LIBs due to their higher Li diffusivity (~ 400 times greater than that of Si at room temperature) and electronic conductivity (10^4 times higher than that of Si).[11,12] Although theoretical gravimetric capacity of Ge (1384 mAh g^{-1} in the form of $Li_{15}Ge_4$) is lower than Si (3579 mAh g^{-1} in the form of $Li_{15}Si_4$), volumetric capacity of Ge (7366 Ah L^{-1}) is relatively similar to that of Si (8334 Ah L^{-1}).[13] Their attractive features make them potentially interesting for high power application with rapid charge/discharge characteristics such as portable electronic devices, electrical vehicles, and large-scale energy storage. Unfortunately, even though bare Ge anode has an advantage as to unique behavior for Li-ion insertion/extraction, it increases mechanical stress by a drastic volume expansion (> 230 %) during the lithiation process ($Ge + xLi^+ + xe^- \leftrightarrow Li_xGe$, $0 < x < 3.75$). As a result, a severe capacity fading occurs due to pulverization

of active materials and loss of the electrical contact from the current collector.[14,15] To solve these issues, several strategies have been proposed through improving the structural stability and electrochemical performance including (i) morphology control of materials,[16,17] (ii) introduction of active/inactive buffer matrix,[18,19] (iii) employment of porous materials[20,21] and (iv) synthesis of amorphous materials.[22,23] In particular, porous materials with micrometer-scale architecture constructed by nanostructured particles generally provide several advantages which can improve electrochemical performances, including a facile penetration of electrolytes, alleviation of volume expansion, enhancement of electronic transport, and reduction of ion-diffusion length.[24–26] However, conventional approaches for synthesizing porous Ge materials, such as template-assisted method,[27] electrodeposition[28,29] and vapor deposition[30], require additional procedure for etching the templates in a harmful solution to manufacture the desired porous structures.

Here we demonstrate, for the first time, the synthesis of three-dimensional porous Ge material (denoted as 3D-pGe) from zeotype-borogermanate ($K_2B_2Ge_3O_{10}$) through a thermal deformation in closed system, etching with warm water, and subsequent hydrogen reduction steps. The well-designed 3D-pGe is micrometer-scale architecture constructed by nanostructured Ge particles, showing the high-porosity in overall frameworks and these micro-size secondary particles features high tap density compared with simple Ge nanostructures, leading to a high volumetric density. In particular, as-formed pores play a significant role in a facile electrolyte penetration, effective Li-ion transfer into whole active materials, and mitigation of a large volume change derived from Li-alloying/dealloying reaction. In addition, this architecture leads to considerable contribution of surface-controlled reaction with pseudocapacitive behavior responsible for rate performance (342 mAh g^{-1} at 10 C). Notably, the well-designed 3D-pGe anode delivers a high reversible capacity (770 mAh g^{-1}) with an outstanding coulombic efficiency per cycle (> 99.8 %) after 250 cycles at 1 C and solid electrolyte interphase (SEI) layers formed at first cycle stably maintains own shapes during repeated lithiation/delithation without further reconstruction. Furthermore, a full cell coupled with $LiCoO_2$ cathode shows stable cyclability with 86.7% capacity retention during 200 cycles without dramatic capacity drop.

5.2 Experimental method

Materials. Germanium oxide (99.999%, GeO_2) was purchased from Sigma-Aldrich. 1,4-diaminobutane (≥99%), ethylene glycol (≥99%), potassium tetraborate tetrahydrate (≥99.5%, $K_2B_4O_7{\cdot}4H_2O$) and germanium power (~100 mesh, 99.999%) were purchased from Alfa Aesar. All the chemicals were used without further purification.

Synthesis of KBGO. To synthesize the zeotype-borogermanate ($K_2B_2Ge_3O_{10}$, denoted as KBGO),[31,32] 3.12 g of GeO_2 and 24 g of 1,4-diaminobutane were dispersed in solution with 30 mL of deionized water and 45 mL of ethylene glycol. After stirring for 1 h at room temperature, 9.51 g of $K_2B_4O_7{\cdot}4H_2O$ was added and stirred for another 1 h. Then, the mixture was transferred to 300 mL of Teflon-lined autoclave and heated in an electric oven at 180 °C at a rate of 5 °C min^{-1} for 4 days. The precipitate was filtered with ethanol three times and dried in vacuum oven at 80 °C overnight. Finally, sample was heated to 600 °C for 6 h under air condition to remove the impurity. To check the optimized size and morphology of KBGO, the reaction time was controlled to 1, 2, 7 days, respectively.

Synthesis of anode materials. As-prepared KBGO was heated in a closed-vessel furnace at 800 °C for 12 h under argon atmosphere to form the $K_2Ge_4O_9$, GeO_2, K_2O, and B_2O_3 through thermal deformation. Then, the byproducts of GeO_2, K_2O, and B_2O_3 were removed by stirring with warm water at 60 °C for 12 h, followed by filtering with ethanol and drying overnight at 80 °C. The resulting $K_2Ge_4O_9$ (KGO) reacted with forming gas (95/5 % of Ar/H_2) at a flow rate of 500 mL min^{-1} at 800 °C for 6 h. Finally, the resulting 3D-pGe was washed with ethanol and dried overnight at 80 °C.

Characterization. Surface morphologies were carried out with a field emission scanning electron microscopy (FE-SEM, Nova 230, FEI). The morphological investigations were analyzed by a high resolution transmission electron microscopy (HRTEM) and scanning TEM with an acceleration voltage of 200 kV, and an energy-dispersive X-ray spectroscopy (EDX) was used to characterize the element of samples (JEM-2100F, JEOL). Surface analysis of samples were investigated by an X-ray photoelectron spectroscopy (XPS, K-alpha, ThermoFisher) with a beam of monochromated aluminum X-ray source. The crystallographic information was determined through a high power X-ray diffractometer (XRD, MAX 2500V, Rigaku, Cu Kα radiation λ = 1.54059 Å) with scanning angle 2θ ranging from 20° to 60°. Surface areas of samples were determined using N_2 adsorption–desorption isotherms at 77 K (ASAP 2020, Micromeritics Instrument) with the Brunauer–Emmett–Teller (BET) method.

Thermogravimetric analysis (TGA) was measured until 800 °C at a rate of 10 °C min^{-1} under N_2 atmosphere (Q500, TA). Raman spectroscopy was carried out on a confocal Raman (alpha 300R, WITec) with a laser wavelength of 532 nm.

Electrochemical Test. A viscous slurry, which composed of active materials, conductive materials (Super-P), and poly (acrylic acid) (PAA)/ carboxymethyl cellulose (CMC) (1:1 weight ratio) as a binder with weight ratio of 8:1:1, was casted on Cu foil to fabricate electrodes (loading mass: 1.2-1.4 mg cm^{-2}). In the case of $LiCoO_2$ (LCO) cathode, the weight ratio was 90:5:5 (LCO: Super-P: polyvinylidene fluoride). And the slurry was casted on Al foil. The LCO has loading mass of 12.7 mg cm^{-2}. All electrodes were assembled in Ar-filled glove box using 2016-type coin cells (Welcos) with Li metal as the counter electrode (half-cell) and LCO (full-cell) as the cathode. Also, polyethylene membrane (Celgard) as the separator and liquid electrolyte, which consists of ethylene carbonate (EC)/diethyl carbonate (DEC) (3:7 volume ratio) with 10 wt% of fluoroethylene carbonate (FEC) and 1.3M $LiPF_6$ salt, were used. Galvanostatic measurement was conducted using a battery cycler (Wanatech, WBCS-3000) under constant temperature (25° C). The potential range of half-cells was limited from 0.005 V to 1.5 V (formation cycle) and used for subsequent cycles in the range of 0.01-1.5 V. Meanwhile, full-cells were tested in 2.5-4.29 V voltage range. The calculation method of energy density has been described in Supporting information (Equation S1). Electrochemical impedance spectroscopy (EIS) results were obtained in the frequency range of 10^{-2} - 10^{6} Hz.

5.3 Results and discussion

A schematic illustration of synthesis process is shown in Figure 5-1a. Zeotype-borogermanate ($K_2B_2Ge_3O_{10}$; denoted as KBGO) was synthesized by a simple hydrothermal reaction as the following equation.

$$K_2B_4O_7 + 3GeO_2 \rightarrow K_2B_2Ge_3O_{10} + 2H_3BO_3 \quad (1)$$

Scanning electron microscopy (SEM) images of the resulting KBGO are shown in Figure 5-1b and S1 in the ESI.† In addition, scanning transmission electron microscopy-high angle annular dark field (STEM-HAADF) image and energy-dispersive X-ray spectroscopy (EDS) mapping of optimized KBGO material are in Figure S2. This overall framework has a chiral structure based on chain-like $[B_2Ge_3O_{10}]_n^{2n-}$ polyanions to form the 3D open frameworks with long, narrow-shaped, helical channels by ABAB stacking. These channels are composed of BO_4 and GeO_4 tetrahedral structures, and K^+ ions filled in channels are coordinated by O atoms.[31,32] Then, the composite material was formed by decomposition of KBGO during a thermal treatment in the closed system at 800 °C, as the following deformation equation.

$$2K_2B_2Ge_3O_{10} \rightarrow K_2Ge_4O_9 + K_2O + 2B_2O_3 + 2GeO_2 \quad (2)$$

After this step, molten salts of K_2O (melting point ~ 740 °C) and B_2O_3 (melting point ~ 450 °C) were hardened on the whole surface of $K_2Ge_4O_9$ particles (Figure 5-1c, denoted as KGO with byproducts). To confirm the decomposition of KBGO and differences in structures of KBGO and KGO, thermogravimetric analysis-differential scanning calorimeter (TGA-DSC) and crystal structures were studied (Figure S3 and S4). After etching in warm water, byproducts including K_2O, B_2O_3, and GeO_2 were removed, resulting in generation of external voids in the $K_2Ge_4O_9$ particle (Figure 5-1d, denoted as KGO). Finally, micron-scale 3D-pGe constructed by Ge nanoparticles was formed after hydrogen reduction of KGO (Figure 5-1e, denoted as 3D-pGe). Morphology and crystalline structure of the 3D-pGe displayed numerous pores in the overall frameworks with high crystalline Ge (111) particles, showing the lattice spacing of 0.33 nm and well-ordered fast Fourier transform (FFT) patterns (Figure 5-1f–h).

To verify the proposed concept of conversion from artificial zeolite to 3D-pGe anode material, an X-ray photoelectron spectroscopy (XPS) was performed to clarify the differences in the binding characteristics of each sample. The peaks of K $2p_{3/2}$ core level at KBGO and KGO appeared as relatively weak binding energies at 292.6 eV and 291.8 eV, respectively, because K^+ ions coordinate to oxygen atoms,[32,33] whereas the peaks for KGO with byproducts were observed at higher binding energies of K $2p_{3/2}$ (~293.1 eV) due to the formation of K_2O compounds after thermal deformation (Figure 5-2a).[34] However, these peaks disappeared after hydrogen reduction. The broad peak of KBGO at B 1s core level was consistent with boron in an oxidation state (~190 eV), and the peaks of KGO with byproducts indicated the formation of B_2O_3 (~193 eV) as shown in Figure 5-2b.[35,36] However, the peaks of boron components disappeared after etching in warm water. It can be concluded that the as-prepared byproducts of K_2O, B_2O_3 and GeO_2 were successfully removed by warm water, but a cubic architecture of KGO was well preserved. The binding energies of Ge 3d were deconvoluted into individual peaks at 32.7, 30.8, and 29.2 eV, corresponding to GeO_2, GeO_x, and Ge, respectively (Figure 5-2c). The peaks of KBGO, KGO with byproducts, and KGO at Ge 3d mainly correspond to GeO_x because their materials consist of covalent Ge–O bonds. After hydrogen reduction, the sharp peak of 3D-pGe indicates high crystalline Ge, which also coincided with TEM image and Raman spectrum showing a single sharp peak of crystal Ge phase (Figure 5-1h and S5). To further confirm the crystallographic information of each sample, X-ray diffraction (XRD) patterns were obtained (Figure 5-2d). The XRD patterns for KBGO are in good agreement with previous reports.[32] The XRD patterns of KGO with byproducts showed major peaks corresponding to KGO (JCPDS #85-0966) and minor peaks consisting of K_2O (labeled ♠), B_2O_3 (labeled ♦), and GeO_2 (labeled ♣) byproducts.[37–39] All the peaks of byproducts disappeared after etching in warm water, whereas the peaks of KGO showed no obvious change. The diffraction peaks of the 3D-pGe sample at 27.3°, 45.3° and 53.7° are mainly attributed to the (111), (220) and (311) lattice planes of high crystalline Ge, respectively (JCPDS #04-0545). Brunauer−Emmett−Teller (BET) surface areas of KBGO, KGO with byproducts, KGO, and 3D-pGe were 0.59, 0.26, 1.92, and 7.73 $m^2\ g^{-1}$, respectively, which showed relatively low surface area because of micrometer-sized architectures (Figure 5-2e). The sharp peaks for 3D-pGe and KGO at high relative pressure ($P/P_0 > 0.9$) indicated the presence of mesopores. The pore size distribution for 3D-pGe showed that sharp peaks ranging from 2 to 4 nm and broad peaks ranging from 5 to 20 nm were observed due to micron-scale architecture constructed by Ge nanoparticles (Figure 5-2f).

Furthermore, electrochemical properties of 3D-pGe anode were evaluated where discharge/charge galvanostatic measurements were conducted at 25°C. For comparison of 3D-pGe anode, the micrometer-sized Ge was assembled in the same manner (denoted as Bulk-Ge). The characterization results of bulk-Ge were shown in Figure S6. Figure S7 shows the differential capacity curves of 3D-pGe electrodes where peaks observed in the first cycle were slightly shifted in the second cycle due to a formation of SEI layers and an amorphization of Ge crystal. Then, in subsequent cycles, the Ge underwent lithiation process at 0.38 and 0.17 V in the cathodic part. For an anodic part, two kinds of peaks were developed at 0.49 and 0.60 V related to dealloying process into Ge and Li, showing stable peak positions.[40,41] The galvanostatic charge/discharge profiles exhibited that the bulk-Ge and the 3D-pGe electrodes showed reversible capacities of 1146.5 and 1341.1 mAh g^{-1} at C/20 after a formation cycle with initial Coulombic efficiencies (ICEs) of 89.5 and 92.3%, respectively (Figure 5-3a). The well-designed morphology and micro-sized secondary particles realized such high ICE because the porosity can facilitate the electrolyte penetration and the high crystalline Ge can enhance the electrical conductivity leading to facile kinetics of electrode.[20,42] Besides, the 3D-pGe exhibited excellent rate capability even at high C-rate in Figure 5-3b (1 C = 1147 mA g^{-1}). With the help of mesoporous structure providing short Li-ion diffusion length and metallic Ge with relatively higher electronic conductivity, the 3D-pGe showed reasonable capacities of 895, 570, 342, and 255 mAh g^{-1} at 1, 5, 10, and 15 C, respectively, whereas bulk-Ge did not facilitate the reaction over 10 C. Moreover, the 3D-pGe electrode successfully recovered its initial capacity when the C-rate returned from 15 C to C/5 (capacity retention of 98.6% compared with initial capacity). In addition, the 3D-pGe electrode delivered outstanding cycle retention without any capacity decay at C/5 (Figure 5-3c). Electrochemical impedance spectroscopy (EIS) results (Figure 5-3d) and TEM images of cycled samples surely verified cyclic performance (Figure 5-3e–h). 3D-pGe electrode did not show SEI layer resistance change corresponding to the stable SEI layer and structure integrity after cycling, which induces the high CE performance. In contrast to 3D-pGe electrode, bulk-Ge experienced uncontrollable resistance increase related to unstable SEI layer as well as sluggish kinetics of a charge transfer by nonporous bulky structure. Along with EIS results, the structure suffered from cracks because the Li insertion into the active materials induced mechanical stress, leading to thick and continuous SEI layer reformation. Also, in whole electrode, this structure failure resulted in tremendous change of the electrode thickness (over 300%) as compared to the 3D-pGe electrode which exhibited superior stress tolerance with 50% thickness change after 100th cycle (Figure S8). This comparison

indicates that high-porosity in overall frameworks can suppress the mechanical stress and contribute to the stable cyclability through the memory effect of pore sites in Ge-based electrode.[40]

On the basis of cyclic voltammetry (CV) curves at various scan rates from 0.2 to 5.0 mV s^{-1} in Figure 5-4a and 4b, the behavior of electrode is related to a pseudocapacitance.[43,44] In Figure 5-4c, the calibrated graph of *b*-value vs. potential elucidates the tendency of the electrode in every voltage state on lithiation. The *b*-value of 0.5 means that overall reaction is attributed to diffusion-controlled behavior (faradaic current) while *b*-value of 1.0 ascribes to the contribution of surface-controlled behavior (capacitive current) in overall reaction. The power law relationship can be described as measured current (*i*) and scan rate (ν), derived from the following equation.[45]

$$i = a\nu^b \quad (3)$$

The 3D-pGe electrode showed higher *b*-value due to fast kinetics by surface-confined reaction process between electrode and electrolyte, which induced the stable cyclic and rate performance even at high C-rate.[46-48] Furthermore, we calculated the capacity contribution of capacitive and faradic current derived from the following equation which certainly demonstrates the effect of pore construction.[13]

$$i = k_1\nu + k_2\nu^{1/2} \quad (4)$$

where $k_1\nu$ and $k_2\nu^{1/2}$ indicate the amounts of capacitive and faradaic current in total current, respectively. The 3D-pGe electrode consisted of capacitive current of 74% while the bulk-Ge electrode showed capacitive current of only 43% at 1.0 mV s^{-1} (Figure 5-4d and 4e). Besides, the 3D-pGe electrode was more sensitive to the change of scan rates, especially in terms of capacitive current as shown in Figure 5-4f, Tables S1, and S2.

In this regard, it is surely understood that a long-term cycling performance of 3D-pGe could show outstanding capacity of 770 mAh g^{-1} even at 1 C after 250 cycles with a high CE per cycle (>99.5 %) without any supporting materials (Figure 5-5a). For a practical application, the full-cell fabricated with $LiCoO_2$ (LCO) cathode and 3D-pGe anode was investigated. The initial voltage profile and electrochemical performance of LCO are displayed in Figure S9. The galvanostatic charge/discharge profile showed the first discharge capacity of 146.1 mAh g^{-1} with an ICE of 76.8 % at C/10 (Figure S10). Figure 5-5b demonstrates that the cell enables to operate at high power density of 365 W kg^{-1}

(187 W kg^{-1} =1 C) and realize energy density of 348 Wh kg^{-1}. Furthermore, the cell also performed 50% capacity retention for 3C with respect to C/5. With the rate durability, the cell exhibited at first both high areal and gravimetric capacity (1.6 mAh cm^{-2} and 143 mAh g^{-1}) at C/5 as well as capacity retention of 86.8% at C/2 without a dramatic capacity drop over 200 cycles (Figure 5-5c). Besides, steadily high coulombic efficiency (average 98.8% except for the ICE) of the full-cell in Figure 5-5d. The considerable tap density of 3D-pGe sample and durable energy/power density are summarized in Tables S3 and S4, which suggests that this material can realize viable large-scale LIBs.

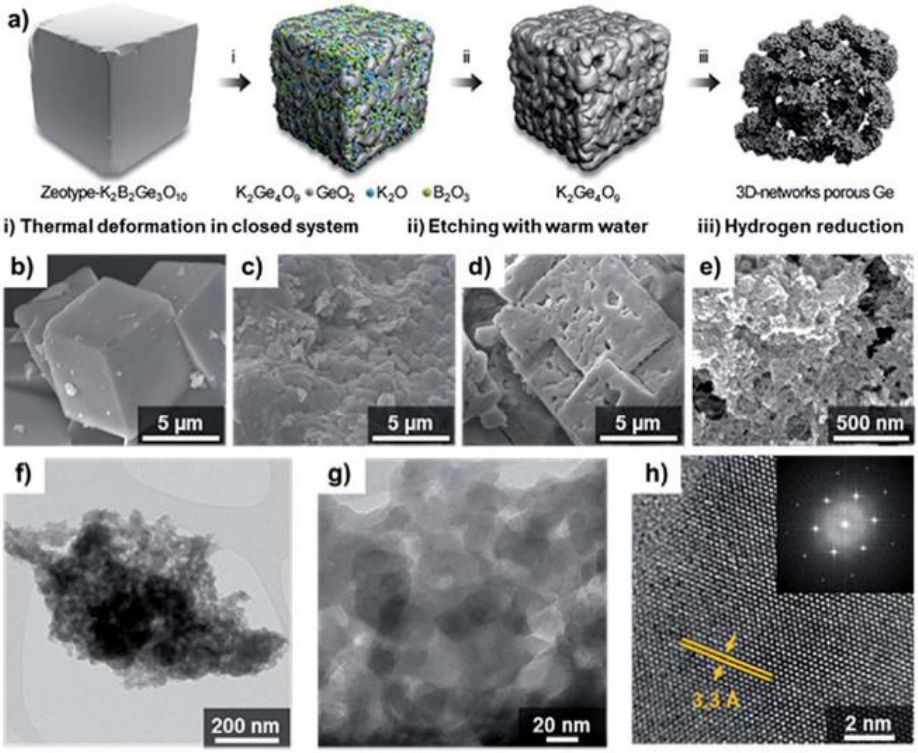

Figure 5-1. (a) The schematic illustration for synthetic routes of three-dimensional porous Ge: (i) deformation of zeotype-$K_2B_2Ge_3O_{10}$ to form $K_2Ge_4O_9$, GeO_2, K_2O, and B_2O_3 with heat treatment in closed system. (ii) Etching the byproducts of K_2O, B_2O_3, and GeO_2 with warm water. (iii) Hydrogen reduction of $K_2Ge_4O_9$ to form three-dimensional porous Ge. SEM images of (b) zeotype-$K_2B_2Ge_3O_{10}$ (denoted as KBGO), (c) composite materials with $K_2Ge_4O_9$, GeO_2, K_2O, and B_2O_3 (denoted as KGO with byproducts), (d) $K_2Ge_4O_9$ (denoted as KGO), and (e) three-dimensional porous Ge (denoted as 3D-pGe). (f–h) HRTEM image of 3D-pGe. The inset of (h) shows FFT image.

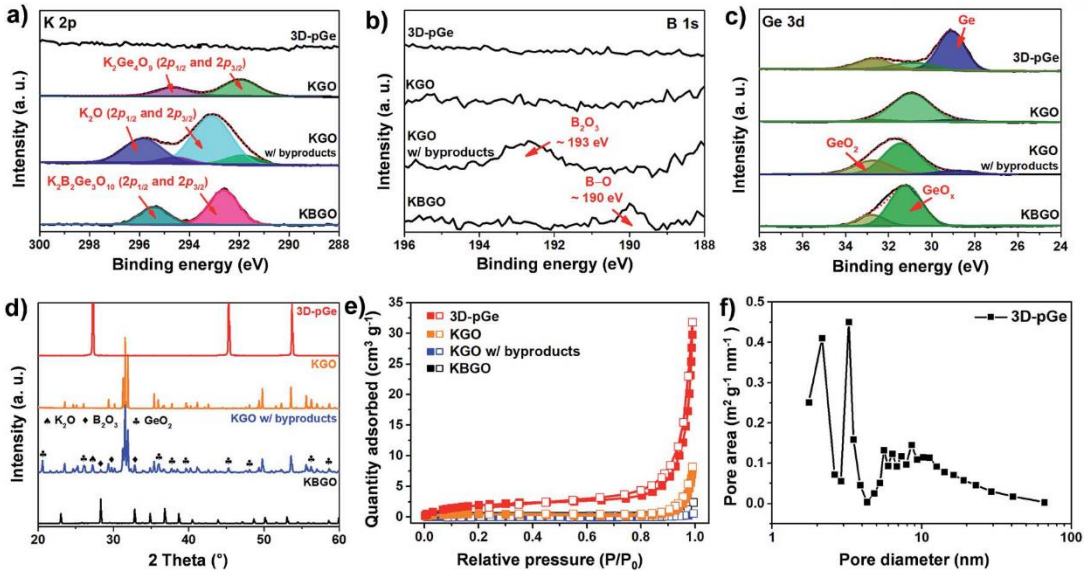

Figure 5-2. X-ray photoelectron spectroscopy (XPS) spectra for KBGO, KGO with byproducts, KGO, and 3D-pGe of (a) K 2p, (b) B 1s, and (c) Ge 3d. (d) X-ray diffraction (XRD) patterns. (e) BET surface area calculated from nitrogen (77 K) adsorption–desorption isotherms, denoted by solid/hollow square symbols, and (f) their corresponding pore size distribution of 3D-pGe.

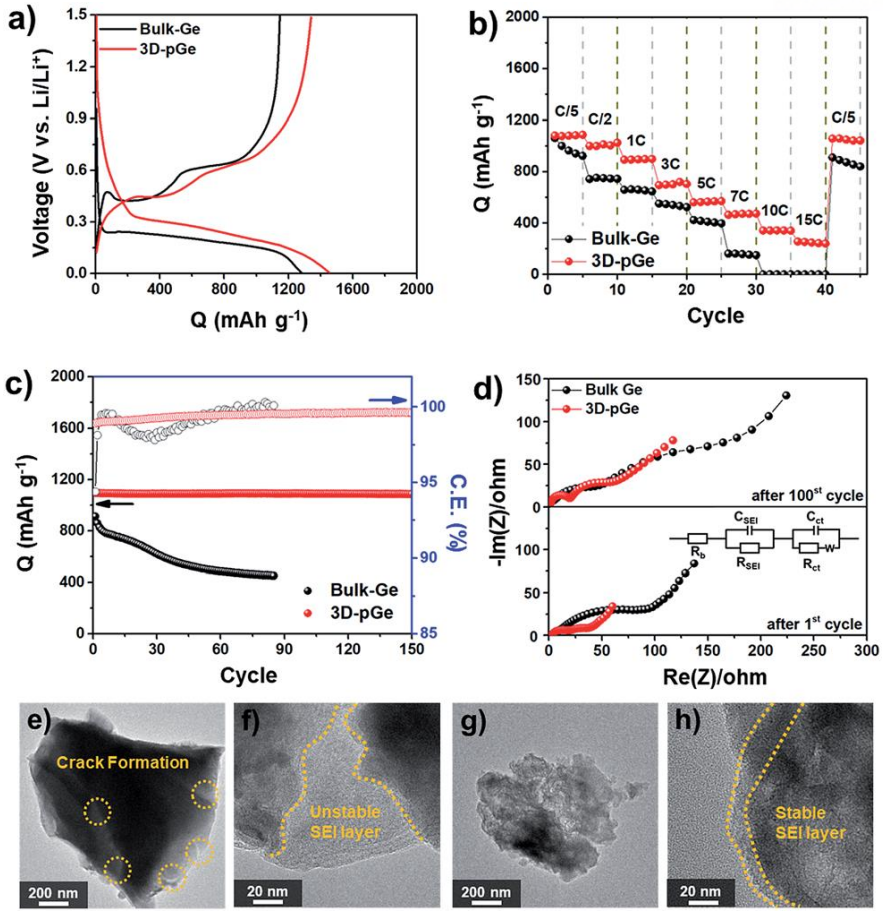

Figure 5-3. The electrochemical performance of half cells. (a) Galvanostatic charge/discharge profile at C/20 and (b) rate capability at various current rates (rate of charge = rate of discharge). (c) Cycle retention at C/5 during 150 cycles. (d) Nyquist plots of bulk Ge and 3D-pGe electrode after the 1st and 100th cycle. The inset corresponds to the equivalent circuit. TEM images of (e and f) bulk-Ge and (g and h) 3D-pGe after the 100th cycle.

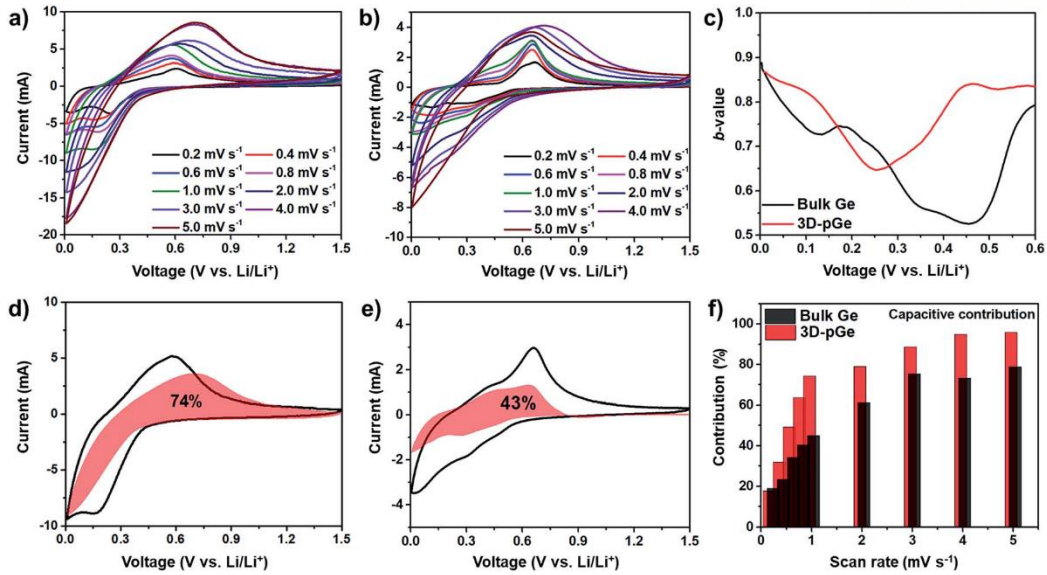

Figure 5-4. CV curves of (a) 3D-pGe and (b) bulk-Ge electrodes at various scan rates. (c) Calibrated curve of b-value vs. voltage. Contribution of capacitive current for (d) 3D-pGe and (e) bulk-Ge at 1.0 mV s^{-1}. (f) Capacitive current contribution of 3D-pGe and bulk Ge depending on scan rates.

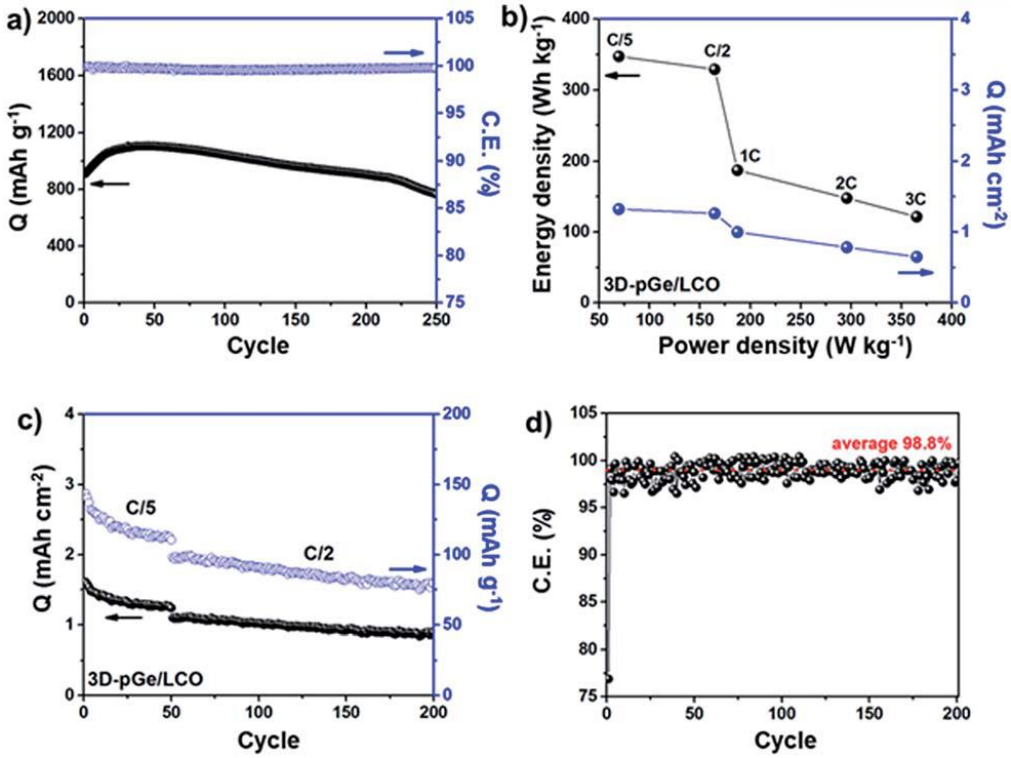

Figure 5-5. (a) Cyclic performance of 3D-pGe anode at 1C. Electrochemical properties of a 3D-pGe/LCO full-cell. (b) The plots of energy density and rate performance depending on power density. (c) Cycle retention at C/5 and C/2. (d) C.E. distribution for each cycle corresponding to (c).

5.4 Conclusion

In summary, we firstly prepared Ge-based zeolite-type compound and synthesized 3D porous Ge materials, micron-scale architecture, constructed by nanostructured Ge particles *via* a thermal deformation of artificial Ge-rich zeolite, etching with warm water, and subsequent hydrogen reduction. The 3D-pGe sample was synthesized with high-porosity in overall framework without using the harmful etchant and assistance of removable or sacrificial templates. This anode material showed the following advantages including (i) effective facilitation of electrolyte penetration, (ii) fast Li-ion/electron transfer, (iii) alleviation of the volume expansion during electrochemical test, and (iv) enhancement of pore reversibility. Therefore, the resulting 3D-pGe exhibited a high capacity with excellent CE without any supporting materials. In particular, the 3D-pGe electrode with high capacitive current contribution showed excellent rate capabilities with 895, 570, 342, and 255 mAh g^{-1} at 1, 5, 10, and 15 C, and followed by well-recovered capacity when the current rate returned to C/5 (98.6% capacity recovery). In addition, a full-cell of 3D-pGe anode paired with LCO cathode exhibited the enhanced electrochemical properties showing 348 Wh kg^{-1} (365 W kg^{-1} at maximum) and high efficiency of average 98.8% without a dramatic capacity decay over 200 cycles. The significance of this strategy opens up a simple, inexpensive, and scalable method to produce porous Ge materials from zeolite for energy storage applications.

5.5 Reference

1. Perot, G.; Guisnet, M. Advantages and disadvantages of zeolites as catalysts in organic chemistry. *J. Mol. Catal.* **1990**, *61*, 173.
2. Yaghi, O. M.; O'keeffe, M.; Ockwig, N. W.; Chae, H. K.; Eddaoudi M.; Kim, J. Reticular synthesis and the design of new materials. *Nature* **2003**, *423*, 705.
3. Han, Y.; Qi, P.; Zhou, J.; Feng, X.; Li, S.; Fu, X.; Zhao, J.; Yu, D.; Wang, B. Metal-Organic Frameworks (MOFs) as Sandwich Coating Cushion for Silicon Anode in Lithium Ion Batteries. *ACS Appl. Mater. Interfaces* **2015**, *7*, 26608.
4. Dong, X.; Mi, W.; Yu, L.; Jin, Y.; Lin, Y. S. Zeolite coated polypropylene separators with tunable surface properties for lithium-ion batteries. *Microporous Mesoporous Mater.* **2016**, *226*, 406.
5. Li, S.; Fu, X.; Zhou, J.; Han, Y.; Qi, P.; Gao, X.; Feng, X.; Wang B. An effective approach to improve the electrochemical performance of $LiNi_{0.6}Co_{0.2}Mn_{0.2}O_2$ cathode by an MOF-derived coating. *J. Mater. Chem. A* **2016**, *4*, 5823.
6. Ryu, J.; Hong, D.; Shin, M.; Park, S. Multiscale Hyperporous Silicon Flake Anodes for High Initial Coulombic Efficiency and Cycle Stability. *ACS Nano* **2016**, *10*, 10589.
7. Ryu, J.; Hong, D.; Choi, S.; Park, S. Synthesis of Ultrathin Si Nanosheets from Natural Clays for Lithium-Ion Battery Anodes. *ACS Nano* **2016**, *10*, 2843.
8. Lin, D.; Lu, Z.; Hsu, P.-C.; Lee, H. R.; Liu, N.; Zhao, J.; Wang, H.; Liu, C.; Cui, Y. A high tap density secondary silicon particle anode fabricated by scalable mechanical pressing for lithium-ion batteries. *Energy Environ. Sci.* **2015**, *8*, 2371.
9. Liu, Z.; Guan, D.; Yu, Q.; Win, L.; Zhuang, Z.; Zhu, T.; Zhao, O.; Zhou, L.; Mai, L. Monodisperse and homogeneous SiOx/C microspheres: A promising high-capacity and durable anode material for lithium-ion batteries. *Energy Storage Mater.* **2018**, *13*, 112.
10. Tang, C.; Zhu, J.; Wei, X.; He, L.; Zhao, K.; Xu, C.; Zhou, L.; Wang, B.; Sheng, J.; Mai, L. Copper silicate nanotubes anchored on reduced graphene oxide for long-life lithium-ion battery. *Energy Storage Mater.* **2017**, *7*, 152.
11. Wang, D.; Chang, Y.-L.; Wang, Q.; Cao, J.; Farmer, D. B.; Gordon, R. G.; Dai, H. Surface Chemistry and Electrical Properties of Germanium Nanowires. *J. Am. Chem. Soc.* **2004**, *126*, 11602.
12. Fuller, C. S.; Severiens, J. C. Mobility of Impurity Ions in Germanium and Silicon. *Phys. Rev.* **1954**, *96*, 21.

13. Liu, X. H.; Huang, S.; Picraux, S. T.; Li, J.; Zhu, T.; Huang, J. Y. Reversible Nanopore Formation in Ge Nanowires during Lithiation–Delithiation Cycling: An In Situ Transmission Electron Microscopy Study. *Nano Lett.* **2011**, *11*, 3991.

14. Palacin, M. R. Recent advances in rechargeable battery materials: a chemist's perspective. *Chem. Soc. Rev.* **2009**, *38*, 2565.

15. Cabana, J.; Monconduit, L.; Larcher, D.; Palacin, M. R. Beyond Intercalation-Based Li-Ion Batteries: The State of the Art and Challenges of Electrode Materials Reacting Through Conversion Reactions. *Adv. Mater.* **2010**, *22*, E170.

16. Graetz, J.; Ahn, C. C.; Yazami, R.; Fultz, B. Nanocrystalline and Thin Film Germanium Electrodes with High Lithium Capacity and High Rate Capabilities. *J. Electrochem. Soc.* **2004**, *151*, A698.

17. Seo, M.-H.; Park, M.; Lee, K. T.; Kim, K.; Kim, J.; Cho, J. High performance Ge nanowire anode sheathed with carbon for lithium rechargeable batteries. *Energy Environ. Sci.* **2011**, *4*, 425.

18. Yoon, S.; Jung, S.-H.; Jung, K.-N.; Woo, S.-G.; Cho, W.; Jo, Y.-N.; Cho, K. Y. Preparation of nanostructured Ge/GeO2 composite in carbon matrix as an anode material for lithium-ion batteries. *Electrochim. Acta* **2016**, *188*, 120.

19. Seng, K. H.; Park, M.-H.; Guo, Z. P.; Liu, H. K.; Cho, J. Self-Assembled Germanium/Carbon Nanostructures as High-Power Anode Material for the Lithium-Ion Battery. *Angew. Chem. Int. Ed.* **2012**, *51*, 5657.

20. Choi, S.; Kim, J.; Choi, N.-S.; Kim, M. G.; Park, S. Cost-Effective Scalable Synthesis of Mesoporous Germanium Particles via a Redox-Transmetalation Reaction for High-Performance Energy Storage Devices. *ACS Nano* **2015**, *9*, 2203.

21. Kennedy, T.; Mullane, E.; Geaney, H.; Osiak, M.; O'Dwyer, C.; Ryan, K. M. High-Performance Germanium Nanowire-Based Lithium-Ion Battery Anodes Extending over 1000 Cycles Through in Situ Formation of a Continuous Porous Network. *Nano Lett.* **2014**, *14*, 716.

22. Lee, H.; Kim, M. G.; Choi, C. H.; Sun, Y.-K.; Yoon, C. S.; Cho, J. Surface-Stabilized Amorphous Germanium Nanoparticles for Lithium-Storage Material. *J. Phys. Chem. B* **2005**, *109*, 20719.

23. Wang, X.-L.; Han, W.-Q.; Chen, H.; Bai, J.; Tyson, T. A.; Yu, X.-Q.; Wang, X.-J.; Yang, X.-Q. Amorphous Hierarchical Porous GeOx as High-Capacity Anodes for Li Ion Batteries with Very Long Cycling Life. *J. Am. Chem. Soc.* **2011**, *133*, 20692.

24. Li, Y.; Fu, Z.-Y.; Su, B.-L. Hierarchically Structured Porous Materials for Energy Conversion and Storage *Adv. Funct. Mater.* **2012**, *22*, 4634.

25. Arico, A. S.; Bruce, P.; Scrosati, B.; Tarascon, J.-M.; van Schalkwijk, W. Nanostructured materials for advanced energy conversion and storage devices. *Nat. Mater.* **2005**, *4*, 366.

26. Bruce, P. G.; Scrosati, B.; Tarascon, J.-M. Nanomaterials for Rechargeable Lithium Batteries. *Angew. Chem. Int. Ed.* **2008**, *47*, 2930.

27. Park, M.-H.; Kim, K.; Kim, J.; Cho, J. Flexible Dimensional Control of High-Capacity Li-Ion-Battery Anodes: From 0D Hollow to 3D Porous Germanium Nanoparticle Assemblies. *Adv. Mater.* **2010**, *22*, 415.

28. Liu, X.; Zhao, J.; Hao, J.; Su, B.-L.; Li, Y. 3D ordered macroporous germanium fabricated by electrodeposition from an ionic liquid and its lithium storage properties. *J. Mater. Chem. A* **2013**, *1*, 15076.

29. van Vugt, L. K.; van Driel, A. F.; Tjerkstra, R. W.; Bechger, L.; Vos, W. L.; Vanmaekelbergh, D.; Kelly, J. J. Macroporous germanium by electrochemical deposition. *Chem. Commun.* **2002**, *18*, 2054.

30. Miguez, H.; Chomski, E.; Garcia-Santamaria, F.; Ibisate, M.; John, S.; López, C.; Meseguer, F.; Mondia, J. P.; Ozin, G. A.; Toader, O.; van Driel, H. M. Photonic Bandgap Engineering in Germanium Inverse Opals by Chemical Vapor Deposition. *Adv. Mater,* **2001**, *13*, 1634.

31. Pan, C.-Y.; Mai, H.-D.; Yang, G.-Y. A new zeotype borogermanate β-K2B2Ge3O10: Synthesis, structure, property and conformational polymorphism. *Microporous Mesoporous Mater.* **2013**, *168*, 183.

32. Kong, F.; Jiang, H.-L.; Hu, T.; Mao, J.-G. CsB_3GeO_7 and $K_2B_2Ge_3O_{10}$: Explorations of New Second-Order Nonlinear Optical Materials in the Borogermanate Systems. *Inorg. Chem.* **2008**, *47*, 10611.

33. Ding, X.; Wang, Q.; Wang, Y. Rare-earth-free red-emitting $K_2Ge_4O_9$:Mn^{4+} phosphor excited by blue light for warm white LED. *Phys. Chem. Chem. Phys.* **2016**, *18*, 8088.

34. Sawyer, R.; Nesbitt, H. W.; Secco, R. A. High resolution X-ray Photoelectron Spectroscopy (XPS) study of K_2O–SiO_2 glasses: Evidence for three types of O and at least two types of Si. *J. Non-Cryst. Solids* **2012**, *358*, 290.

35. Bom, N. M.; Soares, G. V.; Krug, C.; Pezzi, R. P.; Baumvol, I. J. R.; Radtke, C. Evolution of the Al_2O_3/Ge(100) interface for reactively sputter-deposited films submitted to postdeposition anneals. *Appl. Surf. Sci.* **2012**, *258*, 5707.

36. Van Devener, B.; Perez, J. P. L.; Jankovich, J.; J. Anderson, J. Oxide-Free, Catalyst-Coated, Fuel-Soluble, Air-Stable Boron Nanopowder as Combined Combustion Catalyst and High Energy Density Fuel. *Energy Fuels,* **2009**, *23*, 6111.

37. Völlenkle, H.; Wittmann, A. Die kristallstruktur des kaliumtetragermanats $K_2[Ge_4O_9]$. *Monatsh. Chem.* **1971**, *102*, 1245.

38. Liu, X.; Ye, S.; Qiao, Y.; Dong, G.; Zhang, Q.; Qiu, J. Facile synthetic strategy for efficient and multi-color fluorescent BCNO nanocrystals. *Chem. Commun.* **2009**, *27*, 4073.

39. Mutreja, V.; Singh, S.; Ali, A. Potassium impregnated nanocrystalline mixed oxides of La and Mg as heterogeneous catalysts for transesterification. *Renew. Energy* **2014**, *62*, 226.

40. Ryu, J.; Hong, D.; Shin, S.; Choi, W.; Kim, A.; Park, S. Hybridizing germanium anodes with polysaccharide-derived nitrogen-doped carbon for high volumetric capacity of Li-ion batteries. *J. Mater. Chem. A* **2017**, *5*, 15828

41. Mikhaylov, A. A.; Medvedev, A. G.; A. G.; Grishanov, A. G.; Tripol'skaya, T. A.; Mel'nik, E. A.; Prikhodchenko, P. V.; Lev, O. A composite based on sodium germanate and reduced graphene oxide: Synthesis from peroxogermanate and application as anode material for lithium ion batteries. *Russ. J. Inorg. Chem.* **2017**, *62*, 1624.

42. Yoon, T.; Bok, T.; Kim, C.; Na, Y.; Park S.; Kim, K.S. Mesoporous Silicon Hollow Nanocubes Derived from Metal–Organic Framework Template for Advanced Lithium-Ion Battery Anode. *ACS Nano* **2017**, *11*, 4808.

43. Yang, Y.; Zhao, X.; Wang, H.-E.; Li, M.; Hao, C.; Ji, M.; Ren, S.; Cao, G. Phosphorized SnO_2/graphene heterostructures for highly reversible lithium-ion storage with enhanced pseudocapacitance. *J. Mater. Chem. A* **2018**, *6*, 3479.

44. Jiang, Y.; Li, Y.; Zhou, P.; Lan, Z.; Lu, Y.; Wu, C.; Yan, M. Ultrafast, Highly Reversible, and Cycle-Stable Lithium Storage Boosted by Pseudocapacitance in Sn-Based Alloying Anodes. *Adv. Mater.* **2017**, *29*, 1606499.

45. Lindstrom, H.; Sodergren, S.; Solbrand, A.; Rensmo, H.; Hjelm, J.; Hagfeldt, A.; Lindquist, S.-E. Li^+ Ion Insertion in TiO_2 (Anatase). 2. Voltammetry on Nanoporous Films. *J. Phys. Chem. B* **1997**, *101*, 7717.

46. Wang, J.; Polleux, J.; Lim, J.; Dunn, B. Pseudocapacitive Contributions to Electrochemical Energy Storage in TiO_2 (Anatase) Nanoparticles. *J. Phys. Chem. C* **2007**, *111*, 14925.

47. Chao, D.; Zhu, C.; Yang, P.; Xia, X.; Liu, J.; Wang, J.; Fan, X.; Savilov, S. V.; Lin, J.; Fan, H. J.; Shen, Z. X. Array of nanosheets render ultrafast and high-capacity Na-ion storage by tunable pseudocapacitance. *Nat Commun.* **2016**, *7*, 12122.

48. Yang, X.; Zhang, R.-Y.; Zhao, J.; J. Wei, J.; Wang, D.-X.; Bie, X.-F.; Gao, Y.; Wang, J.; Du, F. Chen, G. Amorphous Tin-Based Composite Oxide: A High-Rate and Ultralong-Life Sodium-Ion-Storage Material. *Adv. Energy Mater.* **2018**, *8*, 1701827.

6. Summary and outlook

Lithium-ion batteries serving high energy and power density are recently under tremendous development for large-scale energy storage system. High energy anode materials particularly like silicon (Si) and germanium (Ge) have been become the object of the breakthrough to overcome issues of present lithium-ion batteries. However, the simple high energy system cannot deal all of demands in practical battery for high power and long lifespan as well as high energy. With the dimensional and structural control, the system has been materialized to meet the specific purpose of desired electrochemical results. Thus, the correlation of various dimension and structural modification with the specific electrochemical properties are summarized in here to generally suggest the further research guideline concerning dimensional design of anode materials.

In recent trends in nanoscale Si, the electrodes are favorable to less volume expansion on repeating cycles and still receive the help from additional conductive matters due to unchanged intrinsic properties of electronic/ionic conductivity. However, the initial coulombic efficiency and reversible capacity in essential aspect of practical battery performance decrease because higher volume-to-surface ratio cause spacious SEI layer formation on nanosized structures. Nanostructured Si was summarized in Figure 6-1 concerning initial coulombic efficiency and reversible capacity in the function of dimensions.[1-15] The capacities show wide range because various supporting matters and amounts are combined with nanosized silicon to enhance prolong electrochemical properties. The electrodes in general exhibit poor initial coulombic efficiency as mentioned structural factors. Among nanosized Si dimensions, 0D Si can more manageable dimensions and capacities owing to versatile methods for the collaboration with foreign matters to serve the purpose. Meanwhile, 2D Si shows relatively higher coulombic efficiency corresponding to searched results compared to other dimensions. It might be attributed to lower surface area of two-dimensional nanostructure.[16]

Microsized Si anodes are mostly designed as 0D and 3D through secondary particles integrity or naturally obtained microparticles (Figure 6-2).[17-20] Further, they possess high volumetric capacity/tap density/cost effectiveness compared to nanosized Si anodes. Instead, those microsized structures require buffer/conductive pathway due to high absolute volume change value to keep the advantage, high initial coulombic efficiency and high areal capacity related to much lower surface area. Nevertheless, real microsized Si composite anodes are still under research level because these barely produce high power density due to long diffusion length into core Si atoms.

As the other candidates, Ge materials feature 400 and 10^4 times higher Li diffusivity and

electronic conductivity rather than Si.[21] Further, they shows similar working potential (0.5 V, compared to Si; 0.4 V vs. Li/Li^+) and theoretical volumetric capacity (8645, compared to Si; 9781Ah L^{-1} in form of $Li_{22}M$, M = Si, Ge) with Si anodes.[22] However, Ge anodes unfortunately suffer from lower intrinsic issue for electronic/ionic conductivity and large volume expansion. So, Ge have been generally tried to develop unsettle issues in lithium-ion batteries through the dimensional designs, same as Si anodes. In this regard, Ge anodes are also summarized in Figure 6-3[23-34] and 6-4[35-38] related to each nanoscale and microscale. They display similar factors to address each undesired electrochemical result as mentioned for Si case.

Consequently, for Si/Ge anode approaches in intensive opinion, it is essential to study secondary microparticles consisting nano-level design of Si/Ge-based composites for achieving high power density as well as high energy and initial coulombic efficiency.

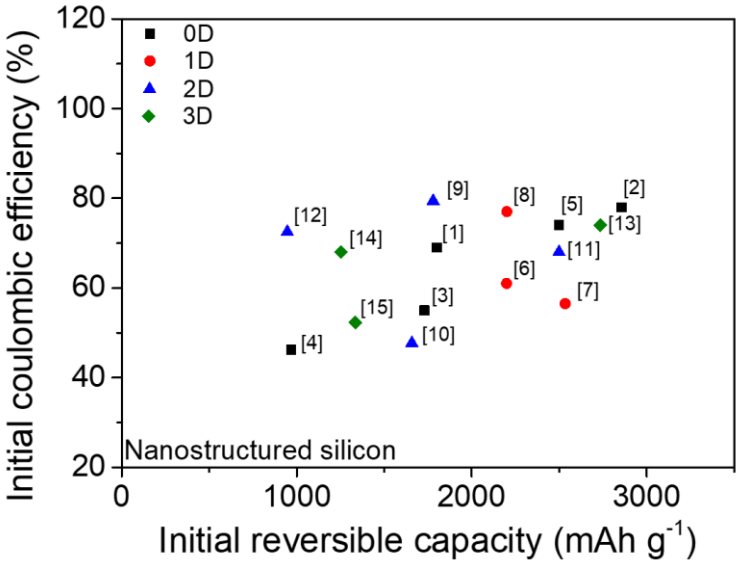

Figure 6-1. The ragone plot of nanostructured silicon concerning dimensions.[1-15]

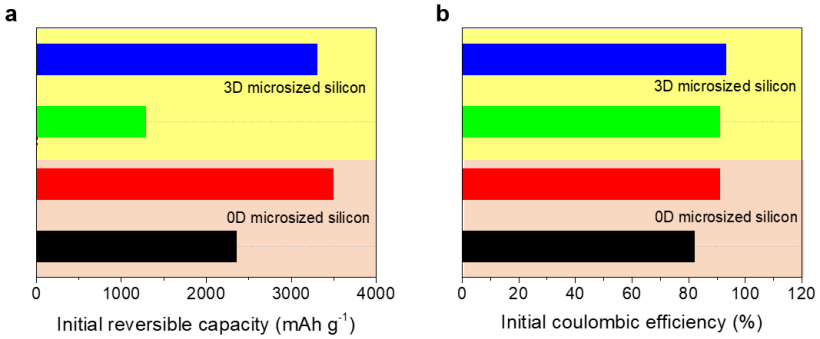

Figure 6-2. (a) Initial reversible capacity and (b) coulombic efficiency of various microsized silicon anodes.[17-20]

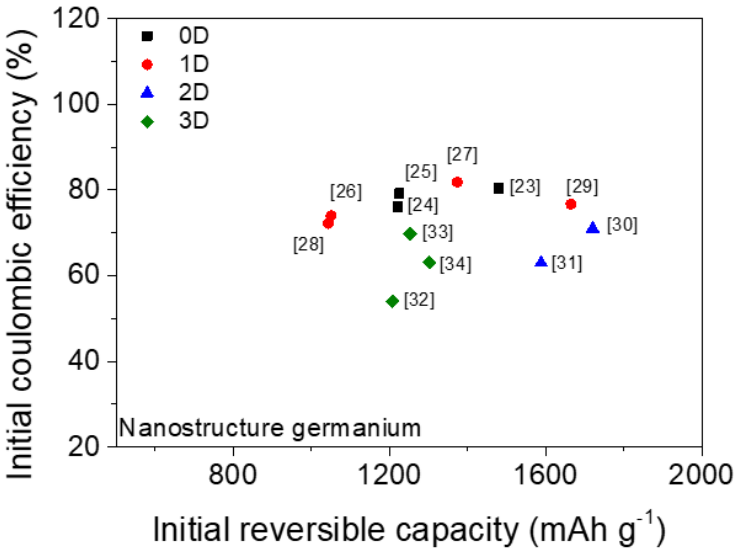

Figure 6-3. The ragone plot of nanostructured germanium concerning dimensions.[23-34]

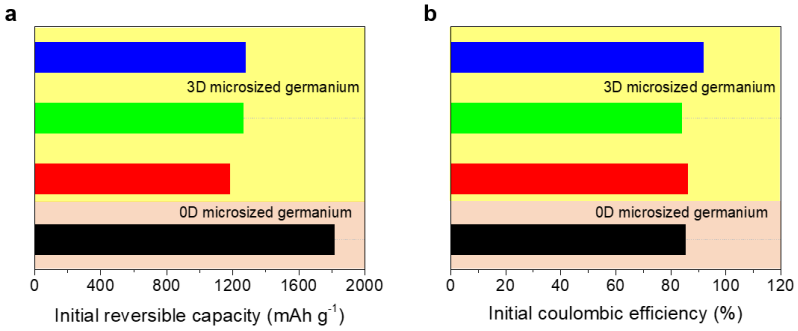

Figure 6-4. (a) Initial reversible capacity and (b) coulombic efficiency of various microsized germanium anodes.

Reference

1. Chen, S.; Shen, L.; van Aken, P. A.; Maier, J.; Yu, Y. Dual-Functionalized Double Carbon Shells Coated Silicon Nanoparticles for High Performance Lithium-Ion Batteries, *Adv. Mater.* **2017**, *29*, 1605650.

2. Higgins. T. M.; Park, S.-H.; King, P. J.; Zhang, C.; McEvoy, M.; Berner, N. C.; Daly, D.; Shmeliov, A.; Khan, Y.; Duesberg, G.; Nicolosi, V.; Coleman, J. N. A Commercial Conducting Polymer as Both Binder and Conductive Additive for Silicon Nanoparticle-Based Lithium-Ion Battery Negative Electrodes. *ACS Nano* **2016**, *10*, 3702-3713.

3. Guo, S.; Hu, X.; Hou, Y.; Wen, Z. Tunable Synthesis of Yolk-Shell Porous Silicon@Carbon for Optimizing Si/C-Based Anode of Lithium-Ion Batteries. *ACS Appl. Mater. Interfaces* **2017**, *9*, 42084-42092.

4. Park, E.; Kim, J.; Chung, D. J.; Park, M.-S.; Kim, H.; Kim, J. H. Si/SiO_x-Conductive Polymer Core-Shell Nanospheres with an Improved Conducting Path Preservation for Lithium-Ion Battery. *ChemSusChem* **2016**, *9*, 2754-2758.

5. Liu, Y.; Tai, Z.; Zhou, T.; Sencadas, V.; Zhang, J.; Zhang, L.; Konstantinov, K.; Guo, Z.; Liu, H. K. An All-Integrated Anode via Interlinked Chemical Bonding between Double-Shelled-Yolk-Structured Silicon and Binder for Lithium-Ion Batteries. *Adv. Mater.* **2017**, *29*, 1703028.

6. Kim, G.-T.; Kennedy, T.; Brandon, M.; Geaney, H.; Ryan, K. M.; Passerini, S.; Appetecchi, G. B. Behavior of Germanium and Silicon Nanowire Anodes with Ionic Liquid Electrolytes. *ACS Nano* **2017**, *11*, 5933-5943.

7. Chen, X.; Bi, Q.; Sajjad, M.; Wang, X.; Ren, Y.; Zhou, X.; Xu, W.; Liu, Z. One-Dimensional Porous Silicon Nanowires with Large Surface Area for Fast Charge-Discharge Lithium-Ion Batteries. *Nanomaterials* **2018**, *8*, 285.

8. Son, Y.; Sim, S.; Ma, H.; Choi, M.; Son, Y.; P, N.; Cho, J.; Park, M. Exploring Critical Factors Affecting Strain Distribution in 1D Silicon-Based Nanostructures for Lithium-Ion Battery Anodes. *Adv. Mater.* **2018**, *30*, 1705430.

9. Ryu, J.; Hong, D.; Choi, S.; Park, S. Synthesis of Ultrathin Si Nanosheets from Natural Clays for Lithium-Ion Battery Anodes. *ACS Nano* **2016**, *10*, 2843-2851.

10. Chen, S.; Chen, Z.; Xu, X.; Cao, C.; Xia, M.; Luo, Y. Scalable 2D Mesoporous Silicon Nanosheets for High-Performance Lithium-Ion Battery Anode. *Small* **2018**, *14*, 1703361.

11. Wang, P. P.; Zhang, Y. X.; Fan, X. Y.; Zhong, J. X.; Huang, K. Synthesis of Si nanosheets by using Sodium Chloride as template for high-performance lithium-ion battery anode material. *J. Power Source* **2018**, *379*, 20-25.

12. Fu, R.; Zhang, K.; Zaccaria, R. P.; Huang, H.; Xia, Y.; Liu, Z. Two-dimensional silicon suboxides nanostructures with Si nanodomains confined in amorphous SiO_2 derived from siloxene as high performance anode for Li-ion batteries. *Nano Energy* **2017**, *39*, 546-553.

13. Chang, J.; Huang, X; Zhou, G.; Cui, S.; Mao, S.; Chen, J. Three-dimensional carbon-coated Si/rGO nanostructures anchored by nickel foam with carbon nanotubes for Li-ion battery applications. *Nano Energy* **2015**, *15*, 679-687.

14. Jiang, Y.; Chen, S.; Mu, D.; Wu, B.; Liu, Q.; Zhao, Z.; Wi, F. A three-dimensional network structure Si/C anode for Li-ion batteries. *J. Mater. Sci.* **2017**, *52*, 10950-10958.

15. Chang, P.; Liu, X.; Zhao, Q.; Huang, Y.; Huang, Y.; Hu, X. Constructing Three-Dimensional Honeycombed Graphene/Silicon Skeletons for High-Performance Li-Ion Batteries. *ACS Appl. Mater. Interfaces* **2017**, *9*, 31879-31886.

16. Ryu, J.; Chen, T.; Bok, T.; Song, G.; Ma, J.; Hwang, C.; Luo, L.; Song, H.K.; Cho, J.; Wang, C.; Zhang, S.; Park, S. Mechanical mismatch-driven rippling in carbon-coated silicon sheets for stress-resilient battery anodes. *Nat. Commun.* **2018**, *9*, 2924.

17. Liu, N.; Lu, Z.; Zhao, J.; McDowell, M. T.; Lee, H.-W.; Zhao, W.; Cui, Y. A pomegranate-inspired nanoscale design for large-volume-change lithium battery anodes. *Nat. Nanotech.* **2014**, *9*, 187-192.

18. Song, G.; Ryu, J.; Kim, J. C.; Lee, J. H.; Kim, S.; Wang, C.; Kwak, S. K.; Park, S. Revealing salt-expedited reduction mechanism for hollow silicon microsphere formation in bi-functional halide melts. *Commun. Chem.* **2018**, *1*, 42.

19. Chae, S.; Ko, M.; Park, S.; Kim, N.; Ma, J.; Cho, J. Micron-sized Fe-Cu-Si ternary composite anodes for high energy Li-ion batteries. *Energy Environ. Sci.* **2016**, *9*, 1251.

20. Li, Y.; Wan, K.; Lee, H.-W.; Lu, Z.; Liu, N.; Cui, Y. Growth of conformal graphene cages on micrometre-sized silicon particles as stable battery anodes. *Nat. Energy* **2016**, *1*, 15029.

21. Yoon, T.; Song, G.; Harzandi, A. M.; Ha, M.; Chou, S.; Shadman, S.; Ryu, J.; Bok, T.; Park, S.; Kim, K. S. Intramolecular deformation of zeotypeborogermanate toward a three-dimensional porous germanium anode for high-rate lithium storage. *J. Mater. Chem. A* **2018**, *6*, 15961.

22. Liu, D.; Liu, Z.; Li, X.; Xie, W.; Wang, Q.; Liu, Q.; Fu, Y.; He, D. Group IVA Element (Si, Ge, Sn)-Based Alloying/Dealloying Anodes as Negative Electrodes for Full-Cell Lithium-Ion Batteries. *Small* **2017**, *13*, 1702000.

23. Liu, X.; Lin, N.; Cai, W.; Zhao, Y.; Zhou, J.; Liang, J.; Zhu, Y.; Qian, Y. Mesoporous germanium nanoparticles synthesized in molten zinc chloride at low temperature as a high-performance anode for lithium-ion batteries. *Dalton Trans.* **2018**, *47*, 7402.

24. Mo, R.; Rooney, D.; Sun, K. Yolk-Shell Germanium@Polypyrrole Architecture with Precision Expansion Void Control for Lithium Ion Batteries. *iScience* **2018**, *9*, 521-531.

25. Wang, L.; Bao, K.; Lou, Z.; Liang, G.; Zhou, Q. Chemical synthesis of germanium nanoparticles with uniform size as anode materials for lithium ion batteries. *Dalton Trans*. **2016**, *45*, 2814.

26. Wang, X.; Fan, L.; Gong, D.; Zhu, J.; Zhang, Q.; Lu, B. Core-Shell Ge@Graphene@TiO_2 Nanofibers as a High-Capacity and Cycle-Stable Anode for Lithium and Sodium Ion Battery. *Adv. Funct. Mater.* **2016**, *26*, 1104-1111.

27. Kim, C.; Song, G.; Luo, L.; Cheong, J. Y.; Cho. S.-H.; Kwon, D.; Choi, S.; Jung, J.-W.; Wang, C.-M.; Kim, I.-D.; Park, S. Stress-Tolerant Nanoporous Germanium Nanofibers for Long Cycle Life Lithium Storage with High Structural Stability. *ACS Nano* **2018**, *12*, 8169-8176.

28. Song, G.; Cheong, J. Y.; Kim, C.; Luo, L.; Hwang, C.; Choi, S.; Ryu, J.; Kim, S.; Song, W.-K.; Song, H.-K.; Wang, C.; Kim, I.-D.; Park, S. Atomic-scale combination of germanium-zinc nanofibers for structural and electrochemical evolution. *Nat. Commun.* **2019**, *10*, 2364.

29. Hao, J.; Yang, Y.; Zhao, J.; Liu, X.; Endres, F.; Chi, C.; Wang, B.; Liu, X.; Li, Y. Ionic liquid electrodeposition of strain-released Germanium nanowires as stable anodes for lithium ion batteries. *Nanoscale* **2017**, *9*, 8481.

30. Bensalah, N.; Kamand, F. Z.; Mustafa, N.; Matalqeh, M. Silicon-Germanium bilayer sputtered onto a carbon nanotube sheet as anode material for lithium-ion batteries. *J. Alloys Compd.* **2019**, *811*, 152088.

31. Wang, B.; Du, W.; Yang, Y.; Zhang, Y.; Zhang, Q.; Rui, X.; Geng, H.; Li, C. C. Two-Dimensional Germanium Sulfide Nanosheets as an Ultra-Stable and High Capacity Anode for Lithium Ion Batteries. *Chem. Eur. J.* **2019**, *25*, 1-8.

32. Ma, Q.; Wang, W.; Zeng, P.; Fang, Z. Amorphous Ge/C Composite Sponges: Synthesis and Application in a High-Rate Anode for Lithium Ion Batteries. *Langmuir* **2017**, *33*, 2141-2147.

33. Kwon, D.; Ryu, J.; Shin, M.; Song, G.; Hong, D.; Kim, K. S.; Park, S. Synthesis of dual porous structured germanium anodes with exceptional lithium-ion storage performance. *J. Power Source* **2018**, *374*, 217-224.

34. Ngo, D. T.; Kalubarme, R. S.; Le, H. T. T.; Fisher, J. G.; Park, C.-N.; Kim, I.-D.; Park, C.-J. Carbon-Interconnected Ge Nanocrystals as an Anode with Ultra-Long-Term Cyclability for Lithium Ion Batteries *Adv. Funct. Mater.* **2014**, *24*, 5291-5298.

35. Tseng, K.-W.; Huang, S.-B.; Chang, W.-C.; Tuan, H.-Y. Synthesis of Mesoporous Germanium Phosphide Microspheres for High-Performance Lithium-Ion and Sodium-Ion Battery Anodes. *Chem. Mater.* **2018**, *30*, 4440-4447.

36. Klavetter, J. C.; de Souza, J. P.; Heller, A.; Mullins, C. B. High tap density microparticles of selenium-doped germanium as a high efficiency, stable cycling lithium-ion battery anode material. *J. Mater. Chem. A* **2015**, *3*, 5829.

37. Liang, J.; Li, X.; Hou, Z.; Zhang, T.; Zhu, Y.; Yan, X.; Qian, Y. Honeycomb-like Macro-Germanium as High-Capacity Anodes for Lithium-Ion Batteries with Good Cycling and Rate Performance. *Chem. Mater.* **2015**, *27*, 4156−4164.

38. Zhang, C.; Lin, Z.; Yang, Z.; Xiao, D.; Hu, P. Xu, H.; Duan, Y.; Pang, S.; Gu, L.; Cui, G. Hierarchically Designed Germanium Microcubes with High Initial Coulombic Efficiency toward Highly Reversible Lithium Storage. *Chem. Mater.* **2015**, *27*, 2189−2194.